

Supporting Information

Large Variations in the Single-Molecule Conductance of Cyclic and Bicyclic Silanes

Haixing Li,¹ Marc H. Garner,² Zhichun Shangguan,³ Yan Chen,³ Qianwen Zheng,³ Timothy A. Su,⁴ Madhav Neupane,⁴ Taifeng Liu,³ Michael L. Steigerwald,^{*4} Fay Ng,⁴ Colin Nuckolls,^{*4} Shengxiang Xiao,^{*3} Gemma C. Solomon,^{*2} Latha Venkataraman^{*1,4}

¹Department of Applied Physics and Applied Mathematics, Columbia University, New York, New York 10027, United States

²Nano-Science Center and Department of Chemistry, University of Copenhagen, Universitetsparken 5, 2100 Copenhagen Ø, Denmark

³The Education Ministry Key Lab of Resource Chemistry, Shanghai Key Laboratory of Rare Earth Functional Materials, Optoelectronic Nano Materials and Devices Institute, Department of Chemistry, Shanghai Normal University, Shanghai 200234, China

⁴Department of Chemistry, Columbia University, New York, New York 10027, United States

Haixing Li, Marc H. Garner and Zhichun Shangguan contributed equally to this work

Table of Contents

I.	STM-Break Junction experiment details	2
II.	Additional Figures.....	2
III.	Computational Details	5
	General details	5
	Transmission plots	7
	Comparison of methods.....	10
	Conformations and transmission	12
	221 and Linear Silanes.....	12
	4-ring	14
	5-ring	17
	222	19
IV.	Synthetic Procedures and Characterization of Compounds	22
V.	NMR spectra.....	27
VI.	References	52

I. STM-Break Junction experiment details

We measured the conductance of single molecules junctions formed with gold electrodes using a custom-built modified Scanning Tunneling Microscope (STM). We used a 0.25 mm diameter gold wire (99.998%, Alfa Aesar) as the STM tip and a gold-coated (99.999%, Alfa Aesar) mica surface as the substrate. The STM was controlled using a custom software (IgorPro, Wavemetrics, Inc.) and operated in ambient conditions at room temperature. The gold substrate was cleaned using UV/Ozone for 15 minutes prior to use. For each measurement, 1000 traces were first collected prior to adding molecular solutions to ensure that the gold was clean. Solutions of the target molecules at 0.1 - 1 mM concentration in 1,2,4-trichlorobenzene (Alfa Aesar, 99% purity) were added to the substrate for molecular conductance measurements. The applied bias was 225 - 900 mV, and the substrate was moved at a speed of 19 nm/s for all measurements. The current and voltage data were acquired at 40 kHz.

For each molecule, we collected over 10,000 - 30,000 traces to create 1D and 2D conductance histograms without data selection. 2D conductance-displacement histograms are created from conductance traces for all molecules by first aligning all traces at the point where the Au-Au bond breaks, and then binning the data using linear bins along the displacement axis and logarithm bins along the conductance axis. We determine the single-molecule junction elongation length as the distance at which the distribution drops to 20% of its peak value for each molecule measured (Figure 3).

II. Additional Figures

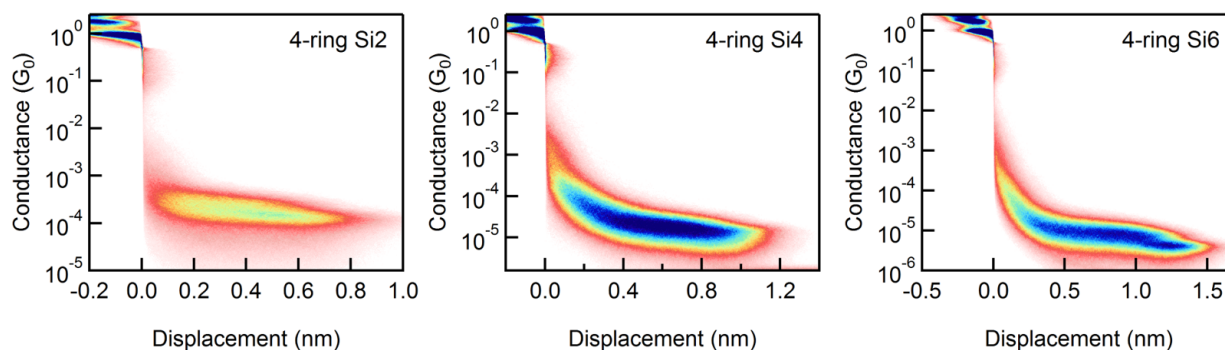


Figure S1. 2D conductance histograms for 4-ring series.

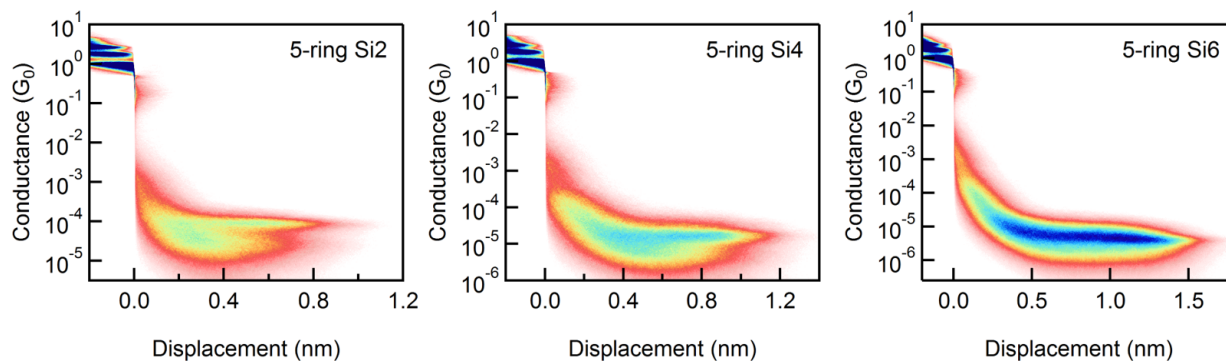


Figure S2. 2D conductance histograms for **5-ring** series.

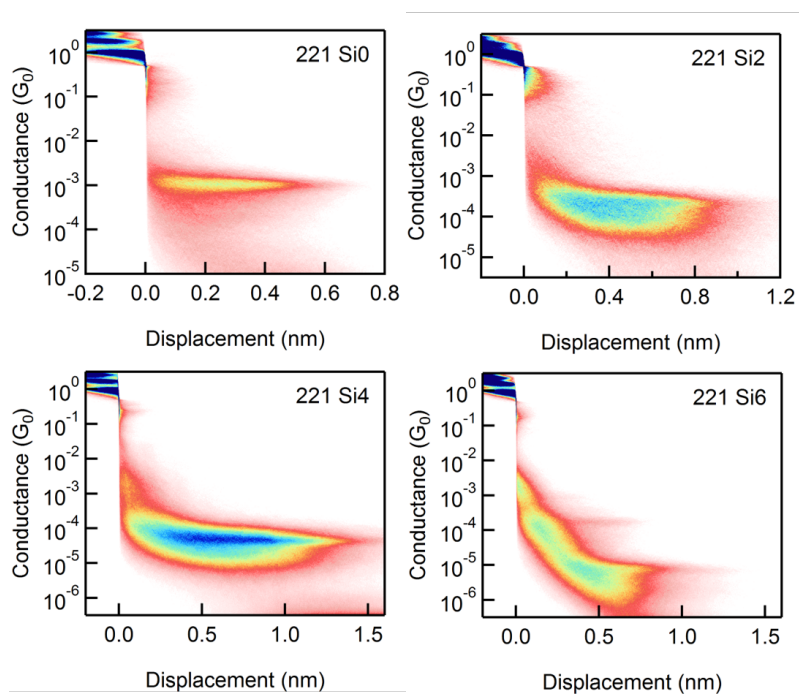


Figure S3. 2D conductance histograms for **221** series.

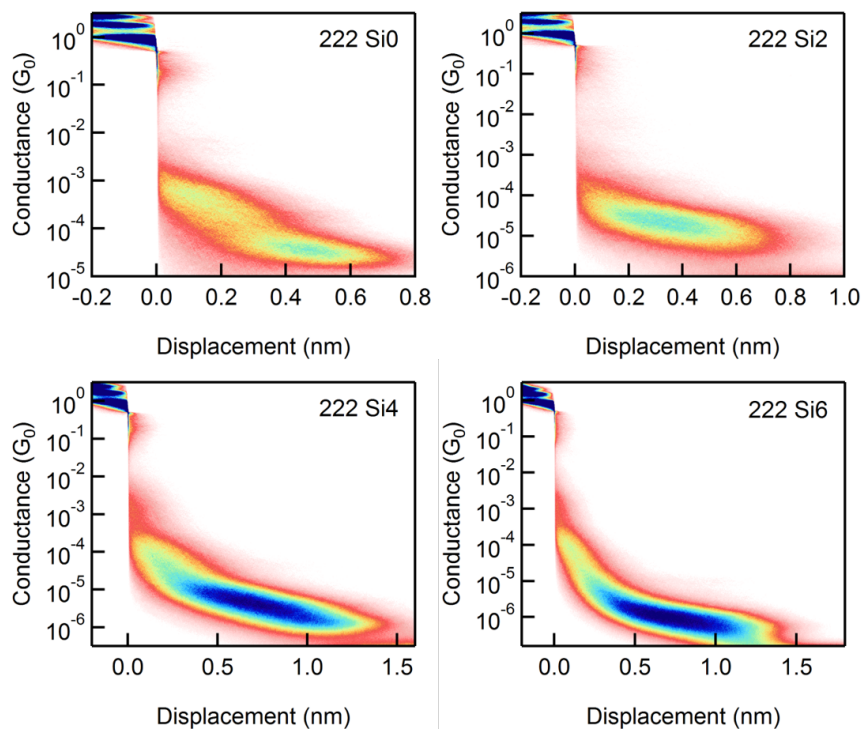


Figure S4. 2D conductance histograms for **222** series.

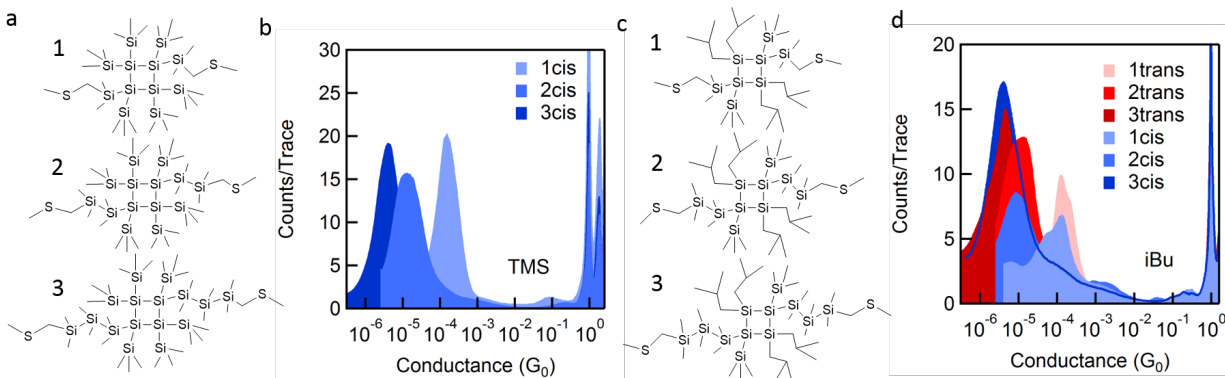


Figure S5. (a) Chemical structures and (b) 1D conductance histograms of TMS substituted **4-ring** series. (c) Chemical structures and (d) 1D conductance histograms of isobutyl substituted **4-ring** series. The counts/trace intensity of the data of *trans*-iBu is multiplied by a factor of 0.3.

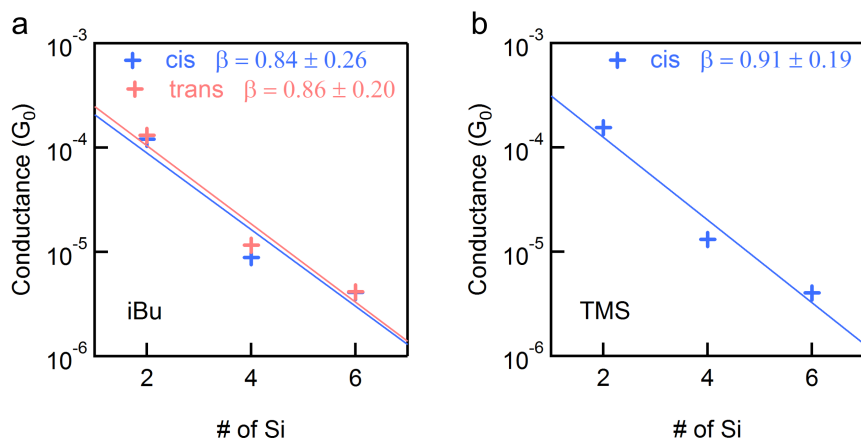


Figure S6. (a) Measured single-molecule junction conductance plotted against extending silicon chain length for cis TMS substituted **4-ring**. (b) Measured single-molecule junction conductance plotted against extending silicon chain length for cis (blue) and trans (pink) isobutyl substituted **4-ring**.

III. Computational Details

General details

In this study we aim to understand the structural and transmission trends for the experimentally studied series of molecules. In this first part, we shall describe the design of the study and the approximations that have been employed. In the following parts a comparative study of transmissions calculated with different methods is presented. Finally, the results for all series of molecules and a discussion of their conformations are presented. All structures of the isolated molecules and the junctions are available upon request.

Prior to building single-molecule junctions, we performed a conformational screening of the molecules. A complete conformational analysis is not feasible due to the vast conformational freedom of the molecules. Moreover, in the experiment the linearly extended molecules may be more likely to be in a “long” conformation, close to their all-*transoid* conformations, as the molecule is being pulled. Therefore, we focus the conformational screening on the variable cyclic or bicyclic core of each system, and extend the conformation systematically with all-*transoid* linear silane arms. All molecules are optimized in vacuum before we make the junctions.

As described in the manuscript, all vacuum optimizations are performed using density functional theory with the PBE exchange-correlation functional as implemented in the GPAW software. All atoms are optimized to a force threshold of at least $0.01 \text{ eV}/\text{\AA}$. A double- ζ plus polarization basis set is used for all atoms. Integrals are evaluated on a 3D grid with a spacing of 0.15 \AA between each point.

Single-molecule junctions are built using the following procedure:

1. The optimized molecule is loaded into the Atomic Simulation Environment software. The molecule must be in a conformation where the terminal Si-CH₂-S-CH₃ dihedrals are in *ortho*-configuration ($\sim 90^\circ$).
2. Single gold atoms are placed in the positions where we expect the tips of the electrodes to be. On the basis of test-calculations, we use the following starting-parameters (these are only used as a starting point for the relaxation). These bond and dihedral angles are illustrated in Figure S7a.
 - S-Au bond-length: 2.45 Å (2.525 Å with dzp Au)
 - C-S-Au bond angle: 110°
 - Si-CH₂-S-Au dihedral: $\pm 170^\circ$ (Either the plus or minus dihedral is used systematically throughout each molecular series.)
3. The molecule with single tip gold atom on each side is placed on 5x5x4 fcc111 gold slab with a three-atom plateau on it. The bottom tip gold atom together with the three-atom plateau thereby form a four-atom pyramid (a tetrahedron in exact terms), as shown in Figure S7b.
4. The tip gold atom axis is aligned with the junction z-axis (the direction of the current), and a three-atom plateau is placed on the other side as well. With periodic boundary conditions used in all directions, the molecule is now placed between two four-atom pyramids on Au-surfaces as can be seen in Figure S7b.

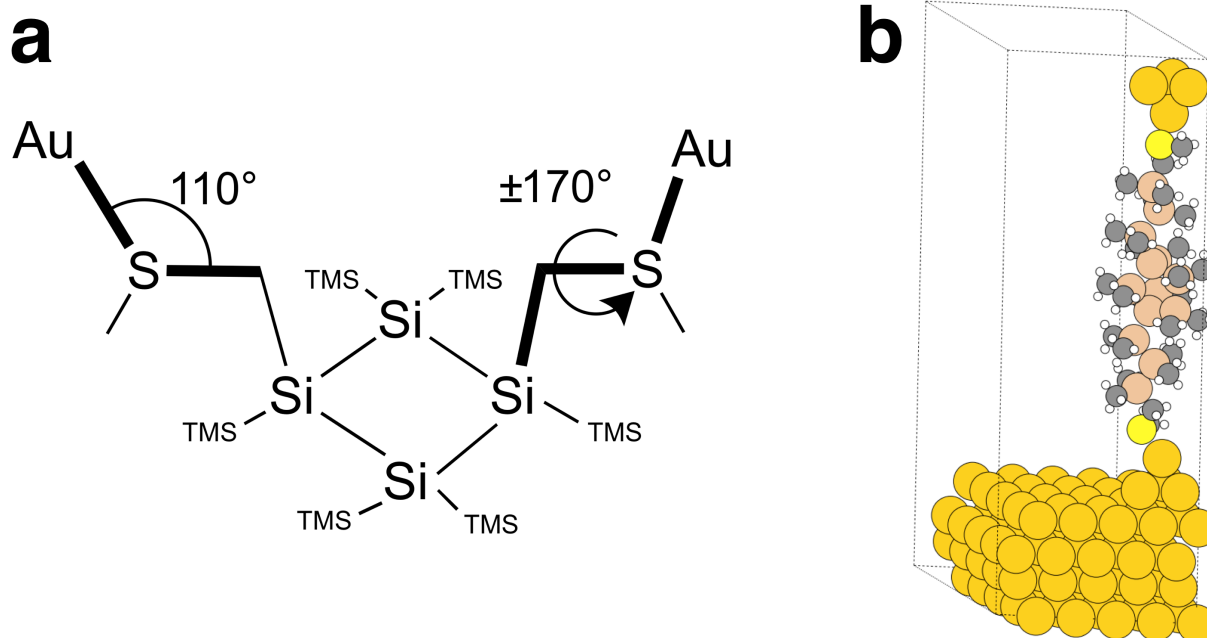


Figure S7. (a) Schematic of C-S-Au bond angle and Si-C-S-Au dihedral. **4-Ring-Sio** is used as example structure. (b) Unit-cell of a non-relaxed molecular junction. **221-Si6** is used as example structure.

The junction is relaxed to a force threshold of 0.05 eV/Å for all atoms, with the gold atoms kept fixed. Two k-points are sampled in the irreducible part of the Brillouin zone. After the relaxation, a second gold slab is placed to complete the junction as periodic boundary conditions are not used in the transport direction when the transmission is calculated.

The Landauer transmission is calculated using the non-equilibrium Green's functions approach. For the transmissions presented in the manuscript, we use Atomistix Tool Kit (ATK) and Virtual NanoLab software packages.¹⁻³ Here, the optimized junction structures (the two Au-pyramids and the molecule) are placed between semi-infinite 6×6 Au fcc(111) surfaces. Double- ζ plus polarization quality basis set is used for the atoms of the molecule, and Double- ζ basis set is used for the Au atoms. We sample one k-point in the irreducible part of the Brillouin zone for the x- and y-directions, and 200 k-points for the z-direction, i.e., the transport direction of the junction. We resolve the interatomic transmission pathways at the Fermi energy as described in detail elsewhere.⁴ Contributions to the transmission between atoms are plotted as arrows on top of the optimized junction structures. At any surface across the junction, the sum of arrows reproduces the full transmission. The cross-sectional area of the arrows scales proportionally with the magnitude of the interatomic transmission. A minimum threshold of 10% of the total transmission is used for the pathways.

To allow comparison we also calculate the transmission using GPAW. Here we use the already described junction with $5 \times 5 \times 4$ Au electrodes. Eight k-points are sampled in the irreducible part of the Brillouin zone. Double- ζ plus polarization quality basis set is used for the atoms of the molecule, and Double- ζ or Double- ζ plus polarization quality basis set is used for the Au atoms as the transmission is calculated.

Transmission plots

Here follows the remaining transmission data used in the manuscript. All transmission herein is calculated with ATK using double- ζ plus polarization basis set for the atoms of the molecule, and double- ζ basis set for the Au atoms. The transmissions of the 222 and 221 series are shown in Figure 5 in the manuscript. The transmission data of linear silanes (Fig. S8), 4-ring (Fig. S9), and 5-ring (Fig. S10) are shown here.

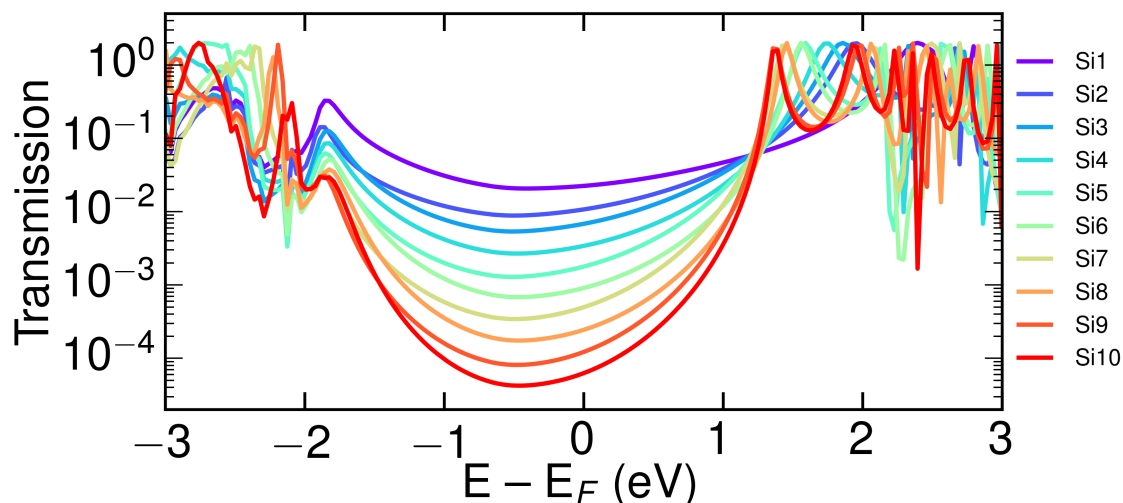


Figure S8. Transmissions of the linear silane series plotted semi-logarithmically against energy.

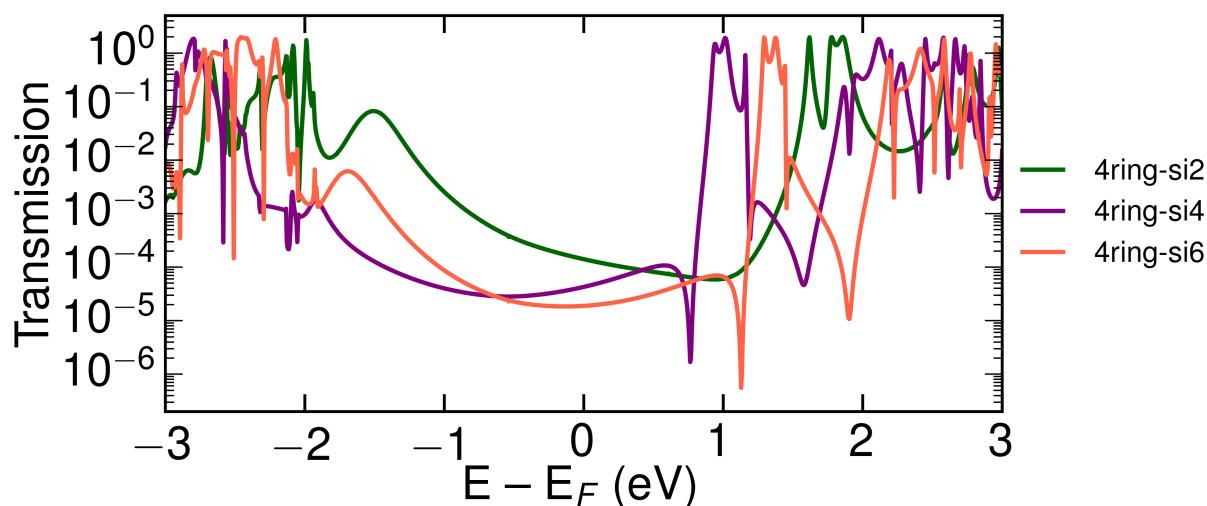


Figure S9. Transmissions of the **4-ring** series plotted semi-logarithmically against energy.

It is well-worth noting that there is an anti-resonance close to LUMO resonances for both **4-ring** and **5-ring**. While these are signatures of quantum interference, these anti-resonances do not seem to have any notable effect on the transmission at the Fermi energy.

As concluded in previous work for the non-extended **5-ring** system, there are significant through-space components to the transmission, i.e. components between non-bonded atoms, as seen in Figure S10.

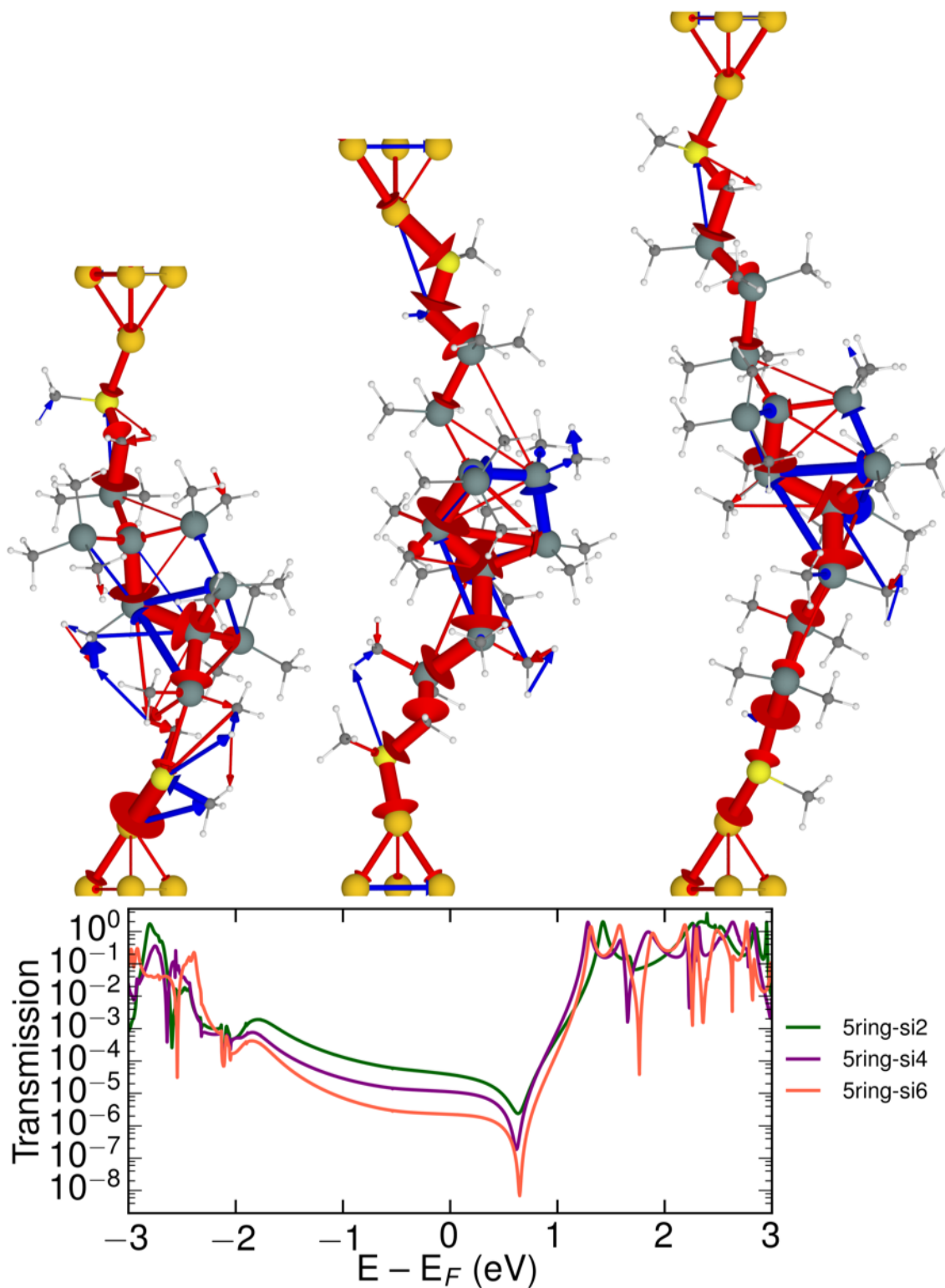


Figure S10. Local transmission and transmissions of the **5-ring** series plotted semi-logarithmically against energy.

Comparison of methods

As we have briefly discussed in the manuscript, the transmission, particularly at the Fermi energy, is very sensitive to the energy level alignment when there are anti-resonances. It is a well-known problem that the energy level alignment is far from exact with DFT, and may be sensitive to the choice of method, such as functional and basis. Here we compare three methods, all using DFT with the PBE functional. As described in the manuscript we use ATK with double- ζ plus polarization basis set for the atoms of the molecule, and double- ζ basis set for the Au atoms. We compare this to transmission calculations in GPAW, where we use double- ζ plus polarization basis set for the atoms of the molecule, and double- ζ basis set for the Au atoms just like in the ATK calculation, and another calculation where we use double- ζ plus polarization basis set for all atoms.

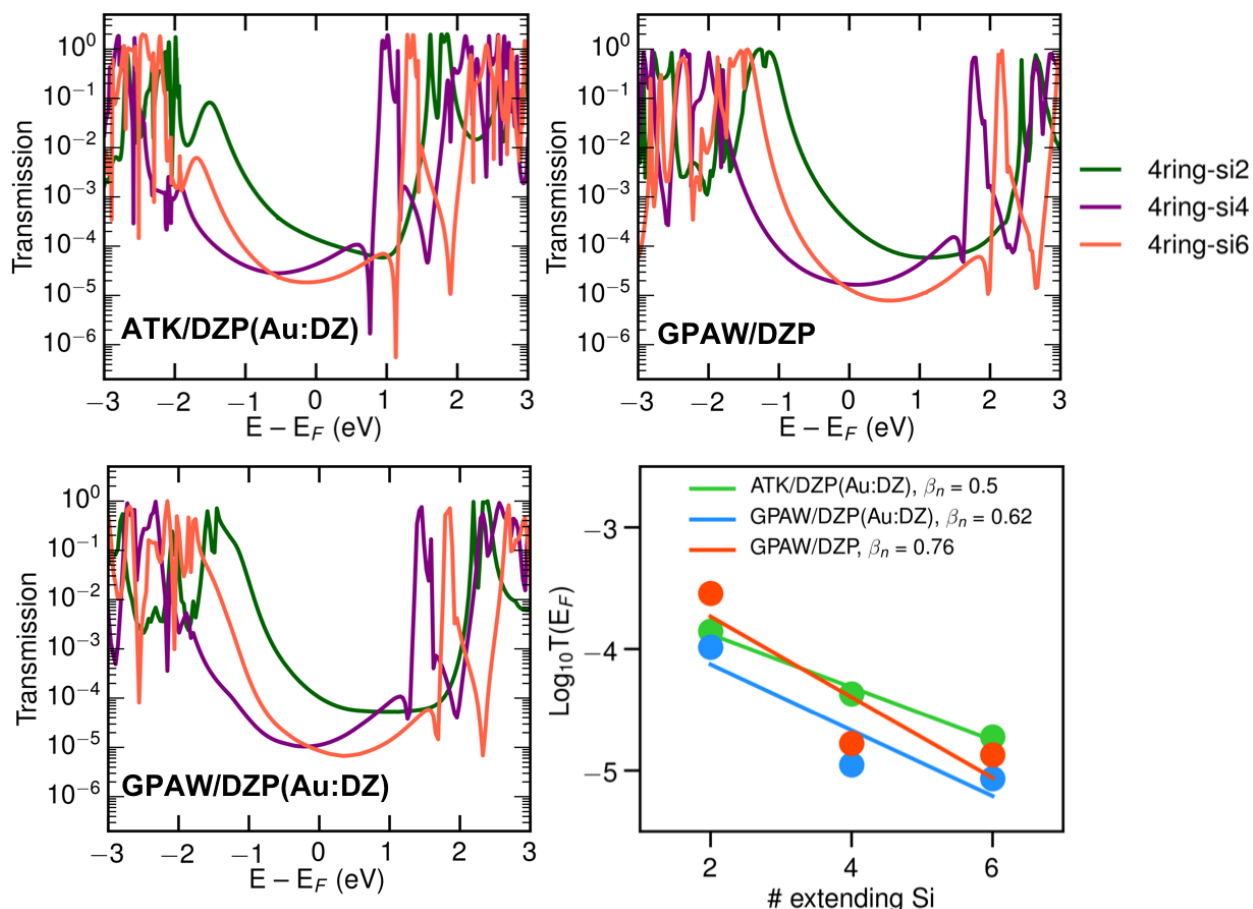


Figure S11. Transmission of the **4-ring** series calculated using ATK and GPAW with double- ζ plus polarization basis set for the atoms of the molecule, and double- ζ or double- ζ plus polarization basis set for the Au atoms.

The transmissions of **4-ring** series calculated using the three methods are shown in Figure S11. Qualitatively the three results are very similar. The most notable difference is the level alignment. For the ATK calculation the LUMO resonance is closer to the Fermi energy compared to the two GPAW calculations. This also affects the transmission at the

Fermi energy, and the odd-even alternation of the transmission at the Fermi energy is consequently more pronounced in the GPAW calculation, particularly when DZP basis set is used for all atoms.

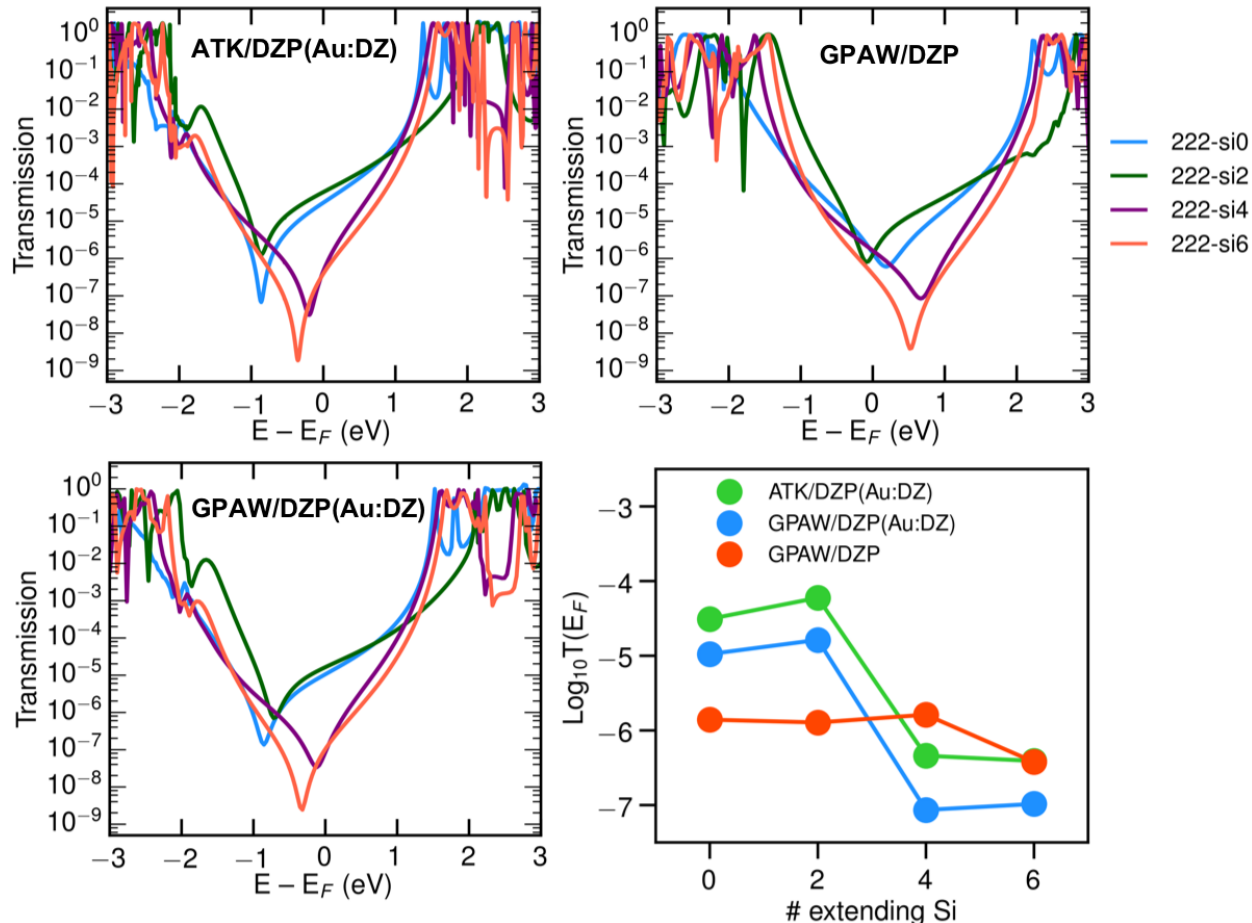


Figure S12. Transmission of the **222** series calculated using ATK and GPAW with double- ζ plus polarization basis set for the atoms of the molecule, and double- ζ or double- ζ plus polarization basis set for the Au atoms.

Figure S12 shows the transmissions of the **222** series calculated with the three different methods. The anti-resonances in the HOMO-LUMO gap are clear in all three cases. ATK and GPAW compare closely when the basis set is the same. However, if the basis set is changed, as in the case where DZP basis is used for all atoms in the junction, the energy of the anti-resonances changes considerably. The change in the transmission at the Fermi is very notable as the qualitative trend is changed due to the change of the anti-resonance energies. As the three methods are at a similar level and quality of theory, it is clear that DFT cannot predict the exact positions of resonances and anti-resonances.

Conformations and transmission

Here follows a brief presentation of the structures of each molecule and further discussion of the relation between single-molecule conductance and conformational freedom. These calculations are done with GPAW, using Double- ζ plus polarization basis set for all atoms in the junction.

221 and Linear Silanes

The central part of **221** (the “cage”) has no conformational freedom. We assume that the linkers couple into the short three-atom path to form an all-*transoid* path through the molecule, as illustrated in the top panel of Figure S13 where **221-Si6** is shown along the equivalent linear silane. We make this assumption based on the fact that both the measured conductance and the calculated transmissions of the **221** series are very close to those of linear silane series; the well-defined conductance trend measured for the linear series corresponds to that of a fully extended transoid conformation.⁵ The transmissions of the **221** series are plotted in the bottom panel of Figure S13.

We have also sampled other conformations where the arms couple into the more constrained pathways of the cage. Two examples of such conformations for **221-Si2** are shown alongside the transoid conformation in Figure S14. Structurally these conformations are more similar to **222** as the arms couple into the more constrained paths through the cage. Similar to **222**, the transmission is low for these conformations and there is odd-even alternation in the junction length as shown in Figure S15. The high conductance and lack of length alternation in the experiments support the assumption that the transoid conformation is dominant in experiment.

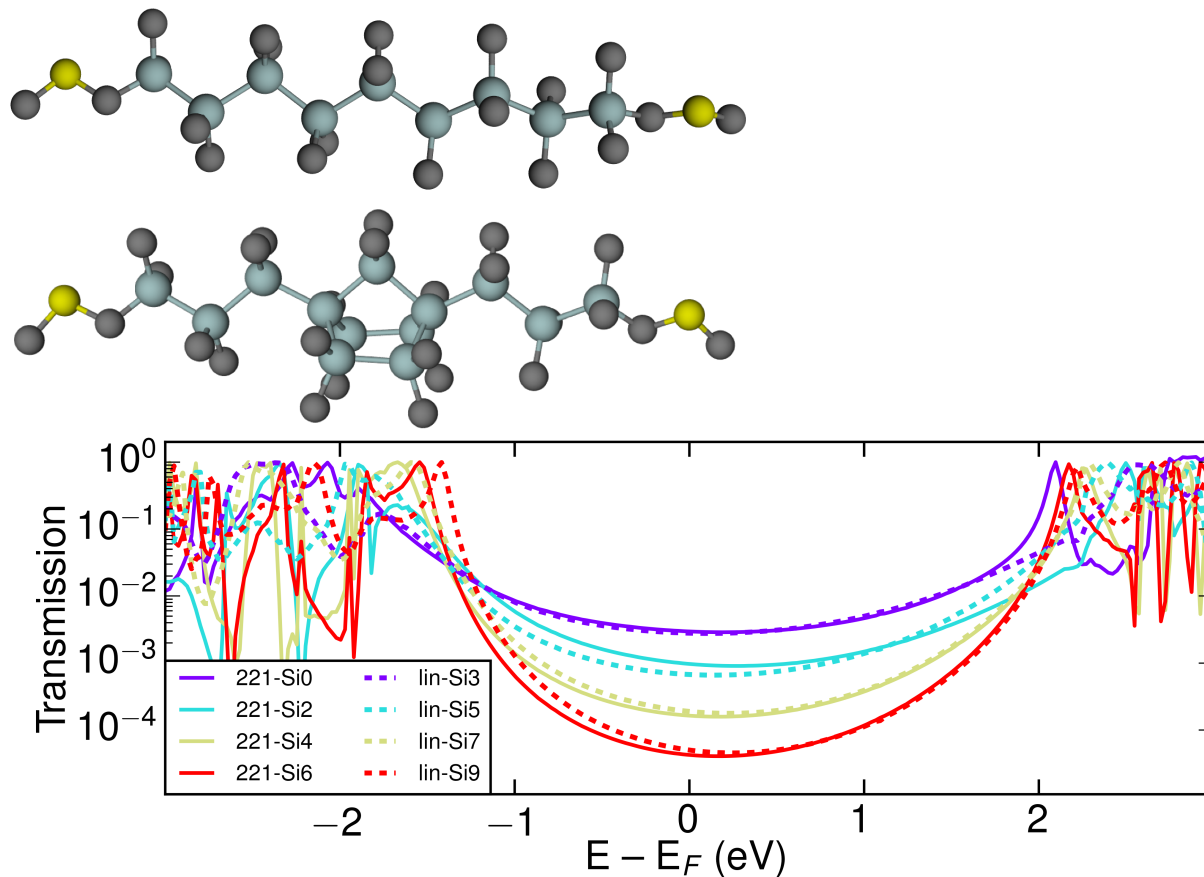
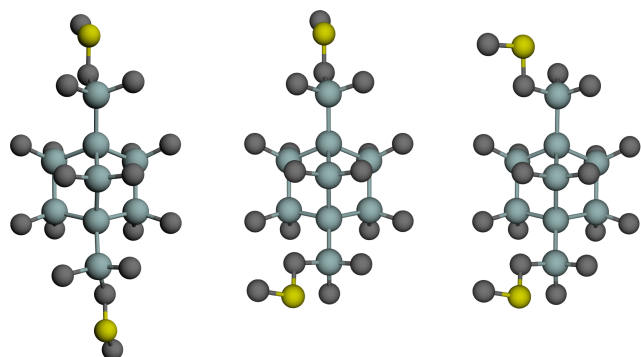


Figure S13. (top) Structures of all-*transoid* linear nonasilane (lin-Si9) and **221-Si6** optimized in vacuum. Hydrogen atoms are omitted for clarity. (bottom) Transmissions of **221** and linear silane series are plotted semi-logarithmically against energy.



Transoid 1-Gauche 2-Gauche

Figure S14. Optimized structures of three sampled conformations of **221-Si2**. Hydrogens are omitted for clarity.

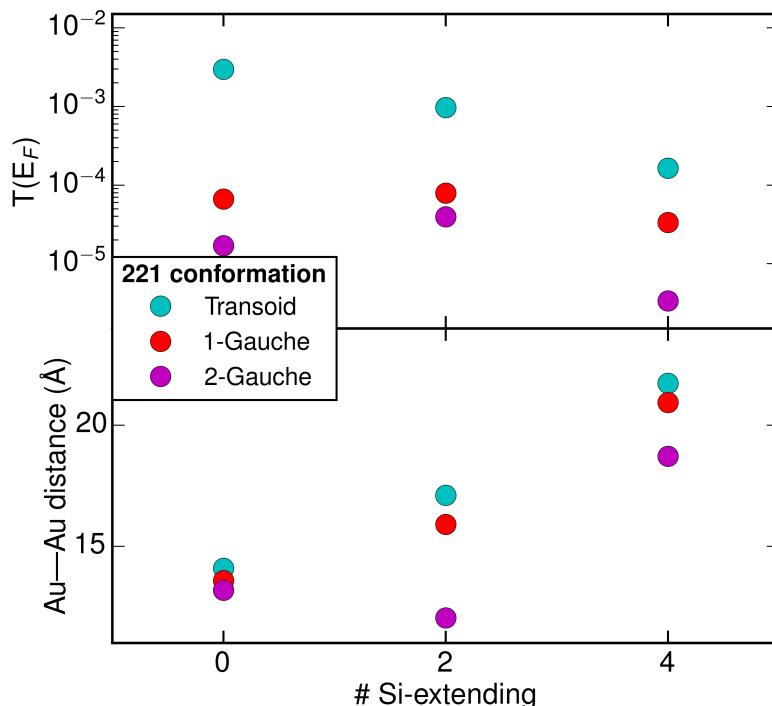


Figure S15. Transmissions at the Fermi energy are plotted semi-logarithmically (Top) and Au-Au distances are plotted linearly (bottom) against number of Si atoms in the extended arm of the three sampled conformations for the **221** series.

4-ring

The central part of **4-ring**, i.e. the “ring”, is very sterically crowded due to the TMS (trimethylsilicon) substituents. The ring is slightly bent, and thus the substituents are in slightly axial and equatorial positions. As we focus only on the trans isomer, this does not give rise to different conformations. We have sampled three different conformations of how the silane arms may couple into the ring (relative to each other). Again, we note that this is not a complete study of the conformational freedom of the molecules, but a sampling of the conformations that allows us to understand the transport properties of the molecules.

The structural difference of the conformations is illustrated in Figure S16, where the (nonsystematic) names relate to which way the C-Si-Si-Si dihedral couples into the ring in an *anti*-dihedral ($\sim 180^\circ$). Here they are illustrated for **4-ring-S12**, but the conformations are largely the same for the extended versions of the molecules.

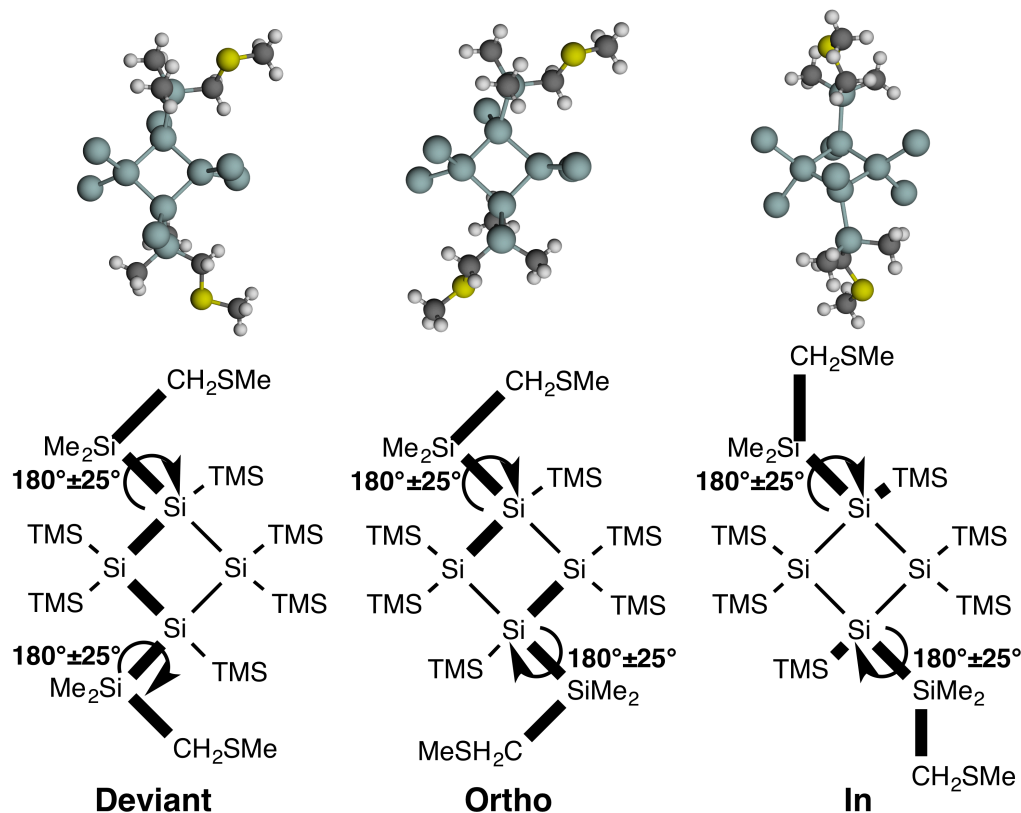


Figure S16. Optimized structure (top) and illustration (bottom) of the three conformations of **4-ring-Si₂** we have sampled. We define conformations based on which one of the two pathways the C-Si-Si-Si dihedrals couple into with a transoid dihedral. Methyls on TMS substituents are omitted for clarity.

In deviant conformation, the two arms couple the same way around the ring, meaning the lowest dihedrals are the two Si-Si-Si-Si dihedrals at approximately 110° and 130°. The Deviant conformation is the conformation that is closest to an all-*transoid* silane conformation. In ortho conformation, the Si-Si-Si-Si dihedrals are the same, but in the optimal path one of C-Si-Si-Si dihedrals is now in an *ortho*-configuration at approximately 75° as the two arms do not couple the same way around the ring. In the “In” conformation, none of the arms couple into the ring-paths, instead they are in *anti*-configuration with the neighboring TMS group. This means the arms point into the ring, but are not expected to couple well into the ring due to the constrained dihedrals. As listed in table S1, there is not one series of conformations that is expected to be dominant based on the calculated vacuum energies (no Au electrodes in the calculation). As the **4-ring** is a sterically crowded molecule, dispersion interactions may be significant to the relative energies. To test this, we have applied the dispersion energy correction scheme (TS09) by Tkatchenko and Scheffler.⁶ While this does present a change to the relative energies, it does not cause a change to which conformation is the most stable in any of the cases.

Table S1: Vacuum energies in eV relative to the most stable conformation, for the three conformations of **4-ring** series. PBE denotes the non-corrected energies. PBE+TS09 denotes the dispersion corrected energies.

	Si₂		Si₄		Si₆	
	PBE	PBE+TS09	PBE	PBE+TS09	PBE	PBE+TS09
Deviant	0.03	0.07	0.00	0.00	0.06	0.02
Ortho	0.05	0.09	0.05	0.08	0.00	0.00
In	0.00	0.00	0.17	0.12	0.28	0.20

While it is conceivable that more than one conformation has contributed to the experimental results, there are particular trends in the experimental results that make us believe that the deviant series is the main contributor. In particular, the measured conductance for the **4-ring** series is almost as high as that for the **221** series, and higher than that of the **5-ring** series. Furthermore, there is odd-even alternation in the conductance and junction lengths with increasing number of silicon atoms in the extending silicon arm. In the top panel of Figure S17 the transmissions for the three conformations reveal that in correspondence with optimal dihedrals, the Deviant conformation has the highest transmission. All three conformations show alternation in the transmission. However, as shown in the bottom panel of Figure S17, the length alternation is the clearest for the Deviant conformation. Considering these two notable trends are best reproduced with the Deviant conformation, this conformation is the one we have focused on in the manuscript. The full transmission plots for Deviant conformation are shown in Figure S18.

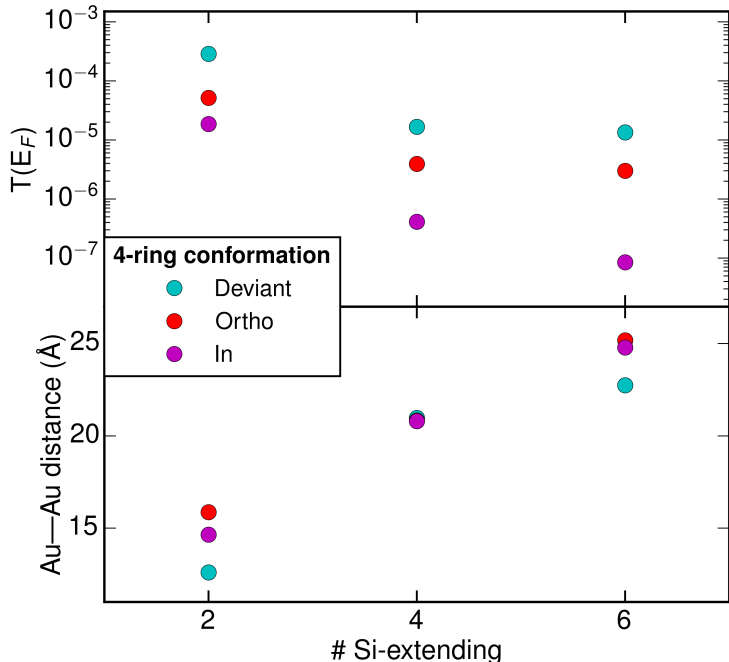


Figure S17. Transmissions at the Fermi energy are plotted semi-logarithmically (Top) and Au-Au distances are plotted linearly (bottom) against number of Si atoms in the extended arms of the three conformations for **4-ring** series.

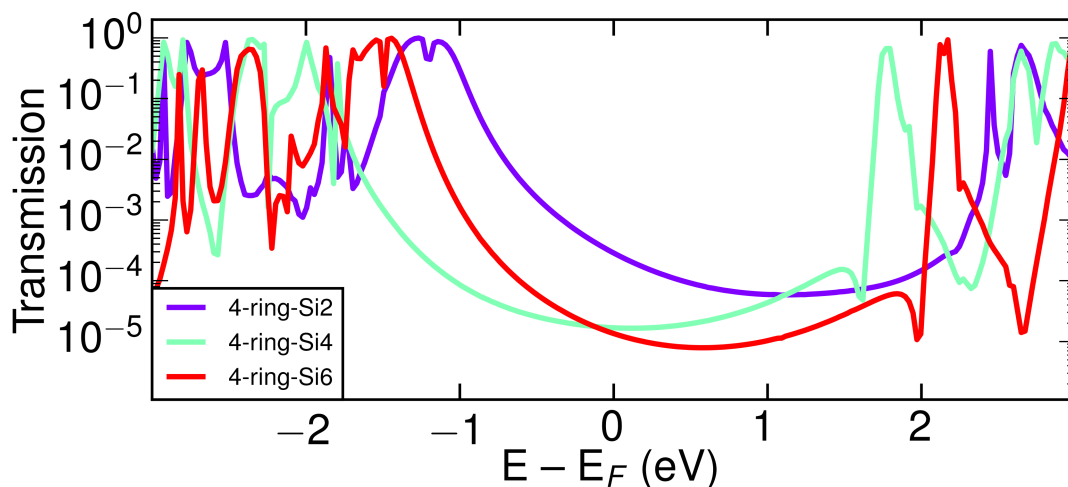


Figure S18. Transmissions plotted semi-logarithmically against energy for the deviant conformation of **4-ring**.

5-ring

As we have described previously, the conformational freedom in **5-ring** is immense, with 93 potential conformers in the ring alone.⁷ Considering there is also conformational flexibility in the arms, a complete conformational analysis is not a feasible approach. Based on our previous studies we have screened for conformations of the extended **5-ring** molecules, with the intention of exploring how the conductance trends of the molecules relate to their structures. Consequently, we only consider a few selected conformations in this study, though it is conceivable that many conformations contribute to the experimental results.

As described in the manuscript, at first glance the fact that the measured conductance of **4-ring** is higher than that for **5-ring** seems to go against the expected structure-function relationship that more constrained dihedrals give lower conductance. Both **4-ring** and **5-ring** have a three-atom silicon-path in the ring. Considering the two Si-Si-Si-Si dihedrals coupled into the ring, the dihedrals of **5-ring** are both around 130° . In comparison, one of the two dihedrals for **4-ring** is only around 110° . The next Si-Si-Si-Si dihedral (one step further away from the ring on each side) in both **4-ring** and **5-ring** is much more conformational dependent, and a large subset of the available conformations of **5-ring** have suboptimal dihedrals thus possibly nullifying the slightly more transoid dihedrals in the central part of **5-ring**. This correlation between the backbone dihedrals and σ -conjugation is directly mirrored in the calculated transmission. Figure S19 shows the transmissions where the **5-ring** conformation with optimal dihedrals is compared to a suboptimal conformation and the deviant conformation of **4-ring**. These results are a reminder that idealized conformations often used in theoretical models may not mirror the experimental reality, and a different set of conformations may be sampled.

In reference to our previous work, the **5-ring** with the highest transmission corresponds to a twist conformation, and is an extended version of the conformations we previously gave the systematic name `2twist_u2`.⁷ The conformation we focus on in the manuscript is also a `2twist` conformation following the previously used definitions, but is really close to a slightly distorted version of `1envelope_b4`, which was found to be the second-most abundant conformation of the non-extended system. The full transmission plots for this conformation are shown in Figure S20.

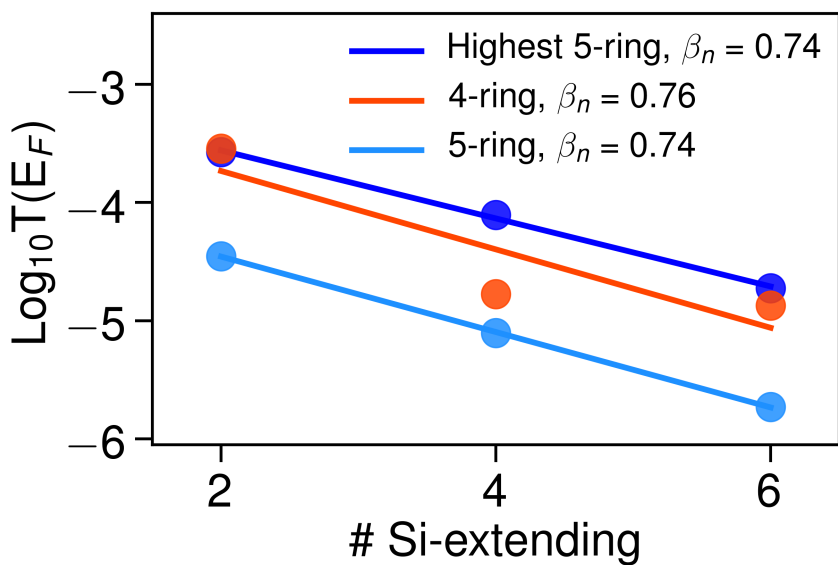


Figure S19. Transmissions at the Fermi energy plotted semi-logarithmically against the number of extending silicon atoms for the deviant conformation of **4-ring**, and for the two sampled conformations of **5-ring** (with optimal and suboptimal dihedrals).

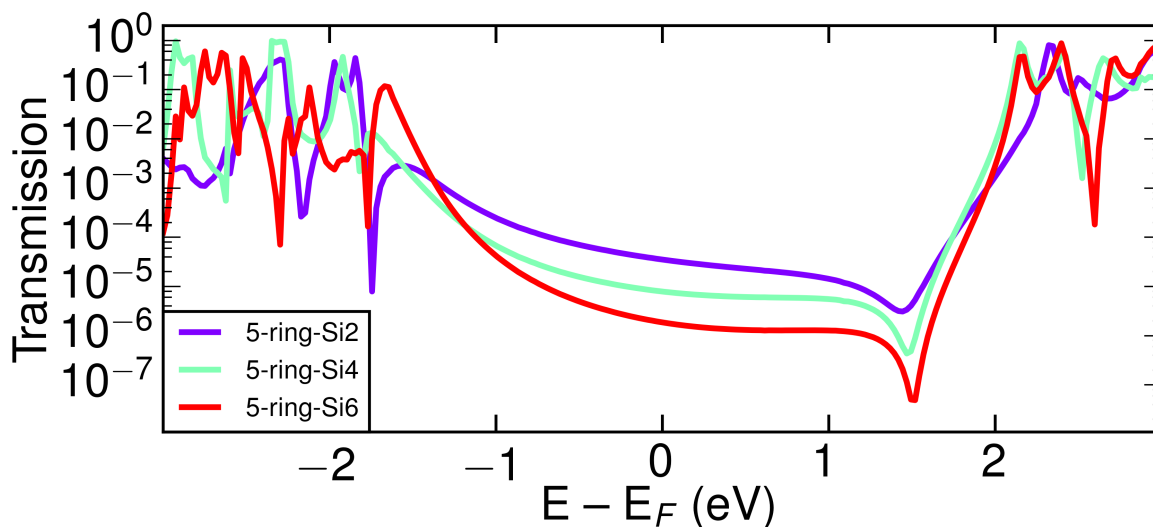


Figure S20. Transmissions plotted semi-logarithmically against energy for the suboptimal conformation of **5-ring**.

222

Due to the high symmetry of the central cage of **222**, the dihedrals coupling the linkers into the cage give rise to three different conformations. These are illustrated in Figure S21 for **222-Si2**, where it is the C-Si-Si-Si dihedral that determines the conformation. The name is given by considering the dihedral of one of the linkers coupling into the bridge of the cage where the other linker couples into the cage by an anti-dihedral. Due to symmetry, this dihedral is the same no matter which of the two linkers is chosen as a reference. In all cases, all the four-atom paths through the cage have Si-Si-Si-Si dihedrals between 16° and 23° (depending on the conformation). As listed in table S2, the energy differences between conformations in vacuum are negligible in all cases.

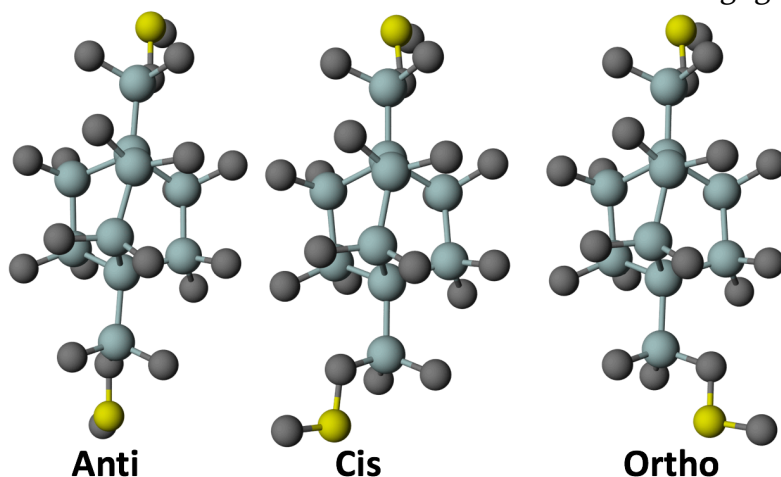


Figure S21. Optimized structures of the three conformations of **222-Si2**. Hydrogen atoms are omitted for clarity.

Table S2: Vacuum energies in eV relative to that of the most stable conformation for the three conformations of **222** series.

	Si0	Si2	Si4	Si6
anti	0.012	0.000	0.008	0.000
cis	0.005	0.000	0.003	0.006
ortho	0.000	0.005	0.000	0.001

In the manuscript we have only included the data from the anti conformation. All three conformations show similar results, both in junction length and transmission. Shown in Figure S22, alternation is the strongest for the anti conformation, but is present in all three cases. The length alternation is present due to the same structural features as in **4-ring**. This is visualized in Figure S23, where the junction structures for the anti conformation are visualized.

The transmissions of the three conformations are qualitatively very similar. The transmission plots for cis and ortho conformations are shown in Figure S24 and S25. Considering the similar energy, transmission and length alternation features in all three conformations, it is possible that all three conformations contribute to the experimental results.

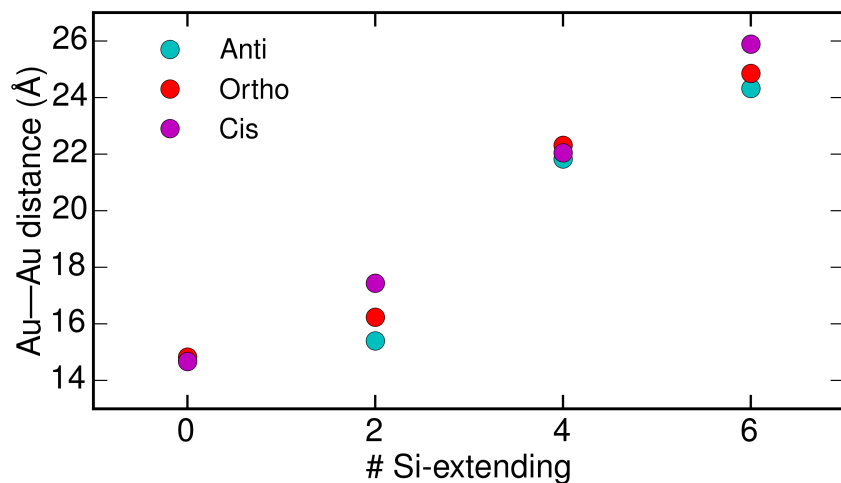


Figure S22. Au-to-Au distance is plotted linearly against number of Si in the extended arm for the three conformations of **222**.

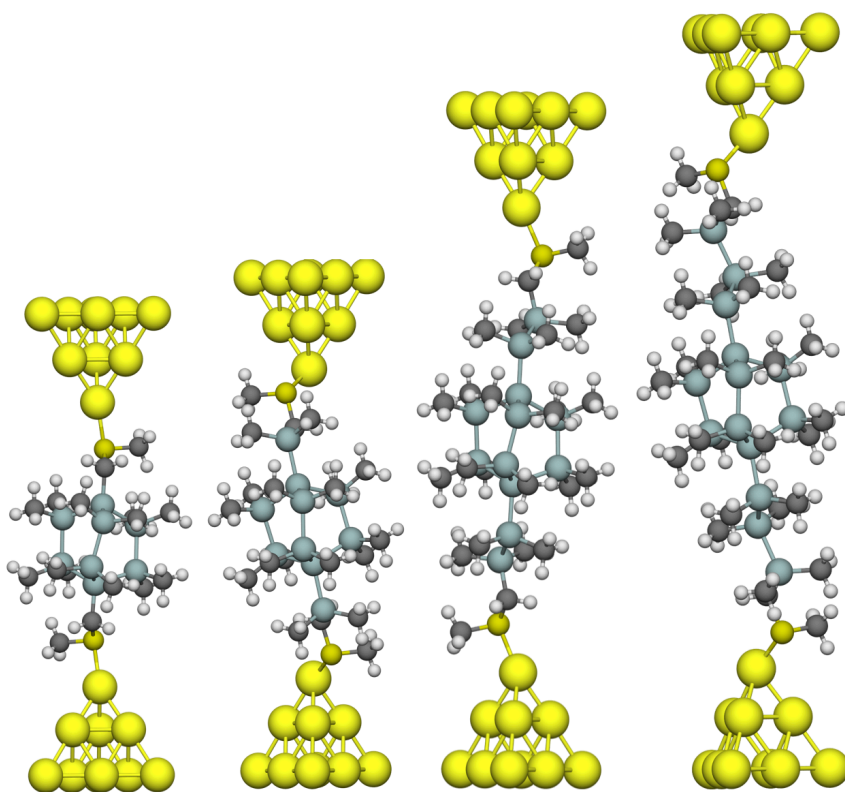


Figure S23. Junction structures for the series $n = 0, 2, 4, 6$ for the anti-conformation of **222**. Corresponding length data are presented in **Figure 4** in the manuscript.

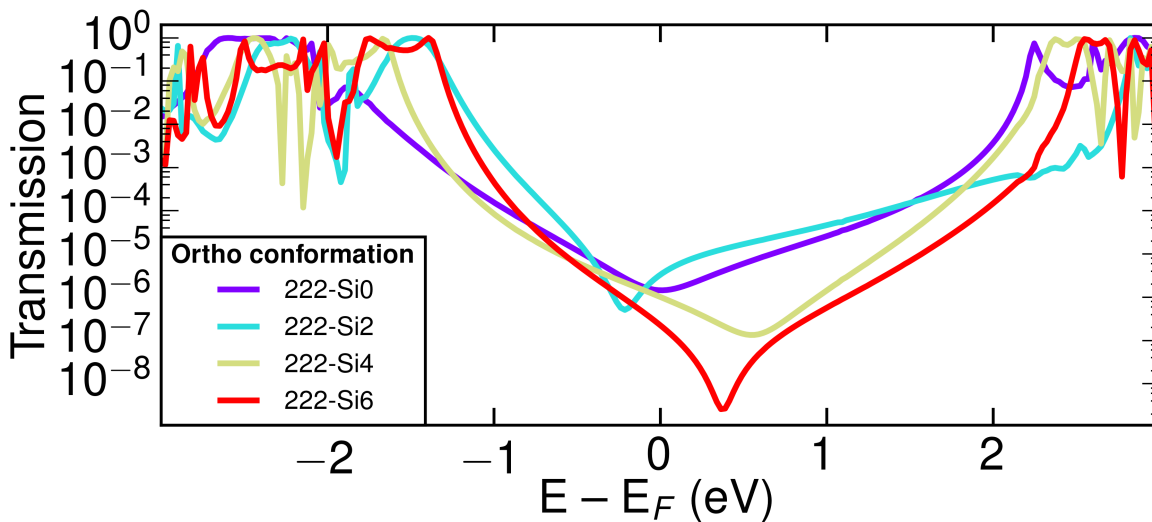


Figure S24. Transmissions plotted semi-logarithmically against energy for the ortho conformation of 222.

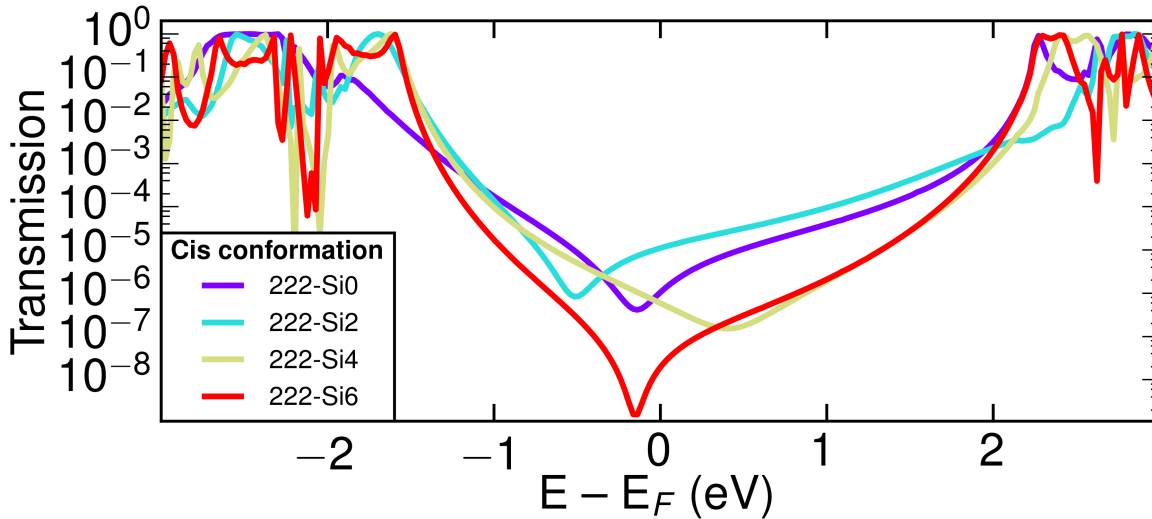


Figure S25. Transmissions plotted semi-logarithmically against energy for the cis conformation of 222.

IV. Synthetic Procedures and Characterization of Compounds

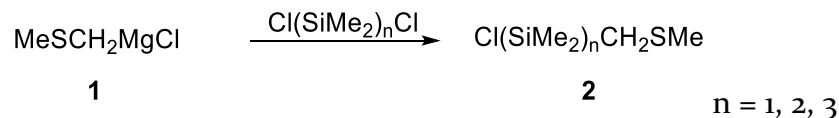
All reactions were performed in oven-dried or flame-dried round bottom flasks unless otherwise noted. The flasks were fitted with rubber septa and reactions were conducted under a positive pressure of nitrogen or argon unless otherwise noted. Anhydrous and anaerobic solvents were obtained from PureSolv MD5 solvent purification system.

Materials. Commercial reagents were used without further purification. ClSiMe₂Cl and 18-crown-6 were purchased from Adamas-beta[®]. Potassium tert-butoxide were purchased from J&K Chemical Ltd. All other reagents were purchased from TCL.

Instrumentation. ¹H, ¹³C, and ²⁹Si NMR spectra were recorded on a Bruker DRX300 (300 MHz), Bruker DRX400 (400 MHz) or a Bruker DMX500 (500 MHz) spectrometer. Chemical shifts for protons are reported in parts per million (ppm) downfield from tetramethylsilane and are referenced to residual proton in the NMR solvent (CHCl₃; δ 7.26). Chemical shifts for carbon are reported in ppm downfield from tetramethylsilane and are referenced to the carbon resonances of the solvent (CDCl₃; δ 77.0). Chemical shifts for silicon are reported in ppm downfield from tetramethylsilane and referenced to the silicon resonance of tetramethylsilane (TMS; δ 0.0). Data are represented as follows: chemical shift, multiplicity (s = singlet, d = doublet, dd = doublet of doublets, t = triplet, m = multiplet), coupling constants in Hertz, and integration.

The mass spectroscopic data were obtained at the Columbia University mass spectrometry facility using a JEOL JMSHX110A/110A tandem mass spectrometer, fast atom bombardment (FAB+), or Shanghai institute of Organic Chemistry Chinese Academic of Sciences using a Thermo Fisher Scientific LTQ FTICR-MS, direct analysis in real time (DART).

Methylthiomethyl linkers were synthesized according to modified literature procedures.⁸ The anchoring of methylthiomethyl arms onto the silanes were performed according to modified literature procedures.^{5, 9}



The solution of **1** (1 equiv.) was added dropwise to dichlorodisilane (1 equiv.) in THF (0.6 M) at room temperature. After the addition of **1** was complete, the mixture was heated under reflux for 6 h. THF was removed under reduced pressure. The residue was extracted with hexane. The hexane solution was then filtered over Celite through a Schlenk filter into a Schlenk flask. The hexane was removed under vacuum and the crude compound was distilled to yield a light-yellow oil.

n = **1**: light yellow oil distilled at 40 °C, 20 Pa. ¹H NMR (CDCl₃, 400 MHz) δ 2.20 (s, 3H), 2.04 (s, 2H), 0.52 (s, 6H). ¹³C NMR (101 MHz, CDCl₃) δ 22.44, 19.70, 1.34. ²⁹Si NMR (CDCl₃, 79 MHz) δ 25.96. HRMS could not be obtained due to the sensitivity of the compound.

n = 2: light yellow oil distilled at 80°C, 20 Pa. ¹H NMR (400 MHz, C₆D₆) δ 1.84 (s, 3H), 1.69 (s, 2H), 0.45 (s, 6H), 0.19 (s, 6H). ¹³C NMR (101 MHz, C₆D₆) δ 20.39, 19.27, 2.75, -4.50. ²⁹Si NMR (79 MHz, C₆D₆) δ 22.76, -16.50. HRMS could not be obtained due to the sensitivity of the compound.

n = 3: light yellow oil distilled at 105°C, 20 Pa. ¹H NMR (CDCl₃, 400 MHz) δ 2.17 (s, 3H), 1.93 (s, 2H), 0.53 (s, 6H), 0.23 (s, 6H), 0.22 (s, 6 H). ¹³C NMR (101 MHz, CDCl₃) δ 20.63, 20.58, 3.11, -3.35, -6.95. ²⁹Si NMR (79 MHz, CDCl₃) δ 27.17, -14.38, -45.75. HRMS could not be obtained due to the sensitivity of the compound.



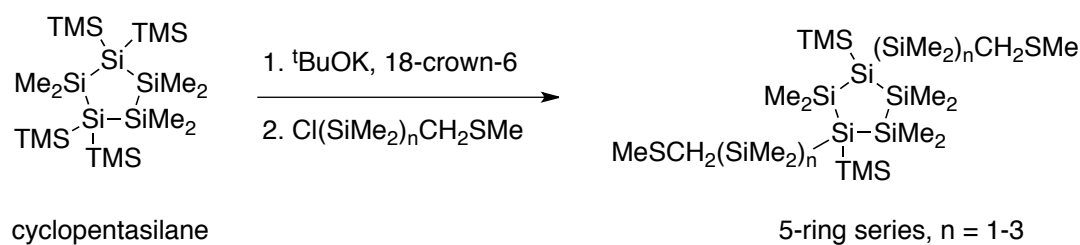
Cyclotetrasilane^{10, 11} (1.0 equiv.), *t*-BuOK (2.0 equiv.) and 18-crown-6 (2.0 equiv.) were dissolved in toluene (50 mL) at room temperature. Immediately the solution turned orange. The mixture was stirred overnight to give the silanylpotassium/18-crown-6. Then a solution of thiomethylmethylsilyl linker **2** (2.0 equiv.) in toluene (20 mL) was added dropwise to the silanylpotassium/18-crown-6 solution. After complete addition, the orange color of the silyl anion vanished. The reaction mixture was stirred at room temperature for 4 h and was then subjected to an aqueous workup with 2 M H₂SO₄. After removal of the solvent, the crude residue was purified by silica gel chromatography. The reaction produced nearly 1:1 *trans*- and *cis*-stereoisomers that are separable by silica gel column chromatography.

n = 1: purified by silica chromatography with a gradient from 100 % hexanes to 80/20 hexanes/dichloromethane (v/v). **trans** white solid (37% yield). ¹H NMR (400 MHz, CDCl₃) δ 2.17 (s, 6H), 2.05 (s, 4H), 0.42 (s, 12H), 0.35 (s, 54H). ¹³C NMR (101 MHz, CDCl₃) δ 23.62, 20.14, 4.42, 1.10. ²⁹Si NMR (79 MHz, CDCl₃) δ -8.05, -8.88, -91.22, -91.41. HRMS (FAB+): calculated for C₂₆H₇₆S₂Si₁₂ 788.26, found [M+H]⁺ 789.27.

n = 2: purified by silica chromatography with a gradient from 100 % hexanes to 80/20 hexanes/dichloromethane (v/v). **trans** white solid (32% yield). ¹H NMR (400 MHz, CDCl₃) δ 2.15 (s, 6H), 1.93 (s, 4H), 0.47 (s, 12H), 0.36 (s, 54H), 0.25 (s, 12H). ¹³C NMR (101 MHz, CDCl₃) δ 21.83, 20.54, 5.07, 4.82, 1.93, -1.56. ²⁹Si NMR (79 MHz, CDCl₃) δ -14.47, -35.06, -37.18, -126.44. HRMS (FAB+): calculated for C₃₀H₈₈S₂Si₁₄ 904.31, found [M-CH₃]⁺ 889.28.

n = 3: purified by silica chromatography with a gradient from 100 % hexanes to 80/20 hexanes/dichloromethane (v/v). **trans** white solid (36% yield). ¹H NMR (400 MHz, CDCl₃) δ 2.16 (s, 6H), 1.91 (s, 4H), 0.50 (s, 12H), 0.35 (s, 54H), 0.26 (s, 12H), 0.21 (s, 12H). ¹³C NMR (101 MHz, CDCl₃) δ 21.21, 20.64, 5.20, 4.97, 3.73, -2.81, -2.87. ²⁹Si NMR (79 MHz,

CDCl₃) δ -11.30, -30.43, -35.62, -75.59, -82.98. HRMS (FAB+): calculated for C₃₄H₁₀₀S₂Si₁₆ 1020.36, found [M-CH₃]⁺ 1005.33.

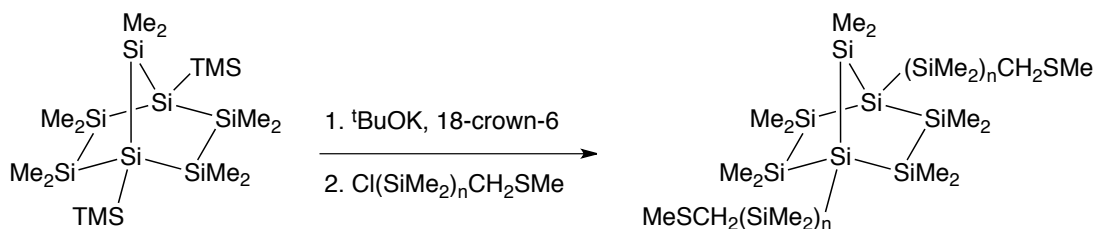


At room temperature cyclopentasilane⁷ (500 mg, 0.955 mmol), *t*-BuOK (214 mg, 1.91 mmol) and 18-crown-6 (505 mg, 1.91 mmol) are reacted in 5 mL of toluene. Immediately the solution turned orange. The mixture was stirred overnight to give the silanylpotassium 18-crown-6 in toluene. Then a solution of thiomethylmethylsilyl linker **2** (2 equiv.) in toluene (3 mL) is added dropwise to the silanylpotassium solution. After complete addition, the orange color of the silyl anion vanishes. The reaction mixture is stirred at room temperature for 4 h and is then subjected to an aqueous workup with 2 M H₂SO₄. After removal of the solvent, the crude residue was purified by silica gel chromatography. The reaction produces nearly 1:1 *trans*- and *cis*-stereoisomers that are separable by silica gel column chromatography.

n = 1: purified by silica chromatography with a gradient from 100% hexanes to 80/20 hexanes/dichloromethane (v/v). **trans** white solid (35 % yield). ¹H NMR (400 MHz, CDCl₃) δ 2.16 (s, 6H), 1.95 (s, 4H), 0.50 (s, 6H), 0.33 (s, 6H), 0.32 (s, 6H), 0.31 (s, 12H), 0.24 (s, 18H). ¹³C NMR (126 MHz, CDCl₃) δ 24.04, 20.52, 4.05, 3.74, 1.22, 1.20, -1.75, -2.17. ²⁹Si NMR (60 MHz, CDCl₃) δ -5.52, -7.47, -19.12, -24.42, -129.02. HRMS (DART+): calculated for C₂₀H₅₈S₂Si₉ 614.1903, found [M+H]⁺ 615.1976.

n = 2: purified by silica chromatography with a gradient from 100% hexanes to 80/20 hexanes/dichloromethane (v/v). **trans** white solid (37% yield). ¹H NMR (400 MHz, CDCl₃) δ 2.17 (s, 6H), 1.93 (s, 4H), 0.51 (s, 6H), 0.35 (s, 6H), 0.33 (s, 6H), 0.32 (s, 12H), 0.24 (s, 12H), 0.23 (s, 18H). ¹³C NMR (126 MHz, CDCl₃) δ 20.87, 20.59, 4.61, 4.03, -0.47, -1.29, -1.88, -2.95, -2.99. ²⁹Si NMR (60 MHz, CDCl₃) δ -8.10, -13.83, -16.34, -23.19, -35.25, -125.27. HRMS (DART+): calculated for C₂₄H₇₀S₂Si₁₁ 730.2381, found [M+H]⁺ 731.2454.

n = 3: purified by silica chromatography with a gradient from 100% hexanes to 80/20 hexanes/dichloromethane (v/v). **trans** white solid (37% yield). ¹H NMR (400 MHz, CDCl₃) δ 2.16 (s, 6H), 1.91 (s, 4H), 0.51 (s, 6H), 0.38 – 0.34 (m, 18H), 0.32 (s, 6H), 0.25 (d, J = 2.9 Hz, 12H), 0.23 (s, 18H), 0.20 (s, 12H). ¹³C NMR (101 MHz, CDCl₃) δ 21.08, 20.64, 4.66, 4.13, 1.09, 0.87, -1.17, -1.73, -2.99, -3.01, -4.60, -4.76. ²⁹Si NMR (79 MHz, CDCl₃) δ -8.16, -12.54, -16.48, -22.96, -30.13, -41.91, -123.38. HRMS (DART+): calculated for C₂₈H₈₂S₂Si₁₃ 846.2858, found [M+H]⁺ 847.2931.



bicyclo[2.2.1]heptasilane

bicyclo[2.2.1]silane series, $n = 0\text{-}3$

At room temperature bicyclo[2.2.1]heptasilane¹² (500 mg, 1.01 mmol), *t*-BuOK (0.267 g, 2.02 mmol) and 18-crown-6 (0.534 g, 2.02 mmol) were reacted in 20 mL of toluene. Immediately the solution turned orange. The mixture was stirred overnight. Then a solution of the silanylpotassium/18-crown-6 in toluene was added dropwise to a solution of thiomethylmethylsilyl linker **2** (2.0 equiv.) in 40 mL of toluene at $-78\text{ }^\circ\text{C}$. After addition, the reaction mixture was stirred for 4 h while warm to room temperature. It was subjected to an aqueous workup with toluene and 2 M H_2SO_4 . After removal of the solvent, the crude residue was purified by silica gel chromatography.

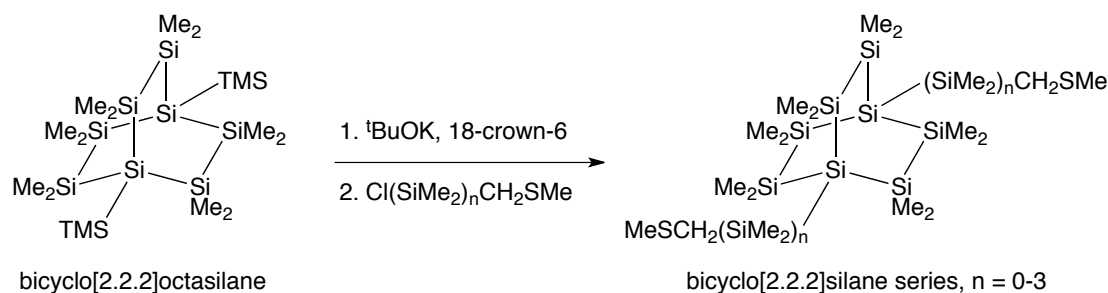
n = 0: purified with a gradient from 100% hexanes to 70/30 hexanes/dichloromethane (v/v), white solid (33% yield). ^1H NMR (400 MHz, CDCl_3) δ 2.24 (s, 6H), 2.23 (s, 4H), 0.48 (s, 6H), 0.39 (s, 24H). ^{13}C NMR (126 MHz, CDCl_3) δ 21.48, 13.64, -1.90 , -2.52 , -3.40 . ^{29}Si NMR (60 MHz, CDCl_3) δ -32.72 , -37.57 , -71.47 .

n = 1: purified with a gradient from 100% hexanes to 70/30 hexanes/dichloromethane (v/v), white solid (45% yield). ^1H NMR (400 MHz, CDCl_3) δ 2.18 (s, 6H), 1.95 (s, 4H), 0.43 (s, 6H), 0.32 (s, 12H), 0.30 (s, 24H). ^{13}C NMR (126 MHz, CDCl_3) δ 23.89, 20.57, 1.15, 0.68, -0.82 , -1.82 . ^{29}Si NMR (60 MHz, CDCl_3) δ -3.88 , -17.01 , -31.71 , -122.78 . HRMS (FAB⁺): calculated for $\text{C}_{18}\text{H}_{52}\text{S}_2\text{Si}_9$ 584.14, found $[\text{M}+\text{H}]^+$ 585.15.

n = 2: purified with a gradient from 100% hexanes to 70/30 hexanes/dichloromethane (v/v), white solid (47% yield). ^1H NMR (400 MHz, CDCl_3) δ 2.17 (s, 6H), 1.93 (s, 4H), 0.48 (s, 6H), 0.31 (d, $J = 3.0$ Hz, 24H), 0.29 (s, 12H), 0.21 (s, 12H). ^{13}C NMR (126 MHz, CDCl_3) δ 20.73, 20.60, 1.67, -0.56 , -0.97 , -1.50 , -3.50 . ^{29}Si NMR (60 MHz, CDCl_3) δ -12.18 , -14.74 , -31.77 , -33.62 , -122.67 ; HRMS (FAB⁺): calculated for $\text{C}_{22}\text{H}_{64}\text{S}_2\text{Si}_{11}$ 700.20, found $[\text{M}+\text{H}]^+$ 701.20.

n = 3: purified with a gradient from 100% hexanes to 70/30 hexanes/dichloromethane (v/v), white solid (53% yield). ^1H NMR (400 MHz, CDCl_3) δ 2.16 (s, 6H), 1.92 (s, 4H), 0.49 (s, 6H), 0.34 (s, 12H), 0.32 (s, 12H), 0.29 (s, 12H), 0.21 (s, 12H), 0.20 (s, 12H). ^{13}C NMR (101 MHz, CDCl_3) δ 21.15, 20.63, 1.94, 0.27, -0.45 , -1.35 , -2.93 , -5.18 . ^{29}Si NMR (79 MHz, CDCl_3) δ

-11.80, -27.64, -31.87, -38.13, -43.83, -121.13. HRMS (FAB+): calculated for $C_{26}H_{76}S_2Si_{13}$ 816.21, found $[M-CH_3]^+$ 801.20.



At room temperature bicyclo[2.2.2]octasilane¹² (500 mg, 1.01 mmol), *t*-BuOK (0.267 g, 2.02 mmol) and 18-crown-6 (0.534 g, 2.02 mmol) are reacted in 20 mL of toluene. Immediately the solution turned orange. The mixture was stirred overnight. Then a solution of the silanylpotassium/18-crown-6 in toluene was added dropwise to a solution of thiomethylmethylsilyl linker **2** (2.0 equiv.) in 40 mL in 40 mL of toluene at -78 °C. The reaction mixture was stirred for 4 h with warming to room temperature. It was subjected to an aqueous workup with toluene and 2 M H_2SO_4 . After removal of the solvents, the crude residue was purified by silica gel chromatography.

n = 0: purified with a gradient from 100% hexanes to 70/30 hexanes/dichloromethane (v/v), white solid (40% yield). 1H NMR (400 MHz, $CDCl_3$) δ 2.18 (s, 4H), 2.18 (s, 6H), 0.31 (s, 36H). ^{13}C NMR (126 MHz, $CDCl_3$) δ 22.07, 15.00, -2.66. ^{29}Si NMR (60 MHz, $CDCl_3$) δ -39.32, -75.79; HRMS (FAB+): calculated for $C_{16}H_{46}S_2Si_8$ 526.12, found $[M+H]^+$ 527.13.

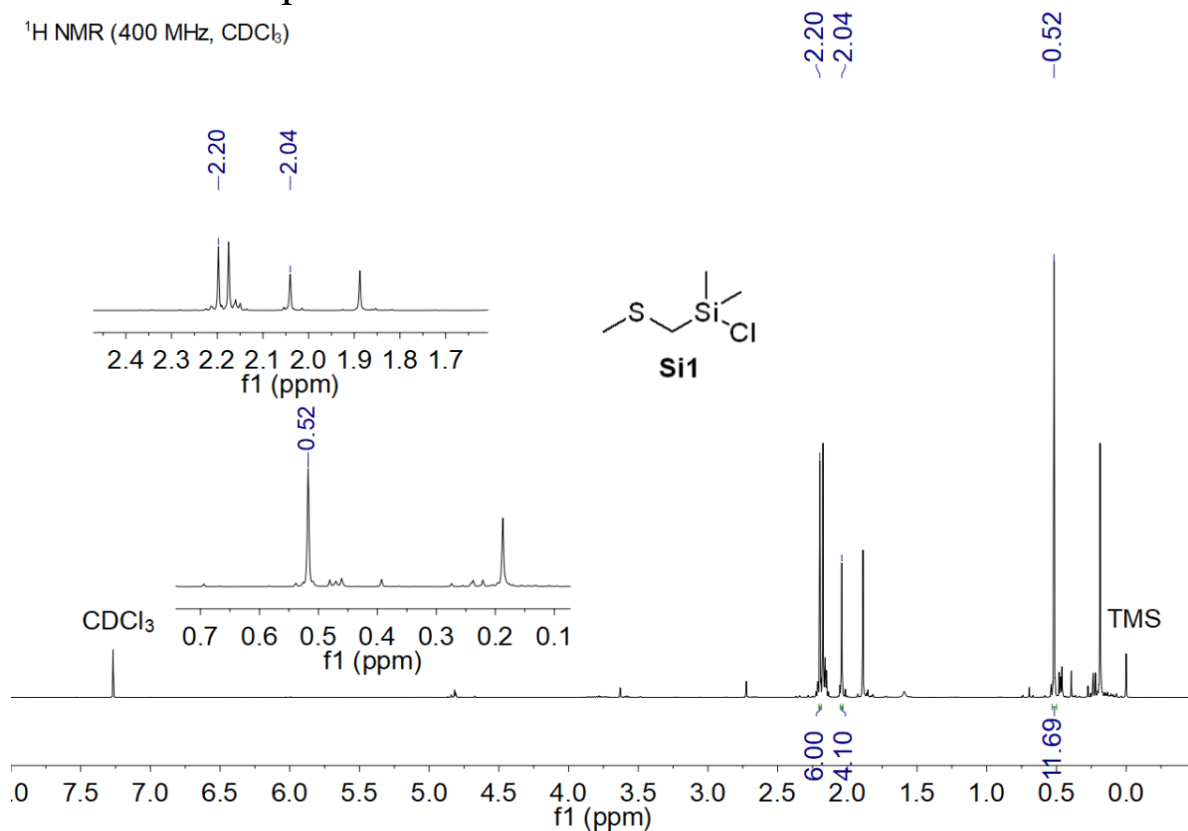
n = 1: purified with a gradient from 100% hexanes to 70/30 hexanes/dichloromethane (v/v), white solid (49% yield). 1H NMR (400 MHz, $CDCl_3$) δ 2.19 (s, 6H), 1.98 (s, 4H), 0.35 (s, 12H), 0.32 (s, 36H). ^{13}C NMR (126 MHz, $CDCl_3$) δ 23.93, 20.59, 1.12, -1.05. ^{29}Si NMR (60 MHz, $CDCl_3$) δ -4.72, -38.04, -129.99. HRMS (FAB+): calculated for $C_{20}H_{58}S_2Si_{10}$ 642.17, found $[M+H]^+$ 643.17.

n = 2: purified with a gradient from 100% hexanes to 70/30 hexanes/dichloromethane (v/v), white solid (47% yield). 1H NMR (400 MHz, $CDCl_3$) δ 2.16 (s, 6H), 1.93 (s, 4H), 0.33 (s, 12H), 0.31 (s, 36H), 0.23 (s, 12H). ^{13}C NMR (126 MHz, $CDCl_3$) δ 20.75, 20.57, -0.55, -0.69, -3.24. ^{29}Si NMR (60 MHz, $CDCl_3$) δ -14.47, -35.06, -37.17, -126.40. HRMS (FAB+): calculated for $C_{24}H_{70}S_2Si_{12}$ 758.22, found $[M+H]^+$ 759.22.

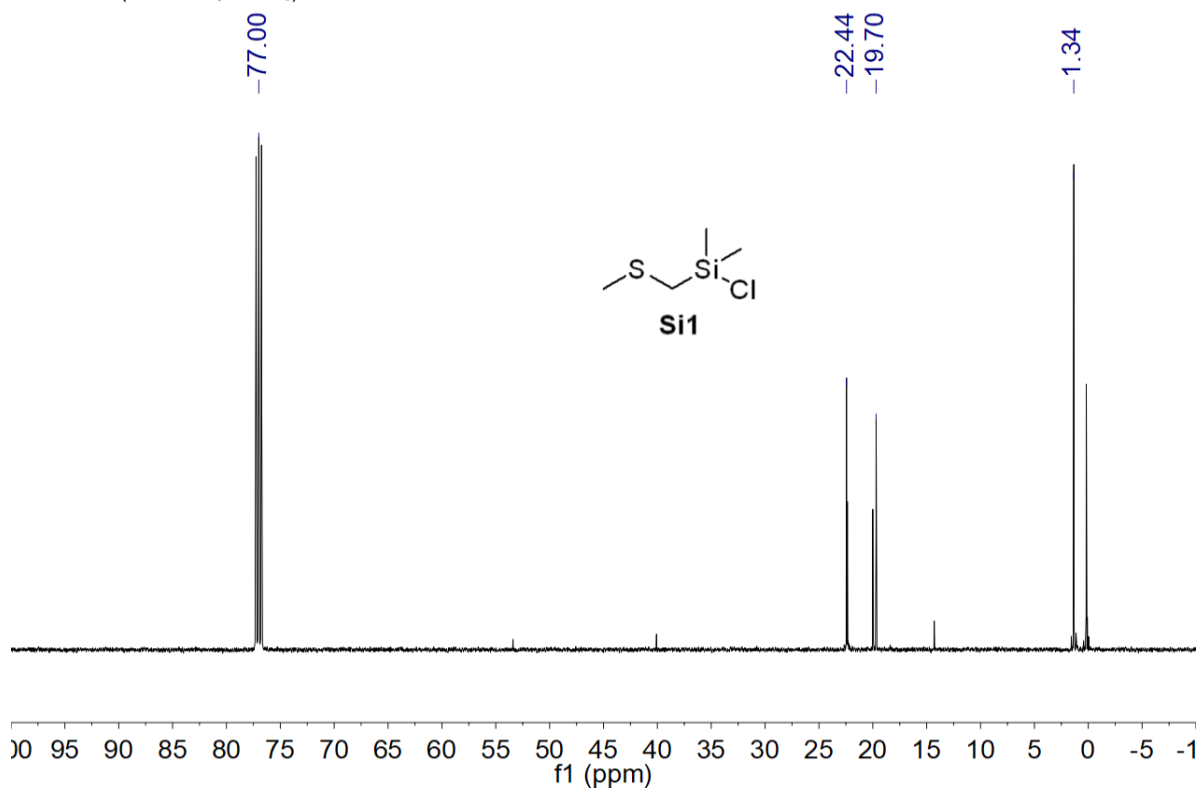
n = 3: purified with a gradient from 100% hexanes to 70/30 hexanes/dichloromethane (v/v), white solid (47% yield). 1H NMR (400 MHz, $CDCl_3$) δ 2.16 (s, 6H), 1.92 (s, 4H), 0.37 (s, 12H), 0.31 (s, 36H), 0.23 (s, 12H), 0.20 (s, 12H). ^{13}C NMR (101 MHz, $CDCl_3$) δ 21.15, 20.62, 0.84, -0.50, -2.88, -4.71. ^{29}Si NMR (79 MHz, $CDCl_3$) δ -8.42, -29.21, -36.62, -42.26, -123.77. HRMS (FAB+): calculated or $C_{28}H_{82}S_2Si_{14}$ 874.26, found $[M-CH_3+H]^+$ 860.24.

V. NMR spectra

¹H NMR (400 MHz, CDCl₃)

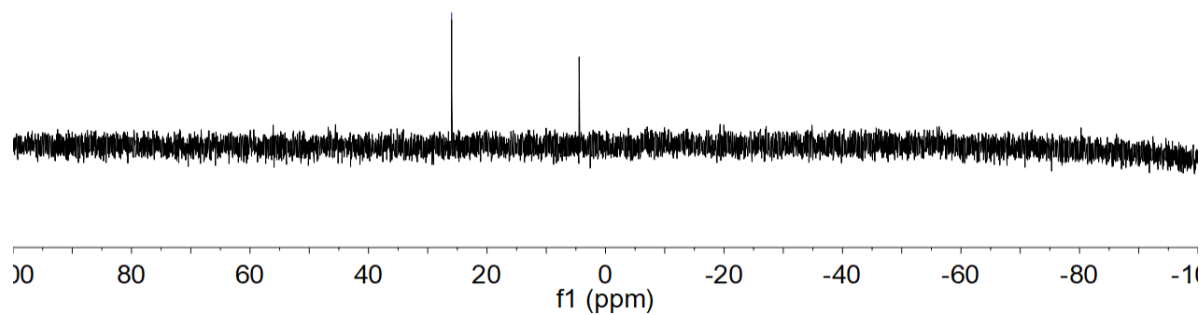
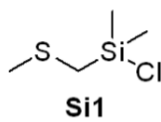


¹³C NMR (126 MHz, CDCl₃)



^{29}Si NMR (79 MHz, CDCl_3)

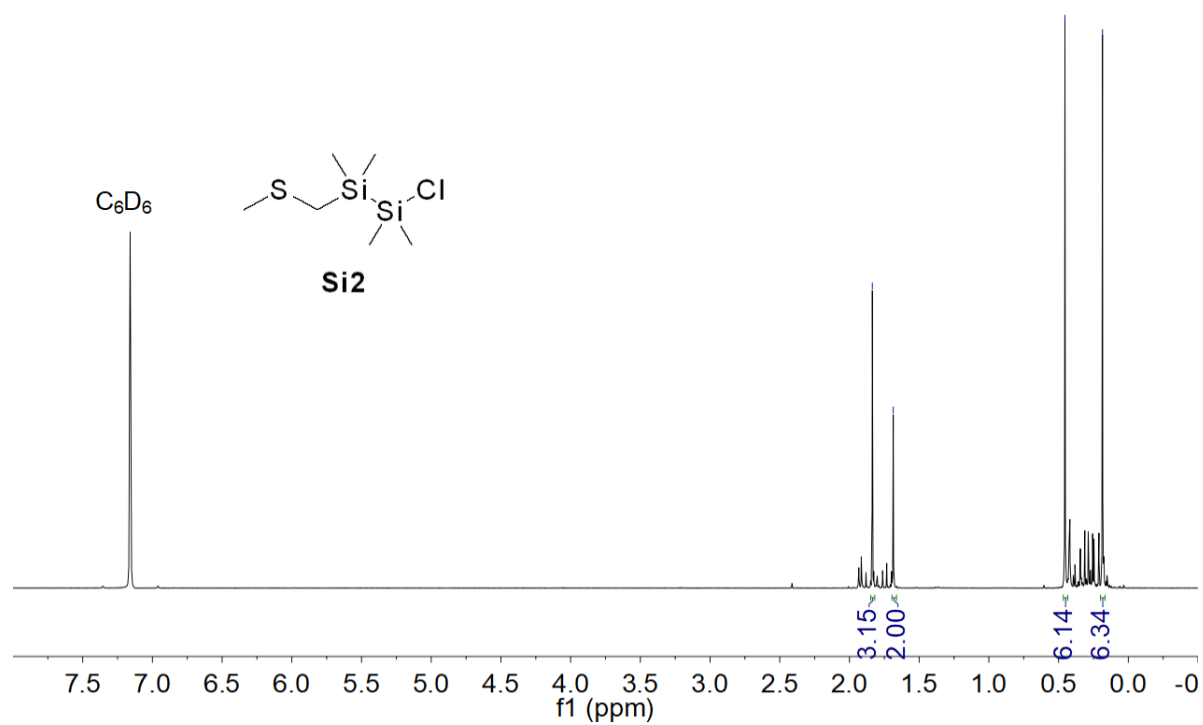
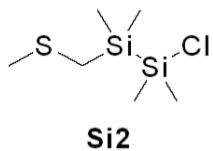
-25.96



^1H NMR (400 MHz, C_6D_6)

1.84
1.69
0.45
0.19

C_6D_6

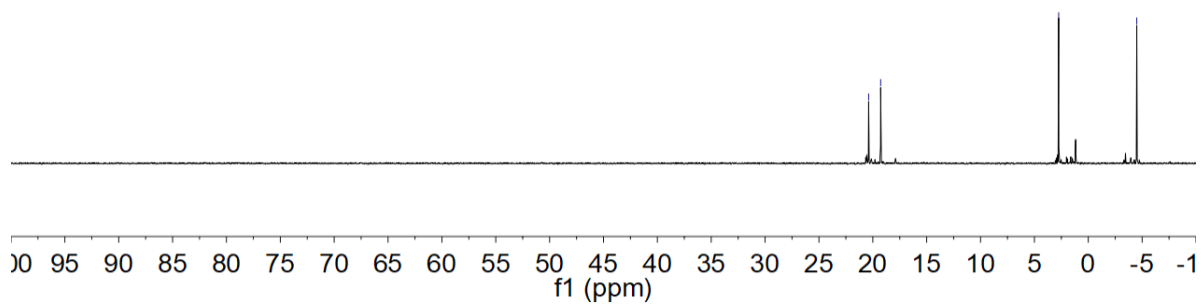
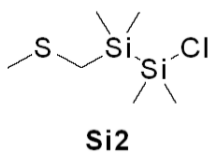


¹³C NMR (101 MHz, C₆D₆)

20.39
19.27

-2.75

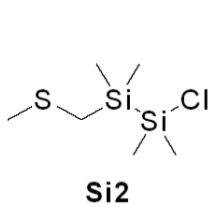
-4.50



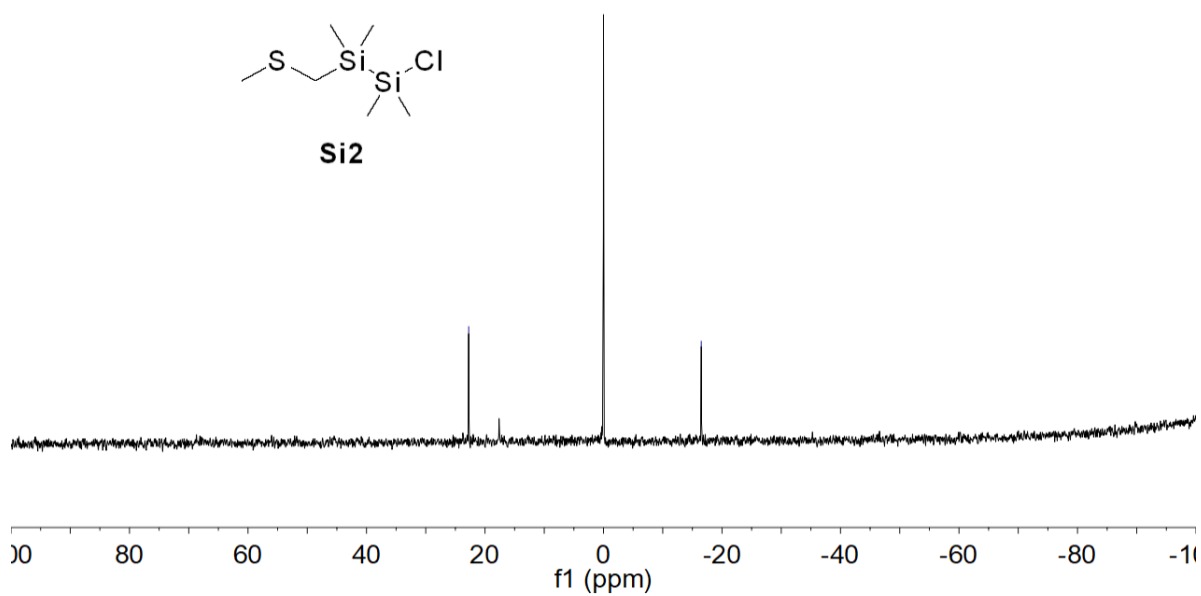
²⁹Si NMR (79 MHz, C₆D₆)

-22.75

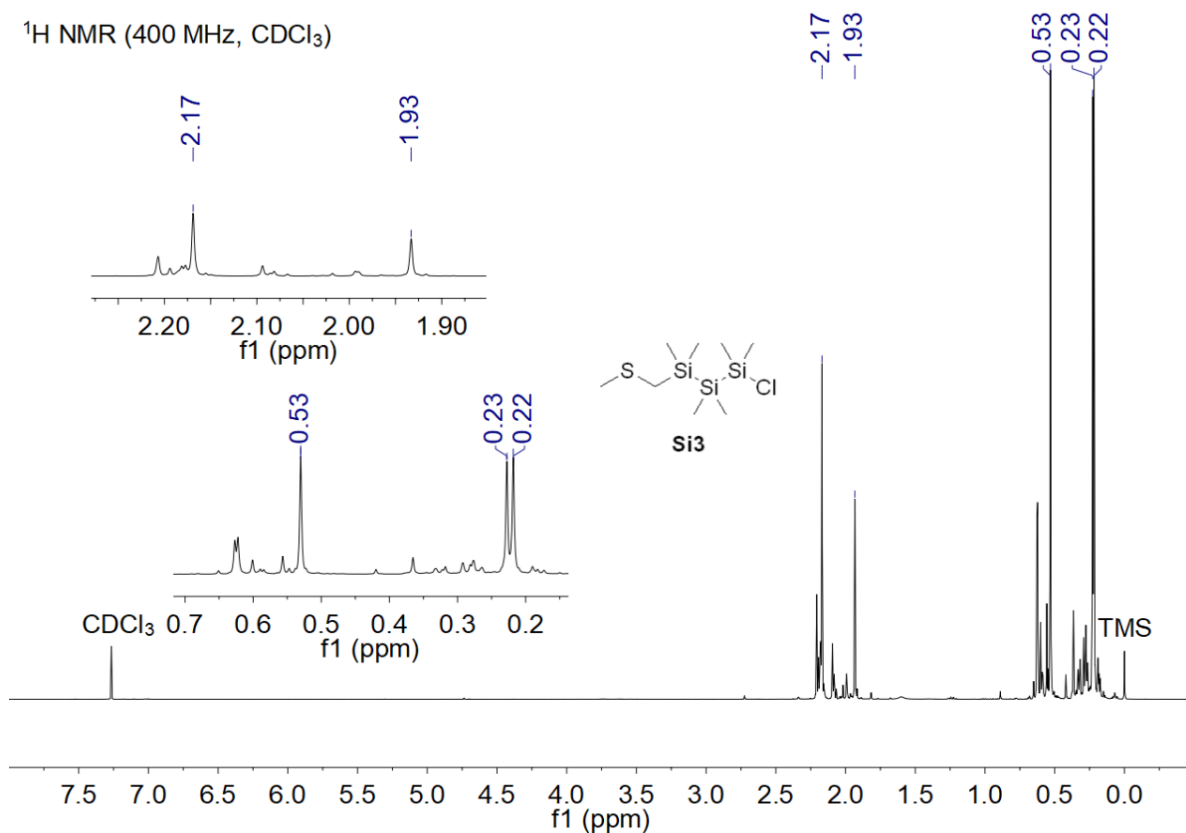
-16.50



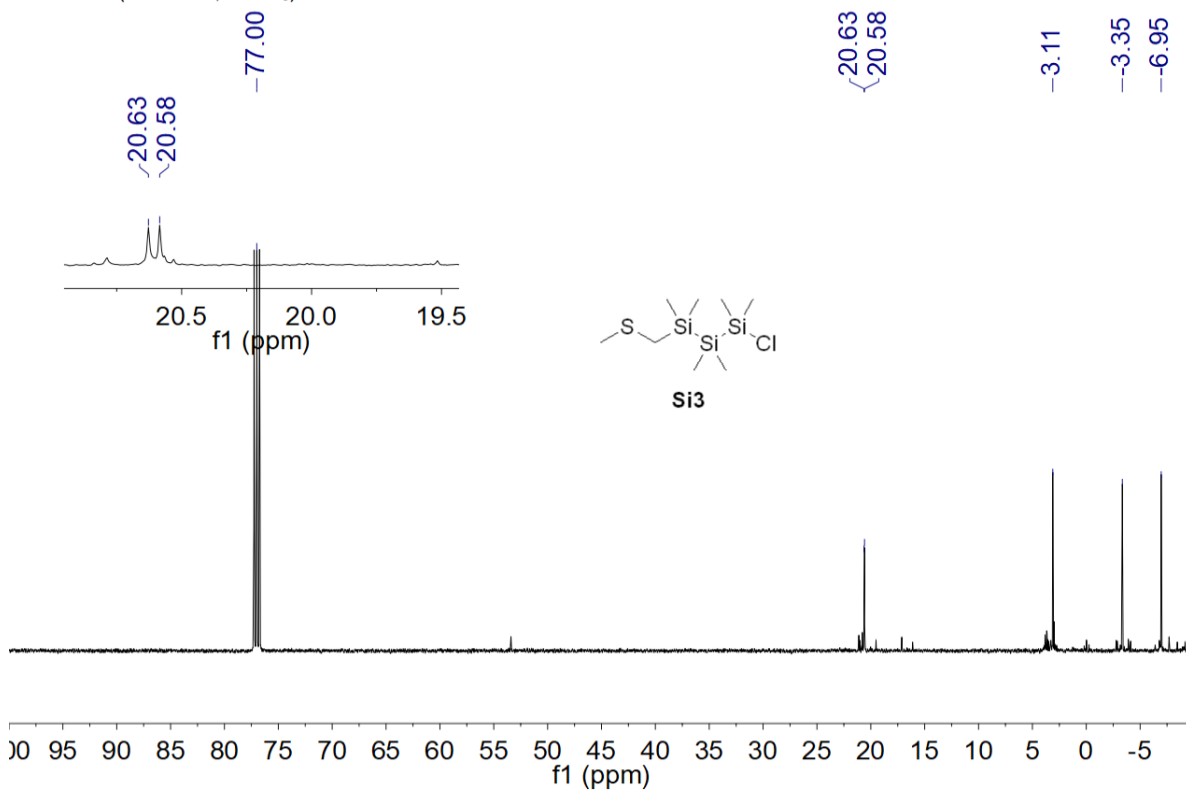
TMS



^1H NMR (400 MHz, CDCl_3)



^{13}C NMR (126 MHz, CDCl_3)

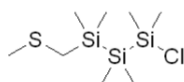


^{29}Si NMR (79 MHz, CDCl_3)

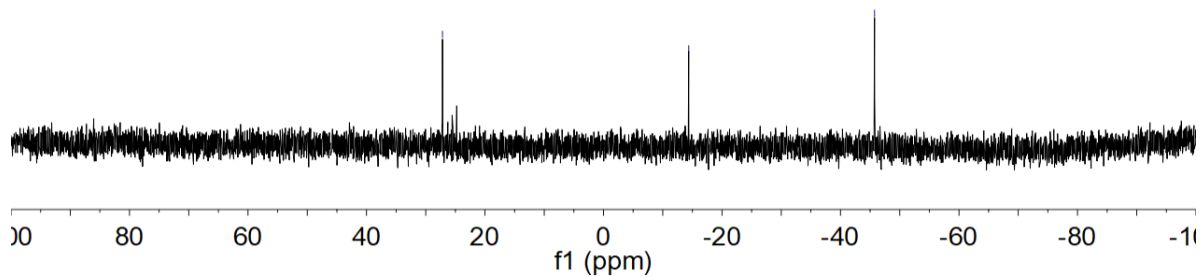
-27.17

-14.38

-45.75



Si3



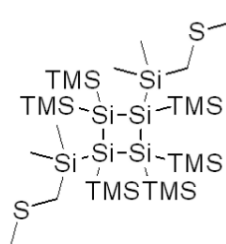
^1H NMR (400 MHz, CDCl_3)

2.17

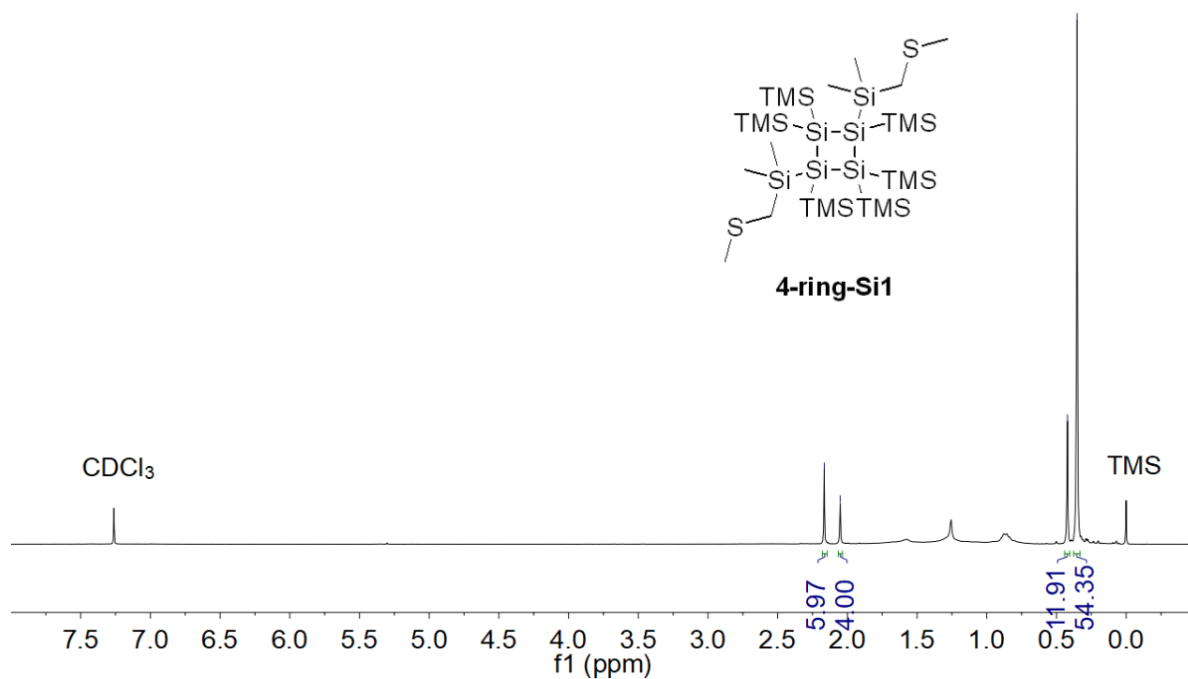
2.05

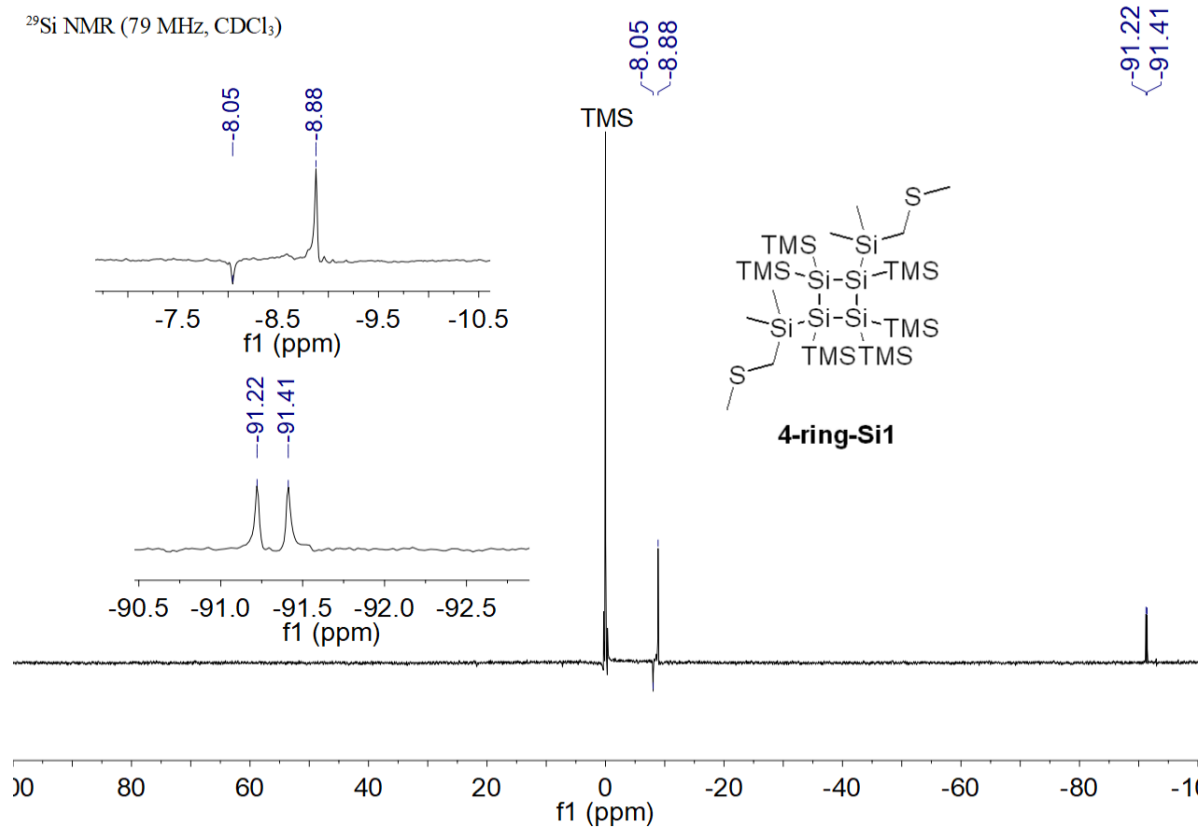
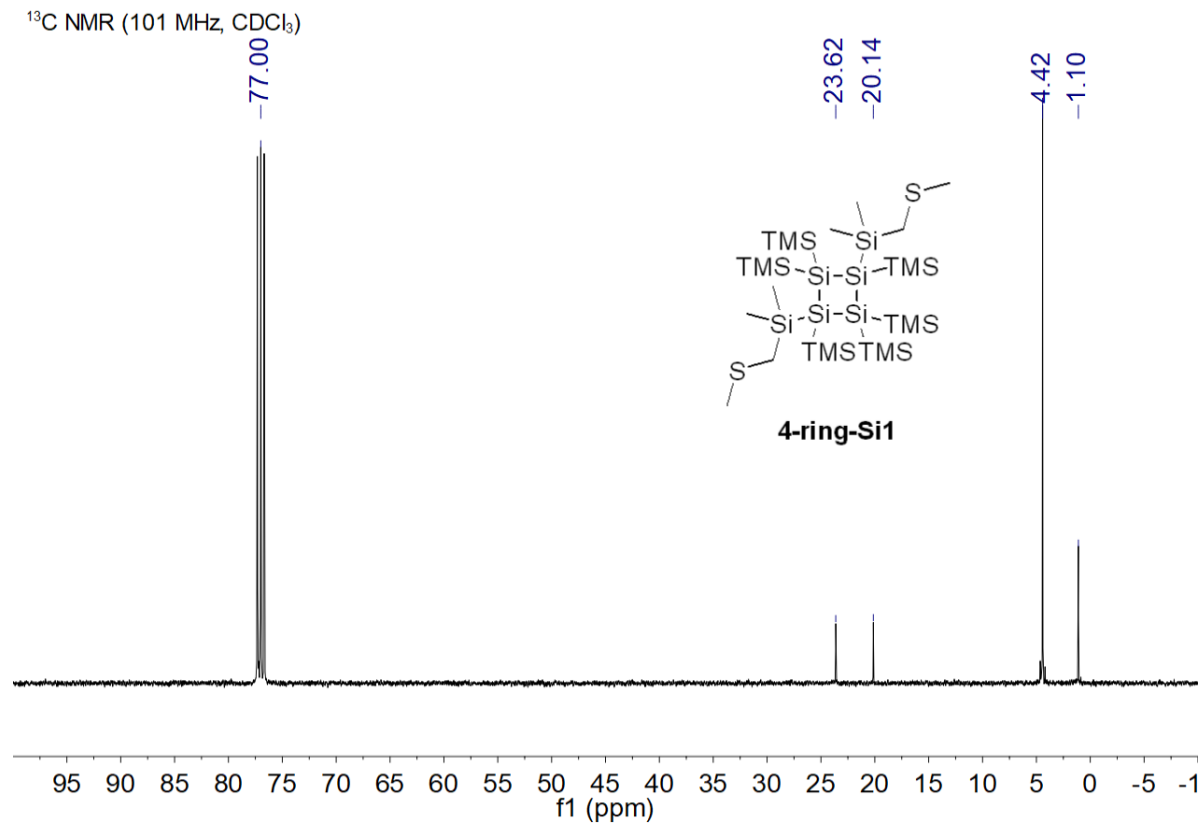
0.42

0.35

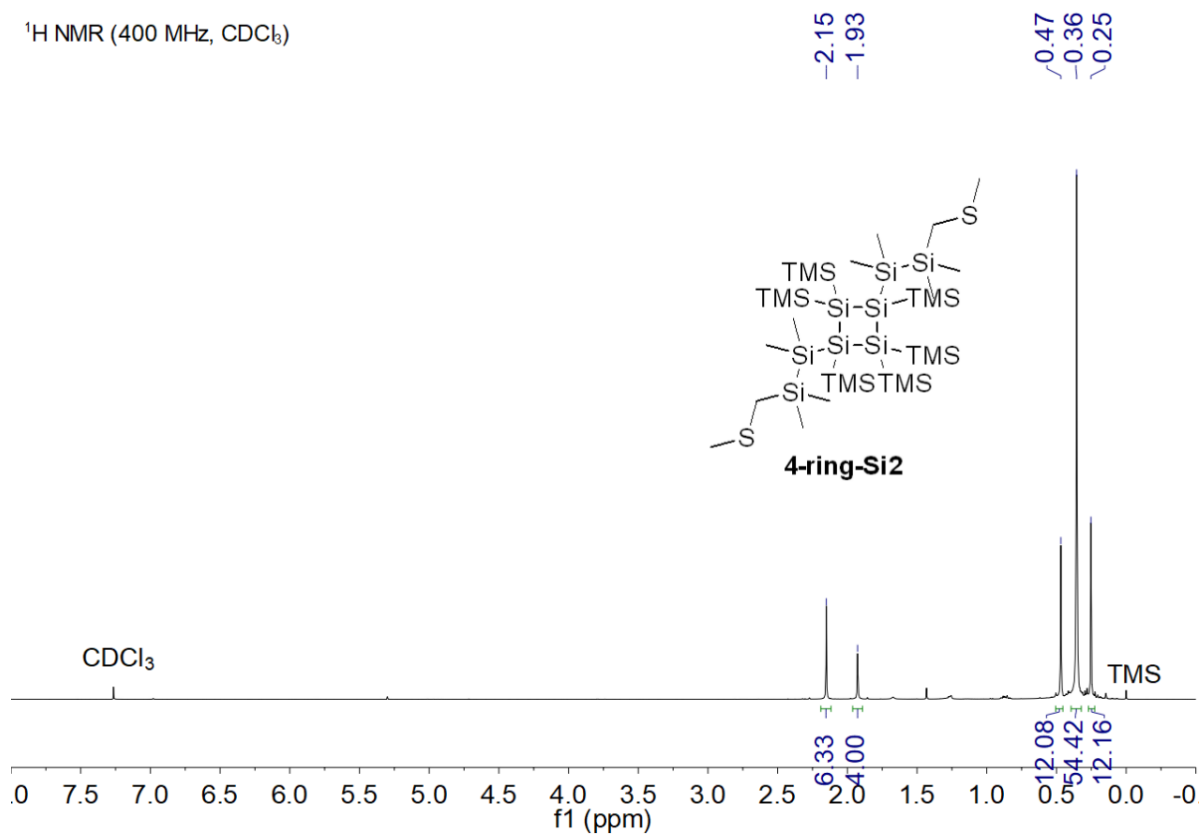


4-ring-Si1

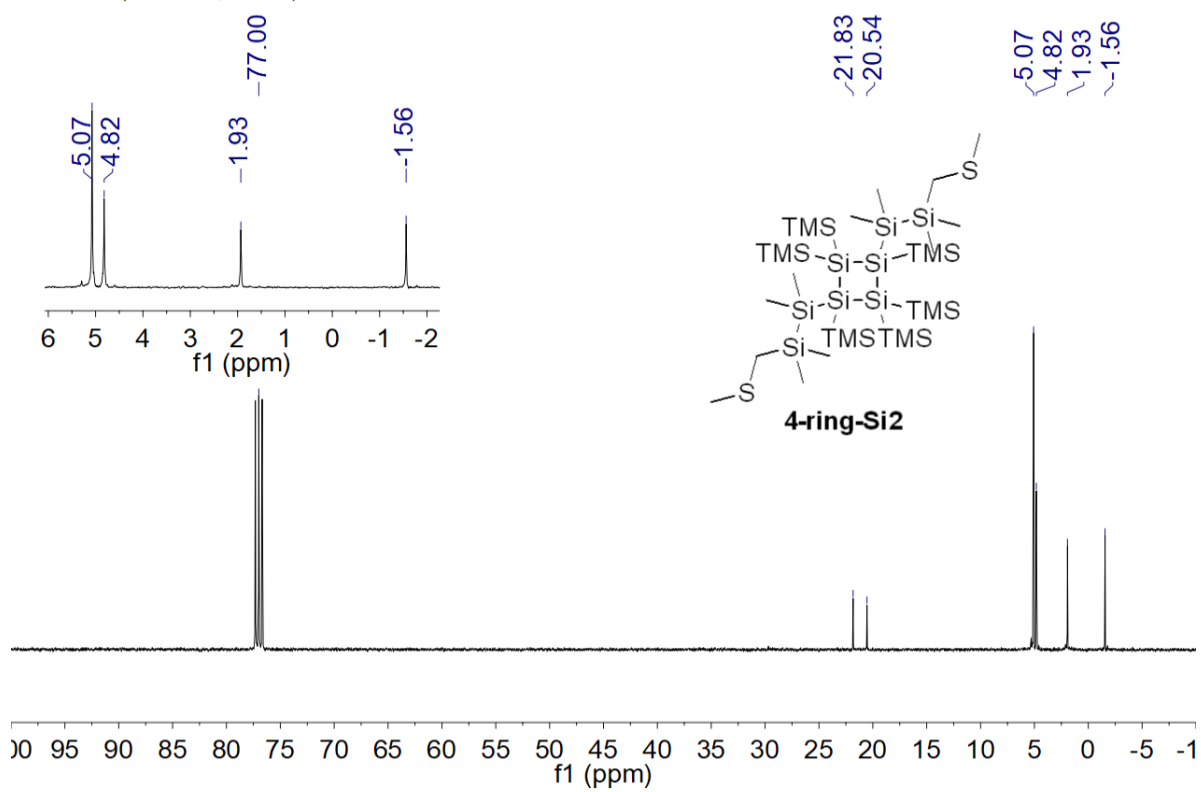




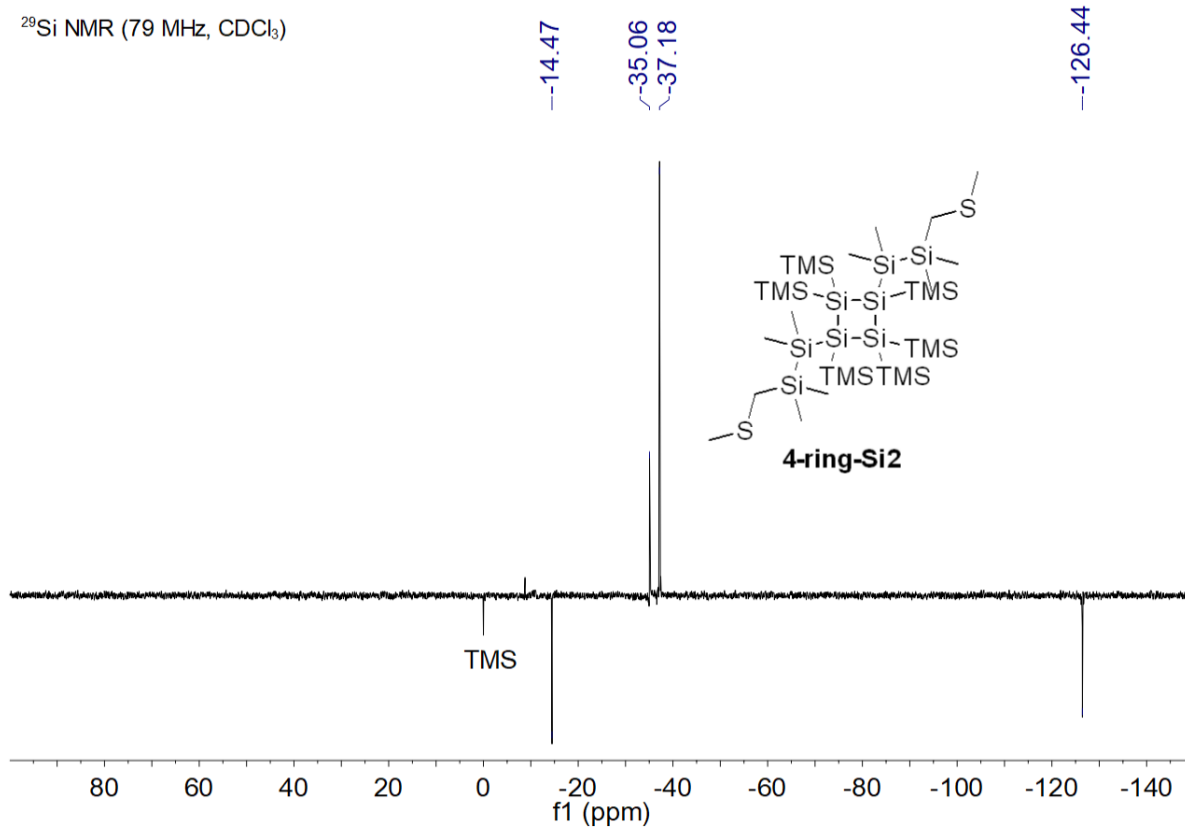
¹H NMR (400 MHz, CDCl₃)



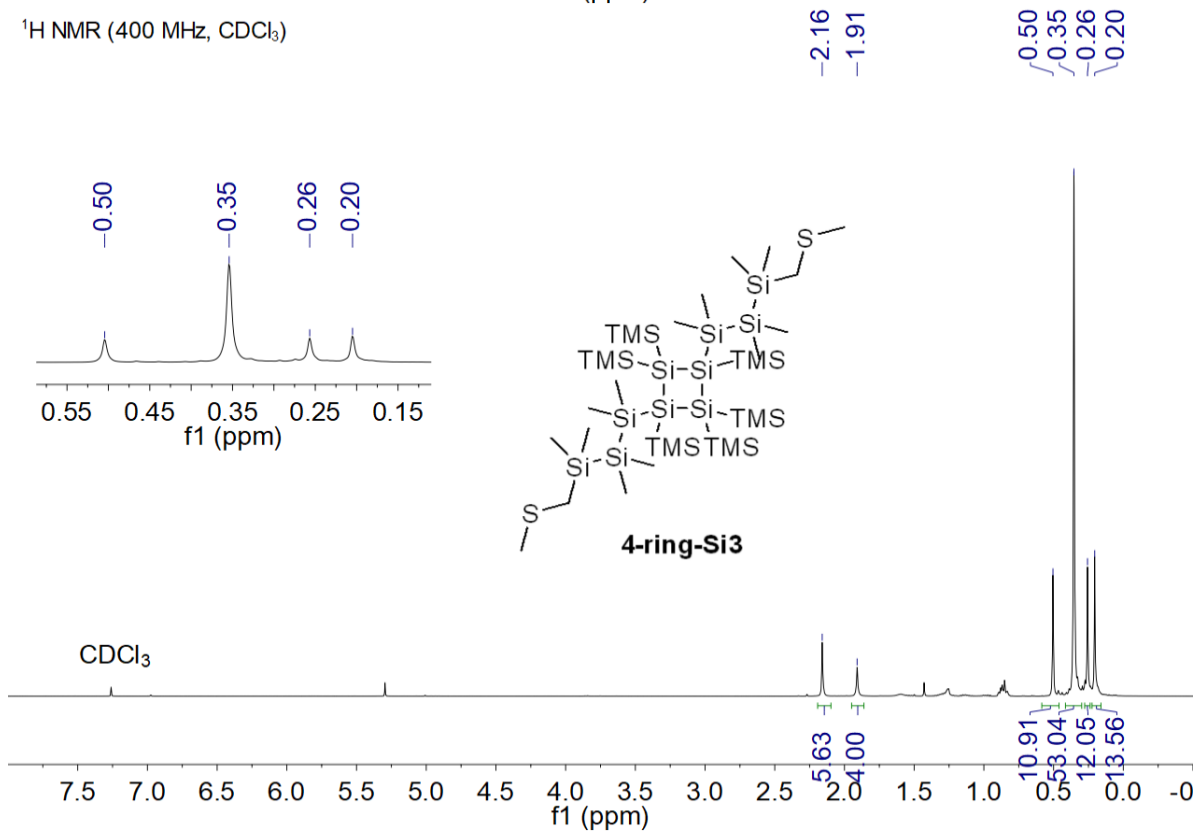
¹³C NMR (101 MHz, CDCl₃)

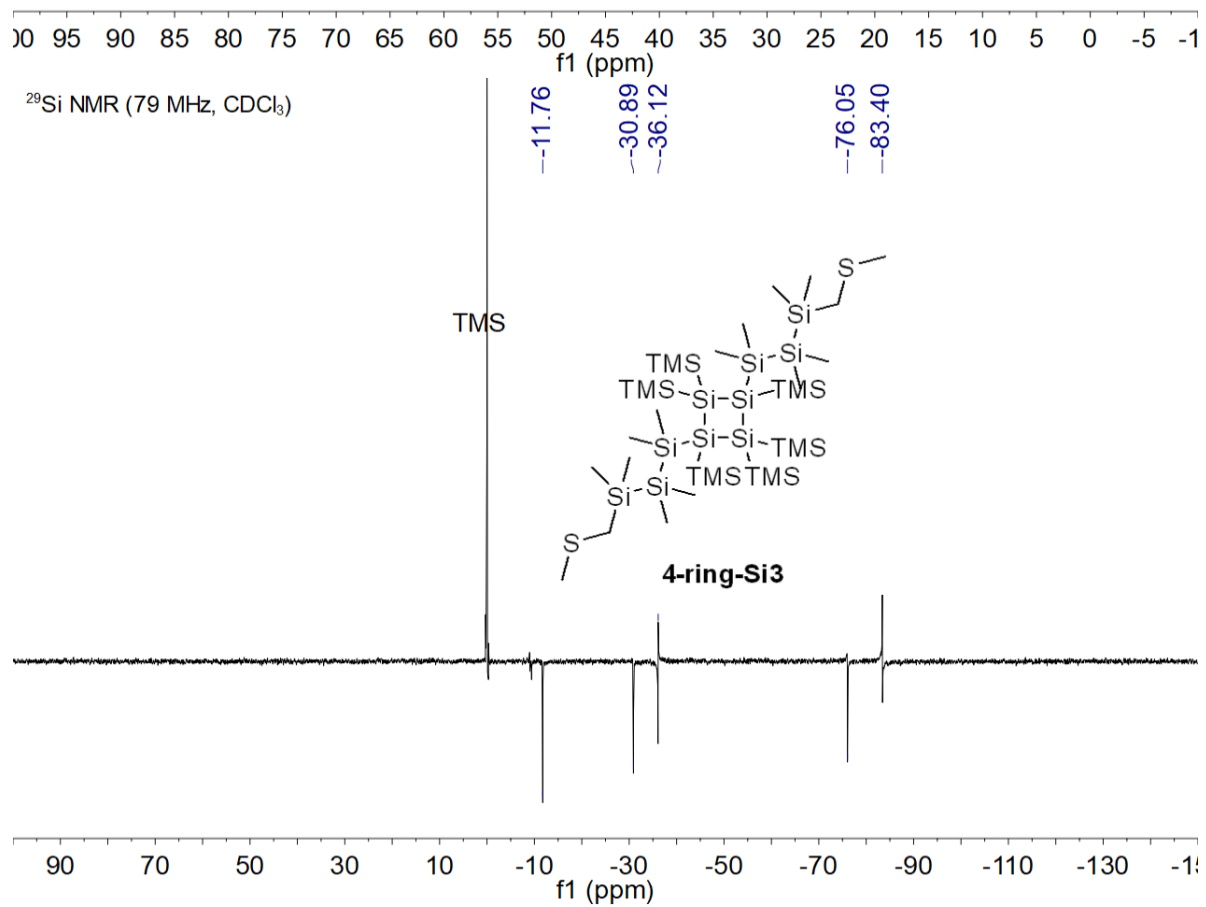
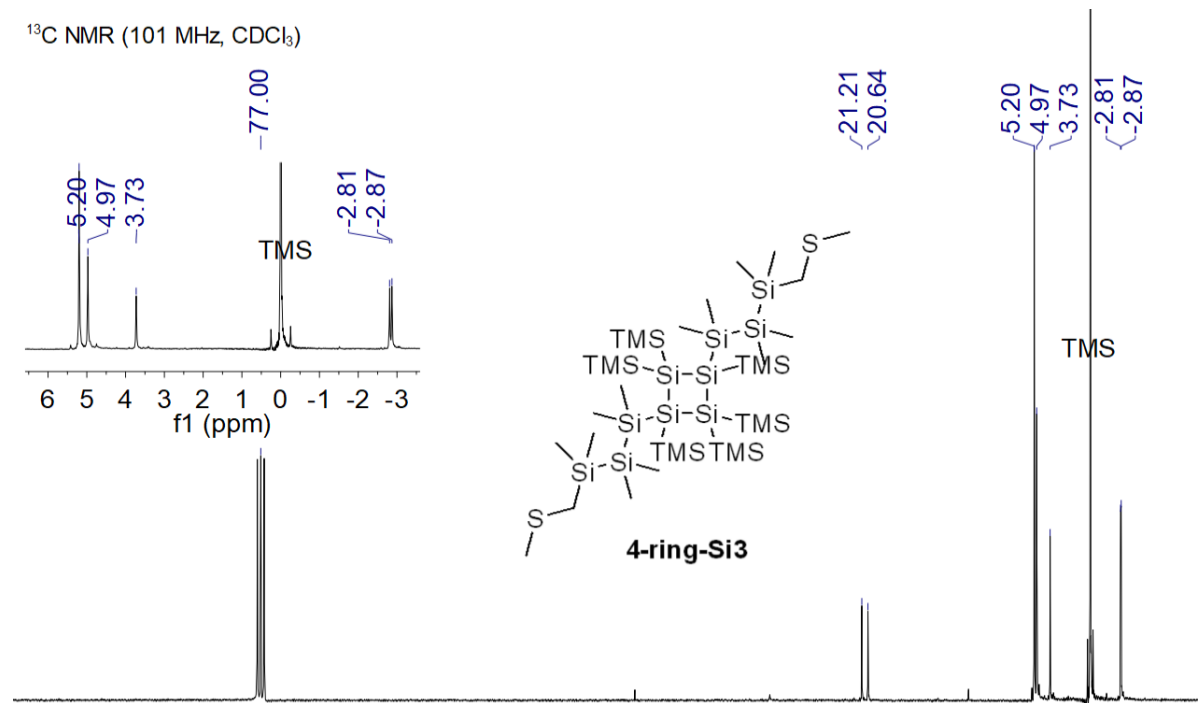


^{29}Si NMR (79 MHz, CDCl_3)

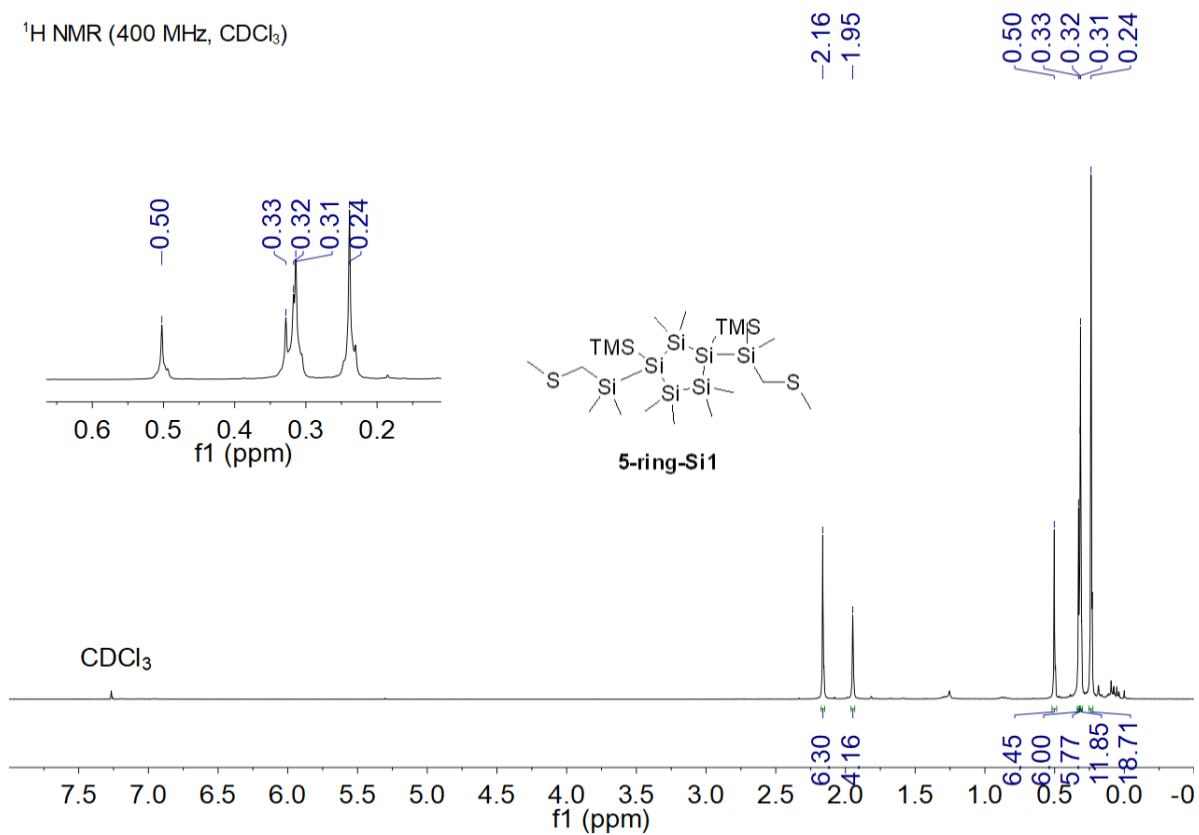


^1H NMR (400 MHz, CDCl_3)

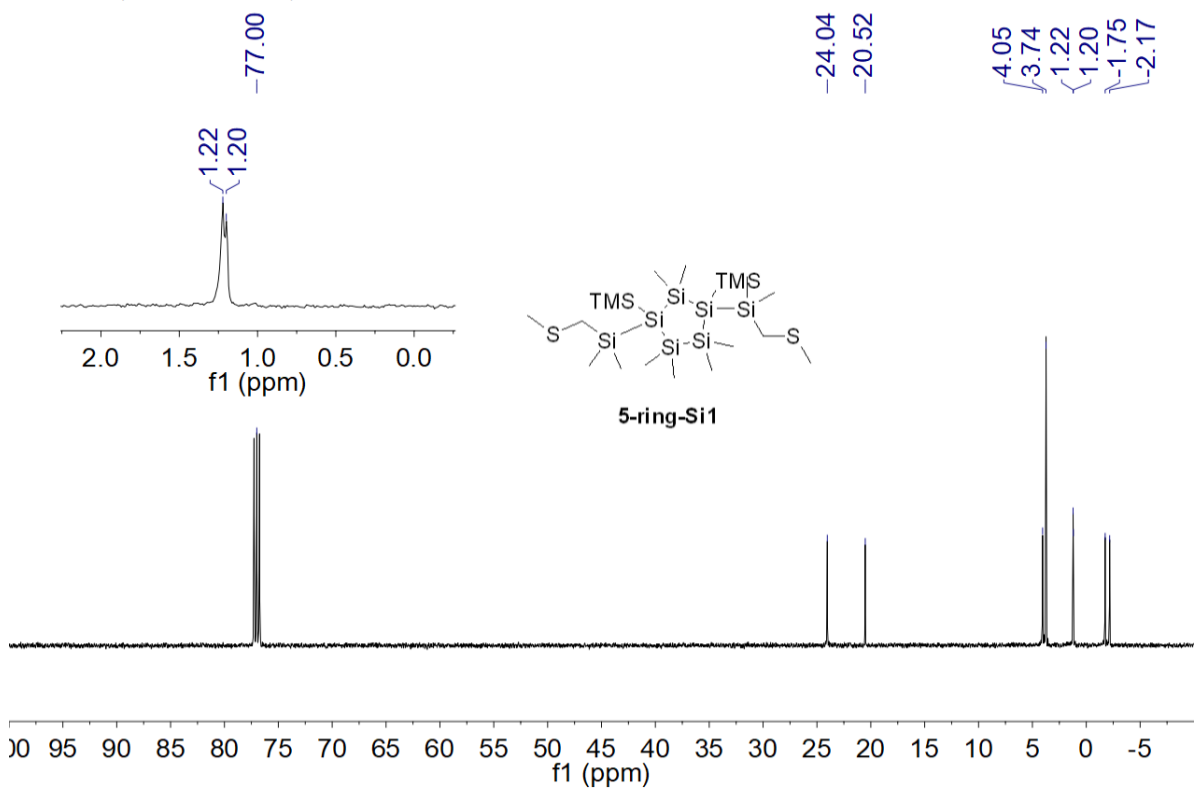




¹H NMR (400 MHz, CDCl₃)



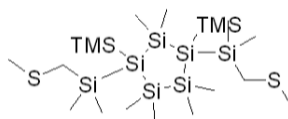
¹³C NMR (126 MHz, CDCl₃)



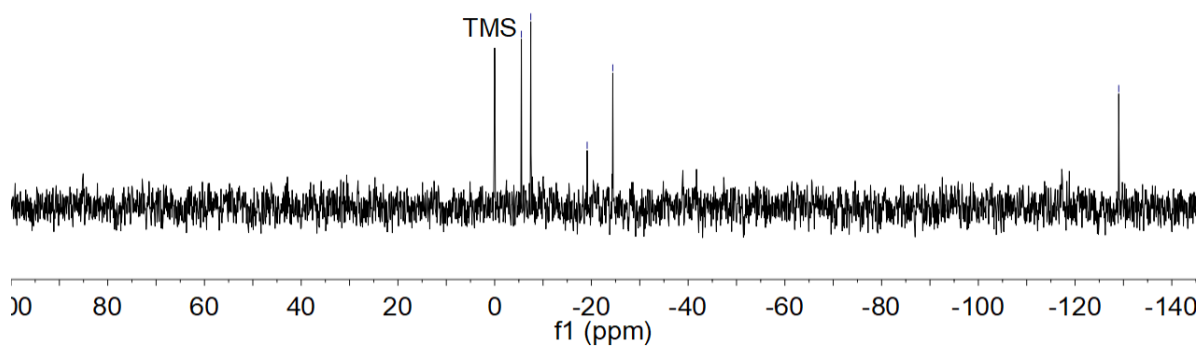
^{29}Si NMR (60 MHz, CDCl_3)

-5.52
-7.47
-19.12
-24.42

-129.02

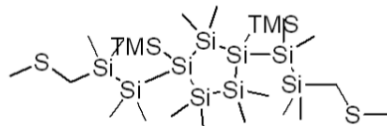


5-ring-Si1

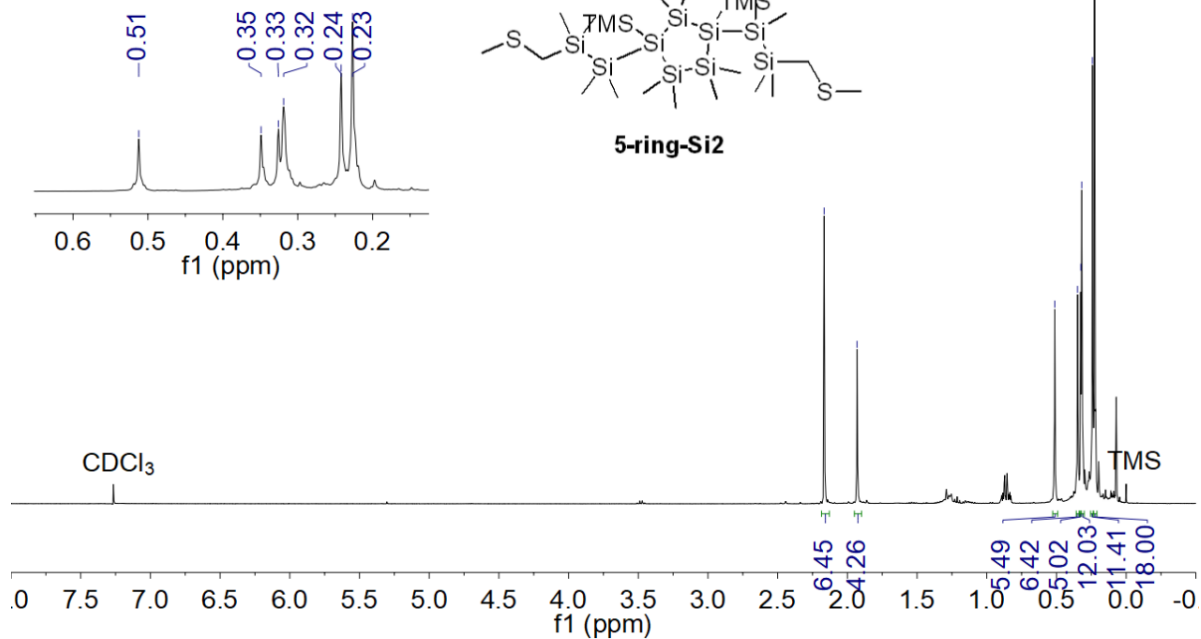


^1H NMR (400 MHz, CDCl_3)

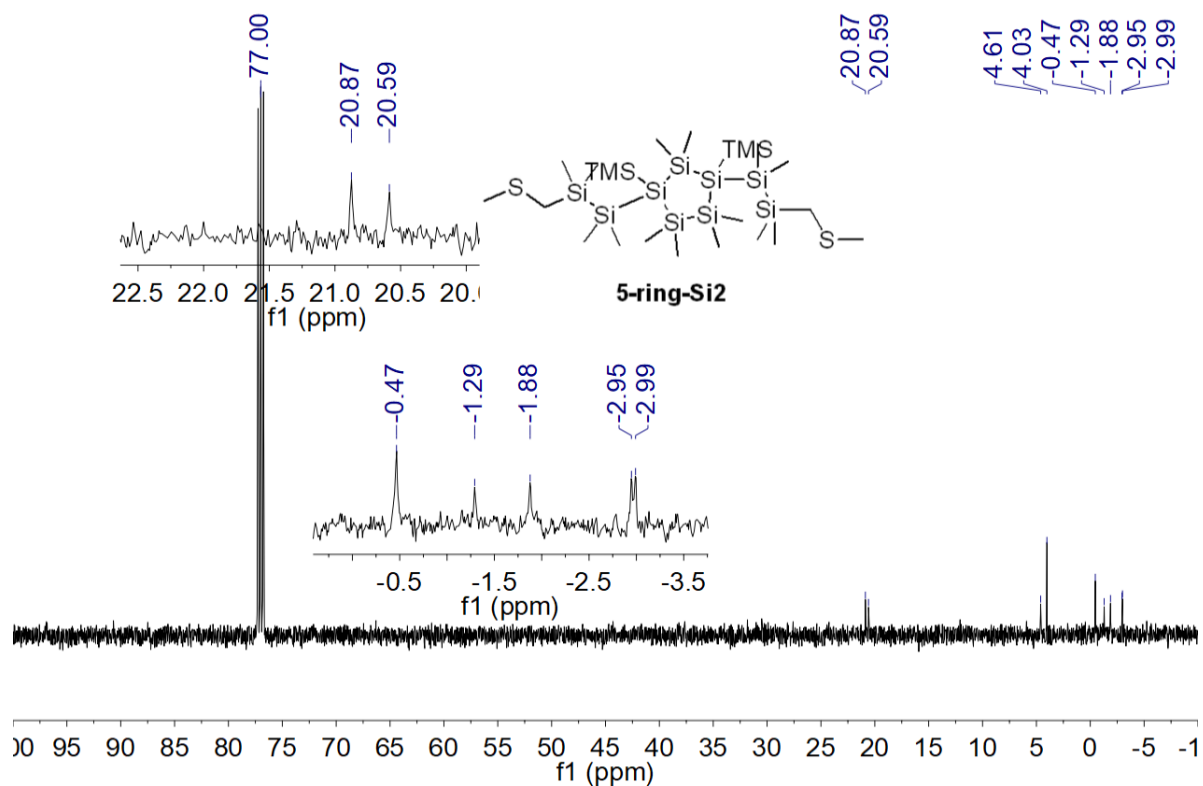
-2.17
-1.93
0.51
0.35
0.33
0.32
0.24
0.23



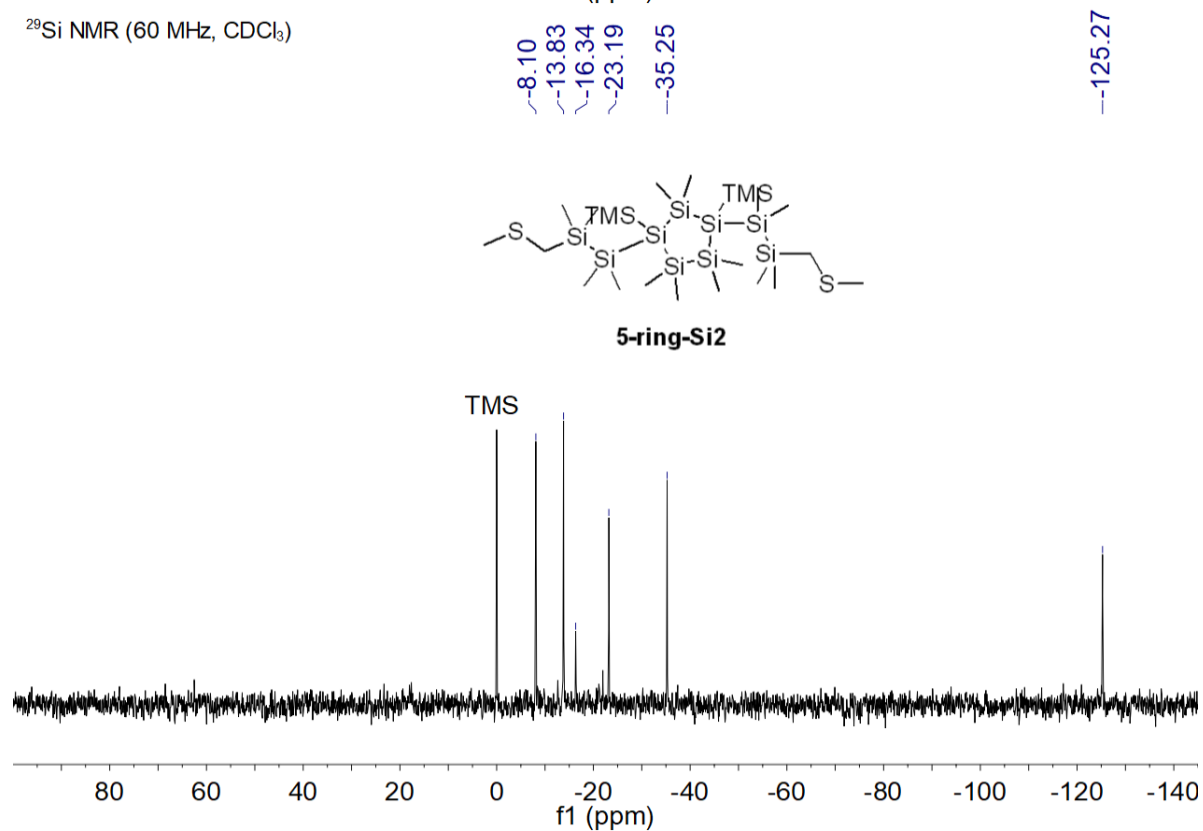
5-ring-Si2



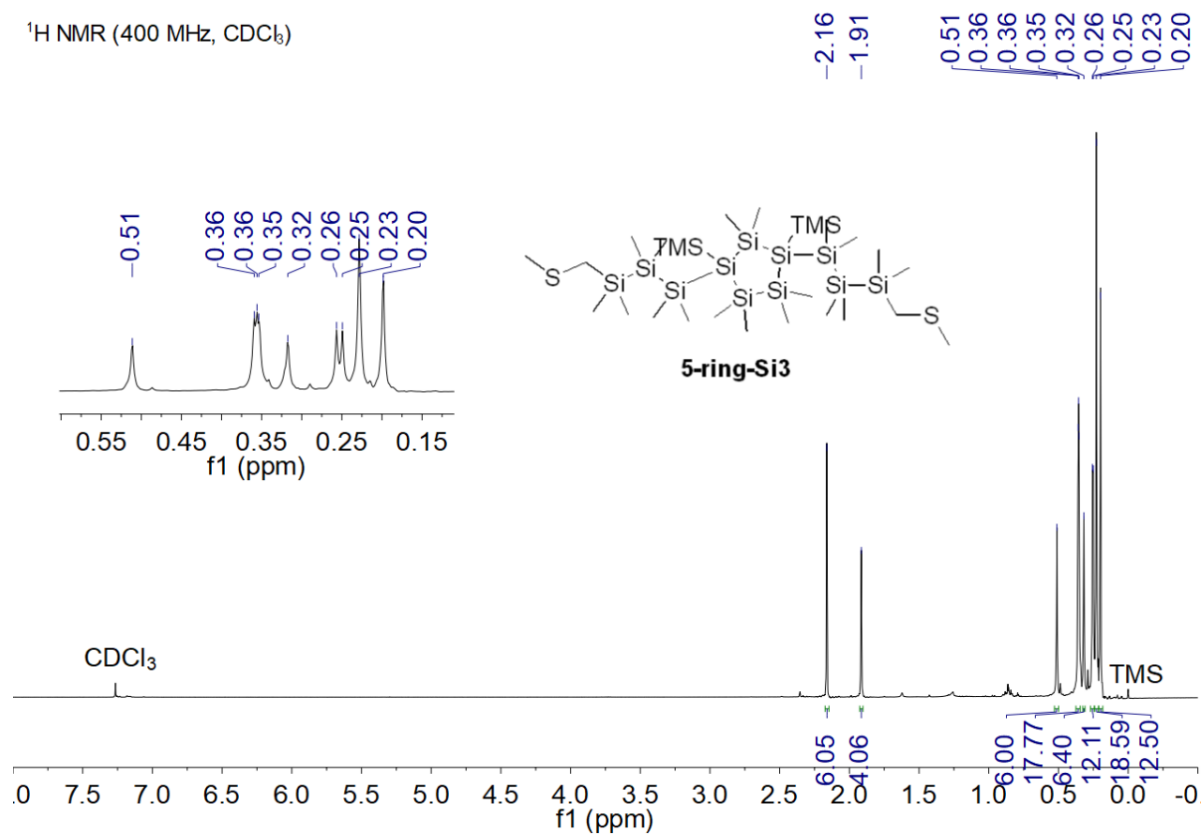
¹³C NMR (126 MHz, CDCl₃)



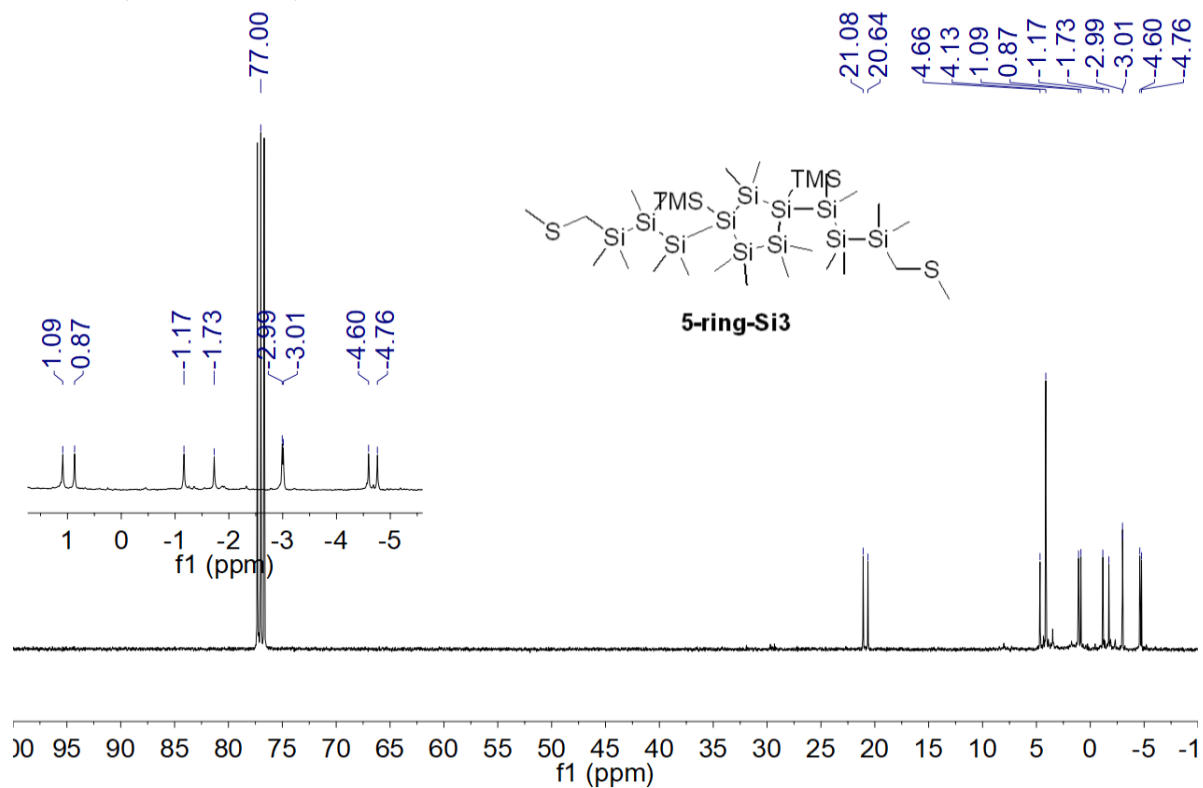
²⁹Si NMR (60 MHz, CDCl₃)



¹H NMR (400 MHz, CDCl₃)



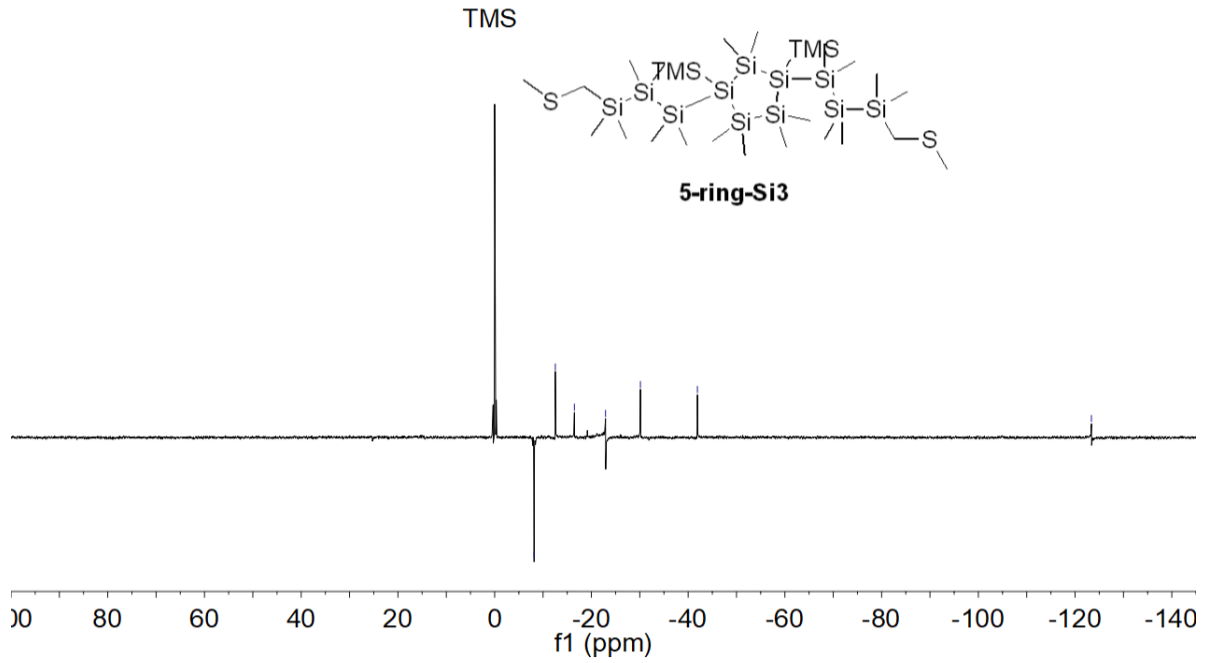
¹³C NMR (101 MHz, CDCl₃)



^{29}Si NMR (79 MHz, CDCl_3)

-8.16
-12.54
-16.48
-22.92
-30.13
-41.91

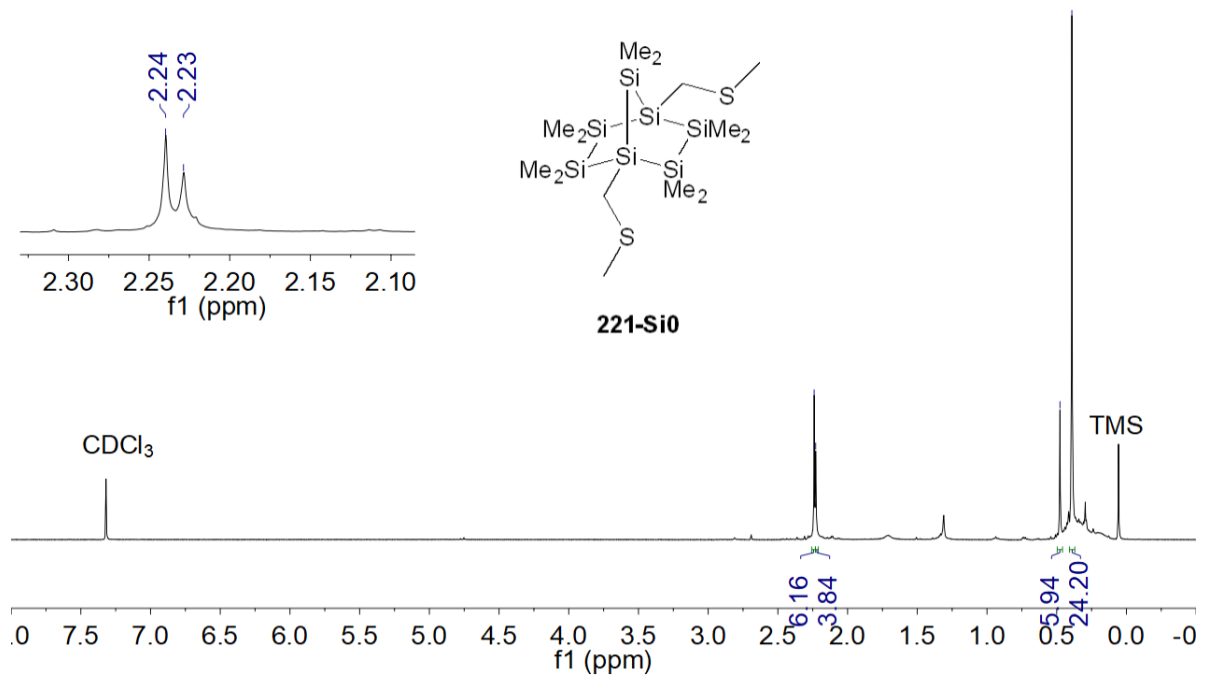
-123.38



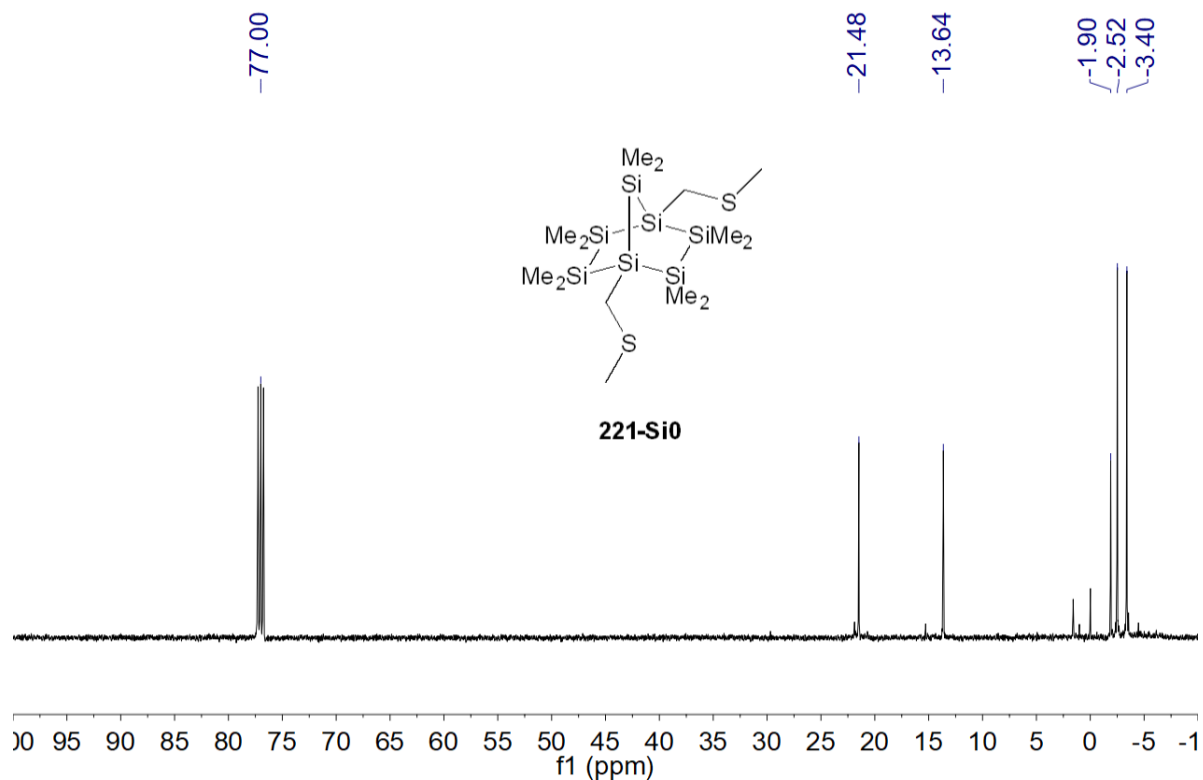
^1H NMR (400 MHz, CDCl_3)

2.24
2.23

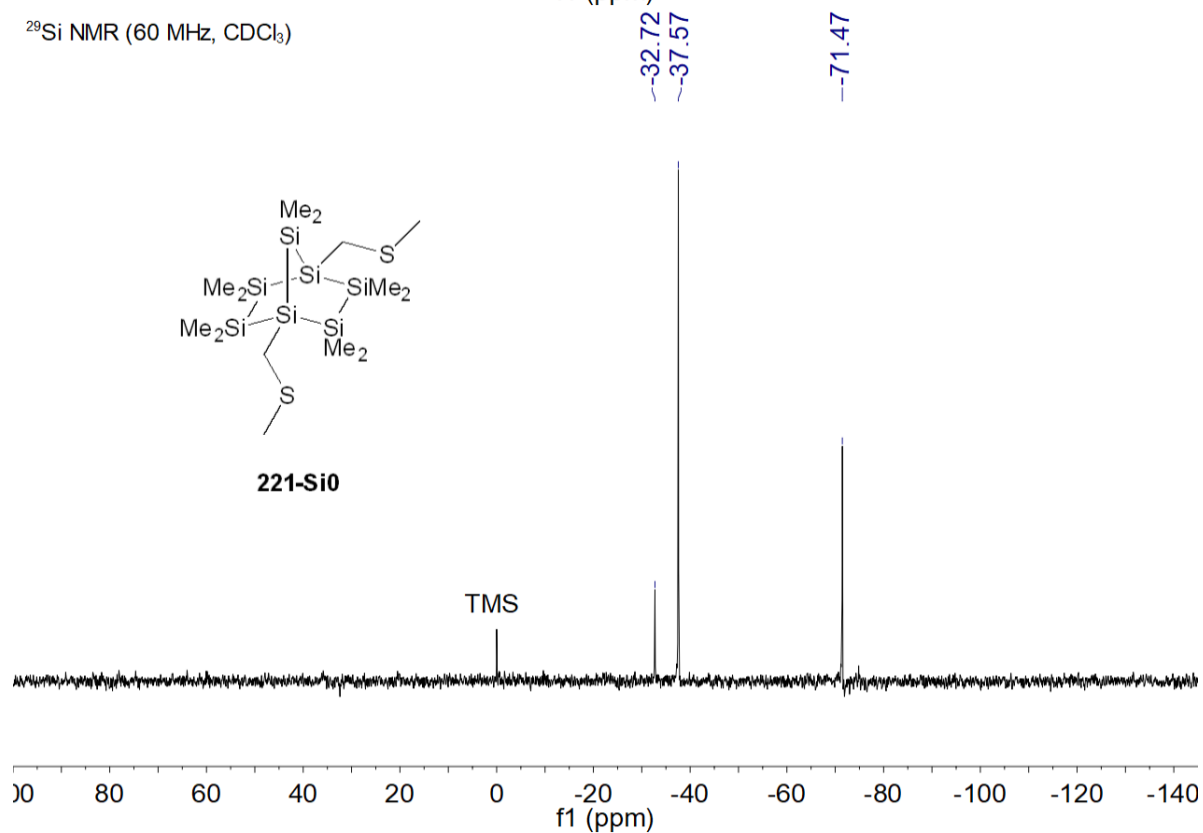
0.48
0.39



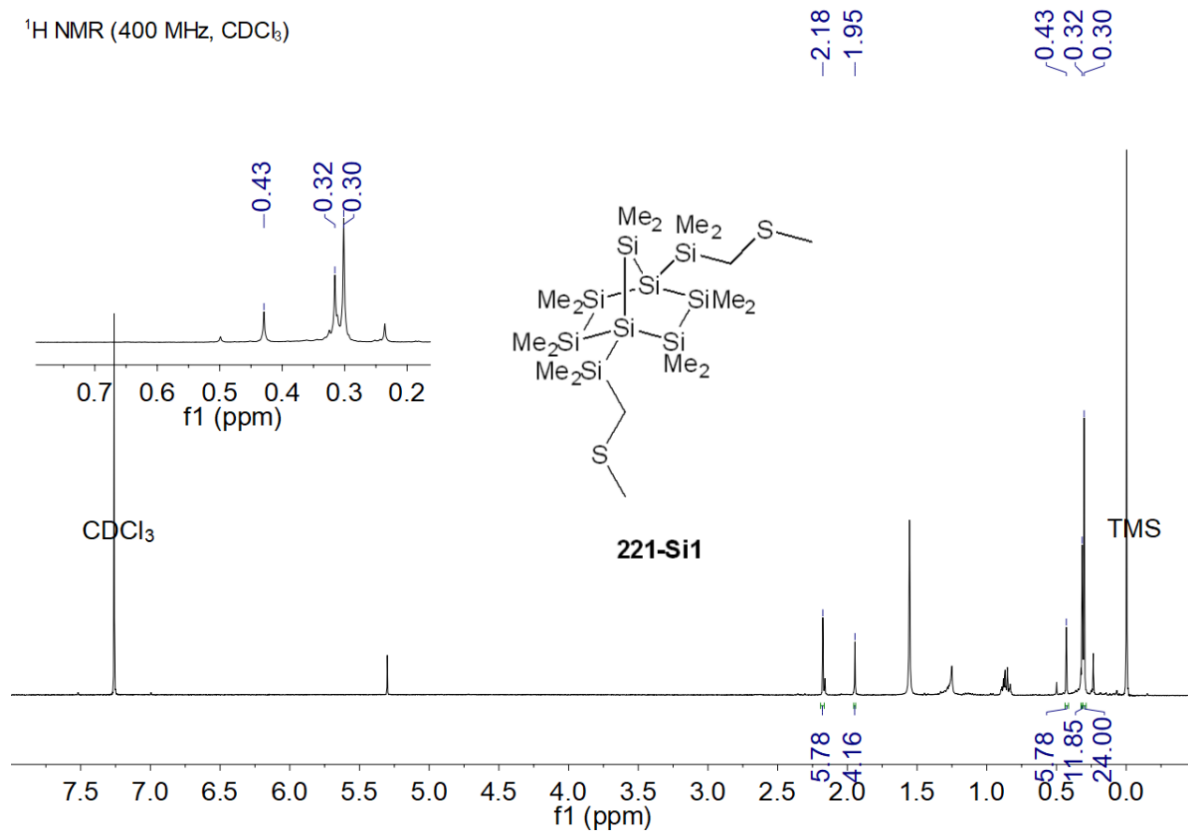
¹³C NMR (126 MHz, CDCl₃)



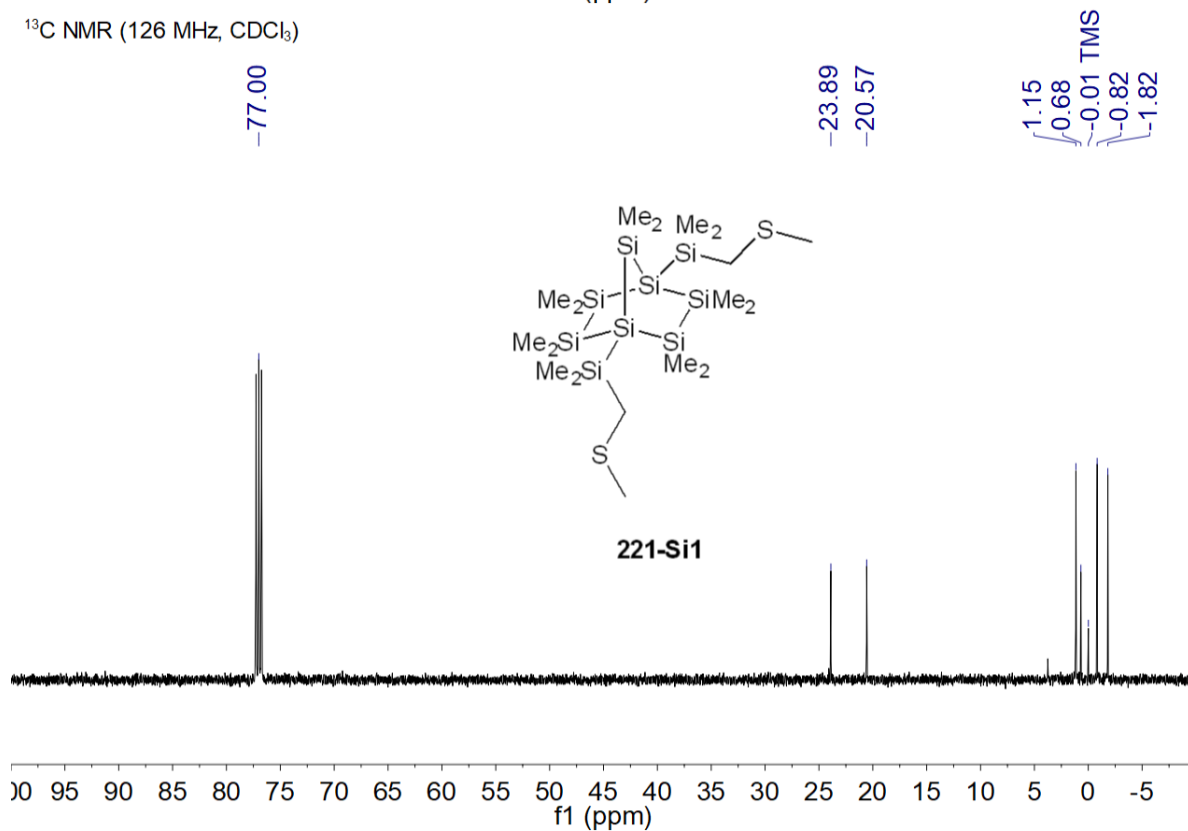
²⁹Si NMR (60 MHz, CDCl₃)

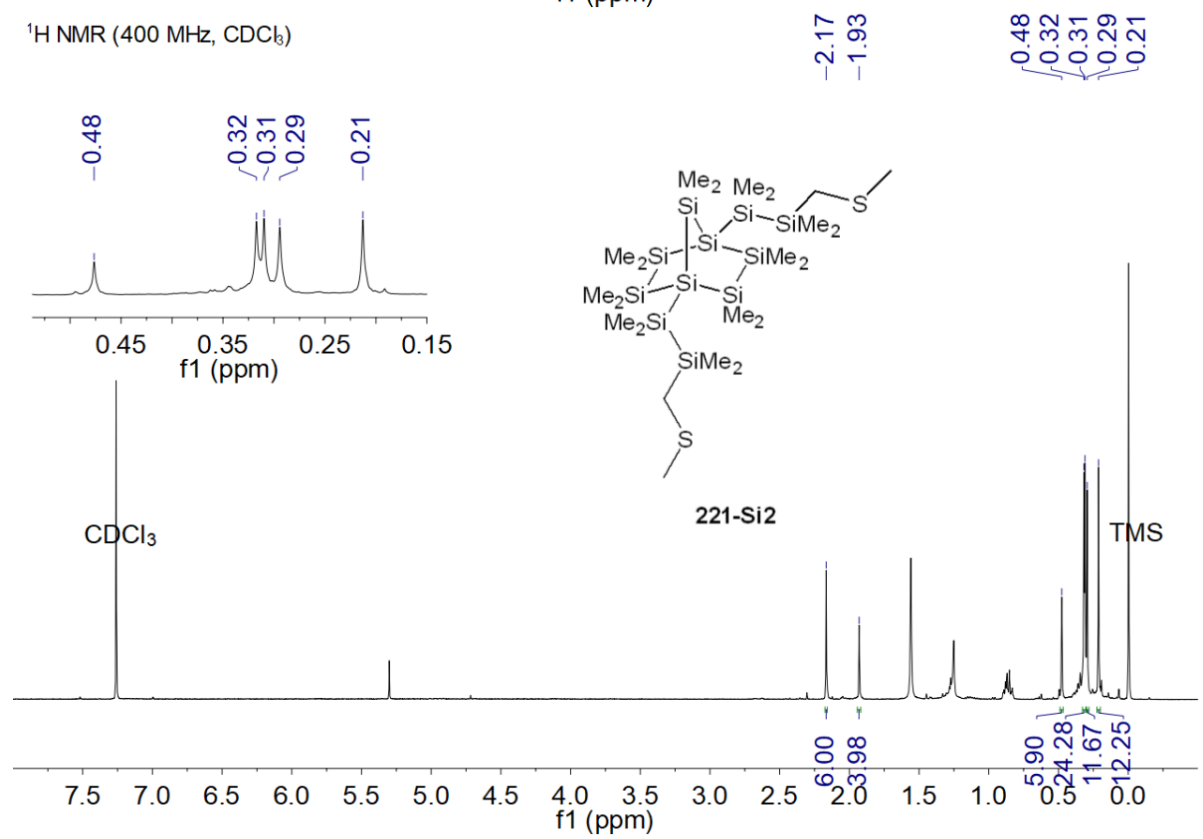
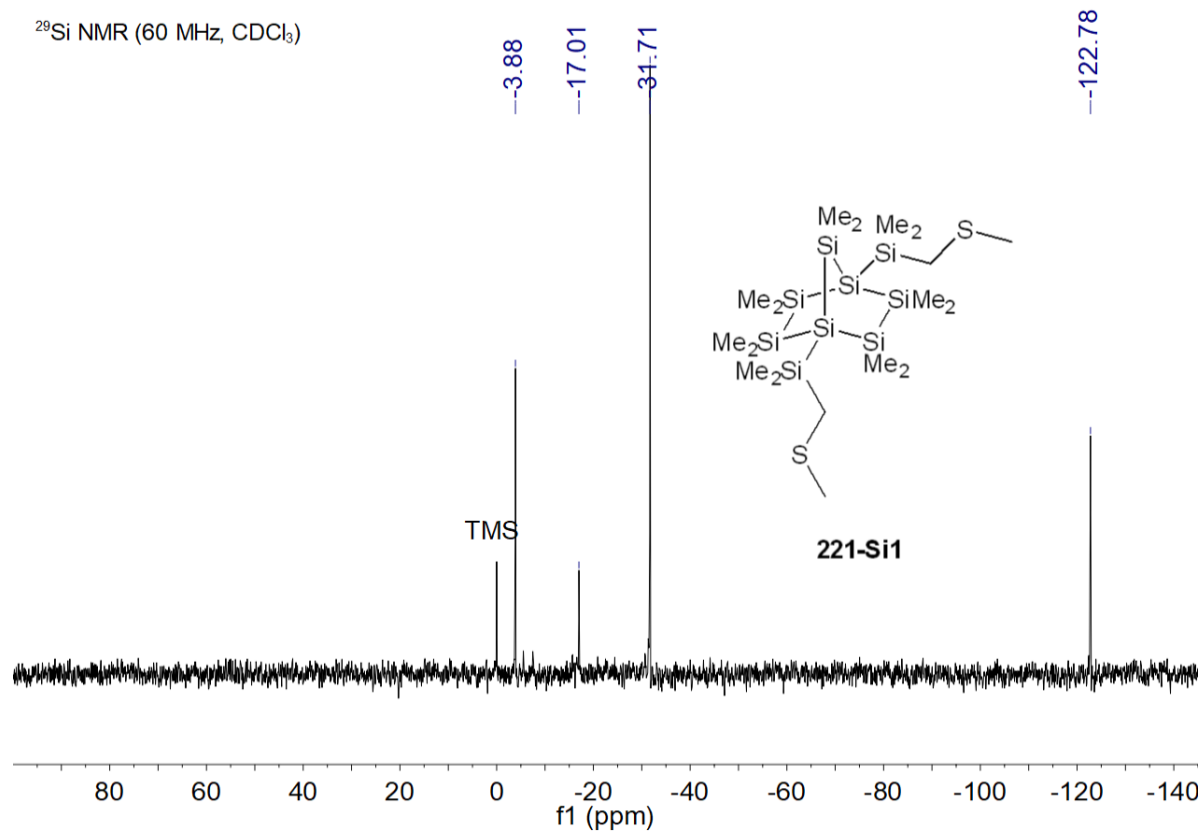


¹H NMR (400 MHz, CDCl₃)

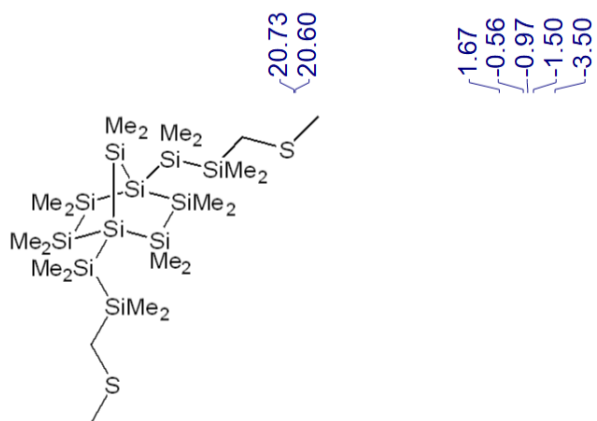
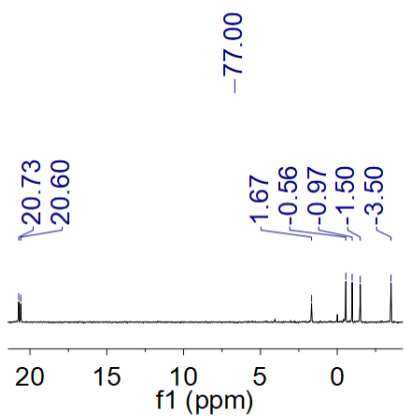


¹³C NMR (126 MHz, CDCl₃)

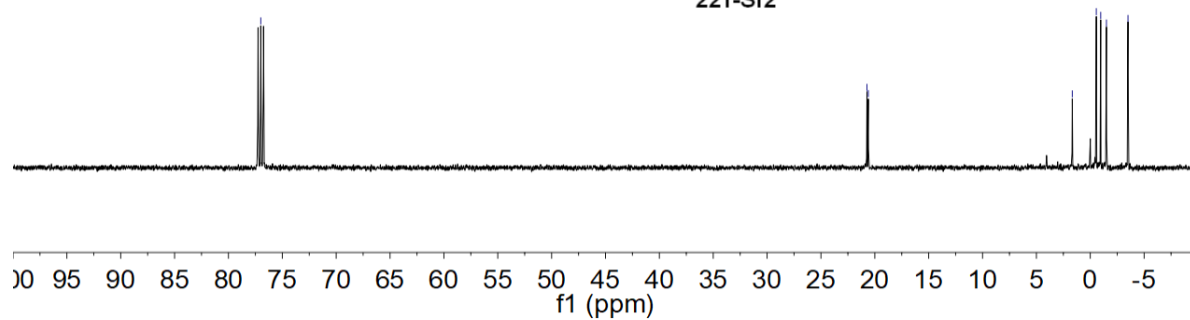




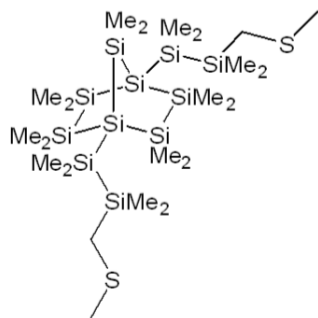
¹³C NMR (126 MHz, CDCl₃)



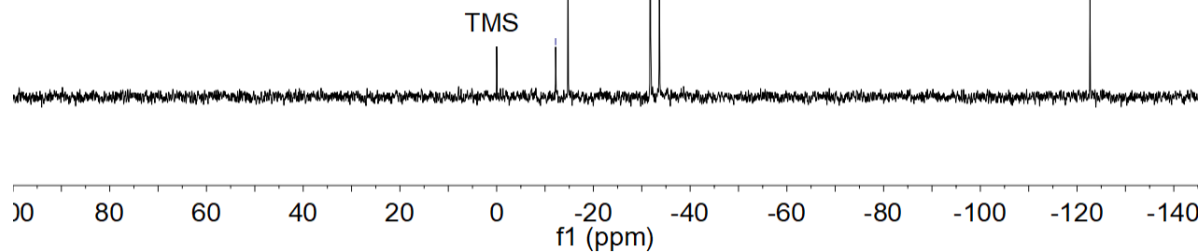
221-Si2



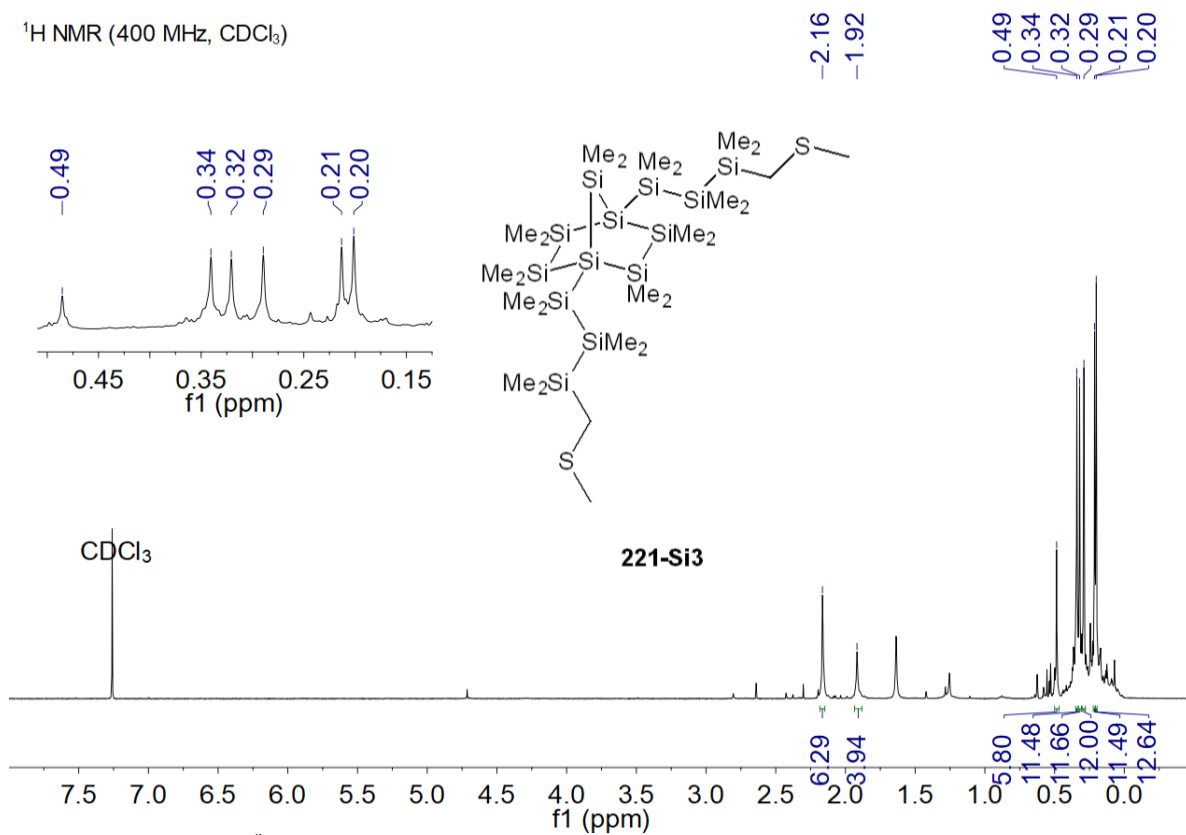
²⁹Si NMR (60 MHz, CDCl₃)



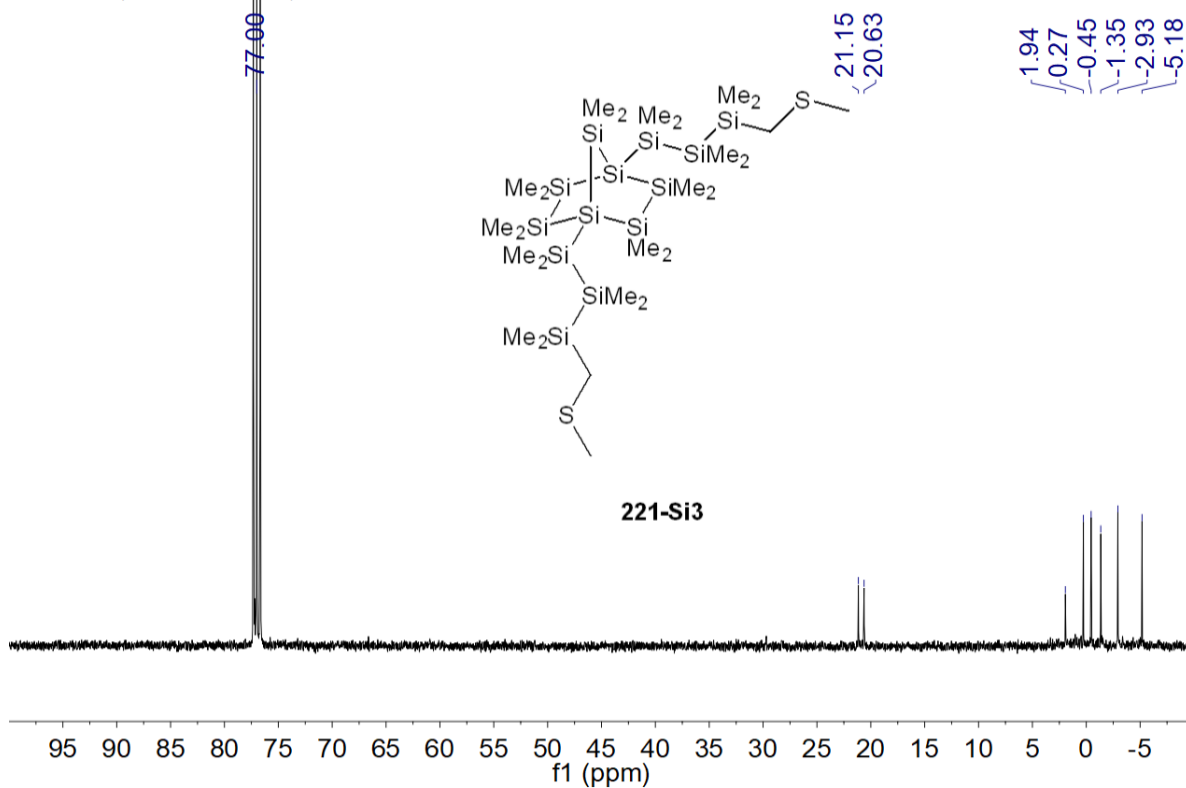
221-Si2

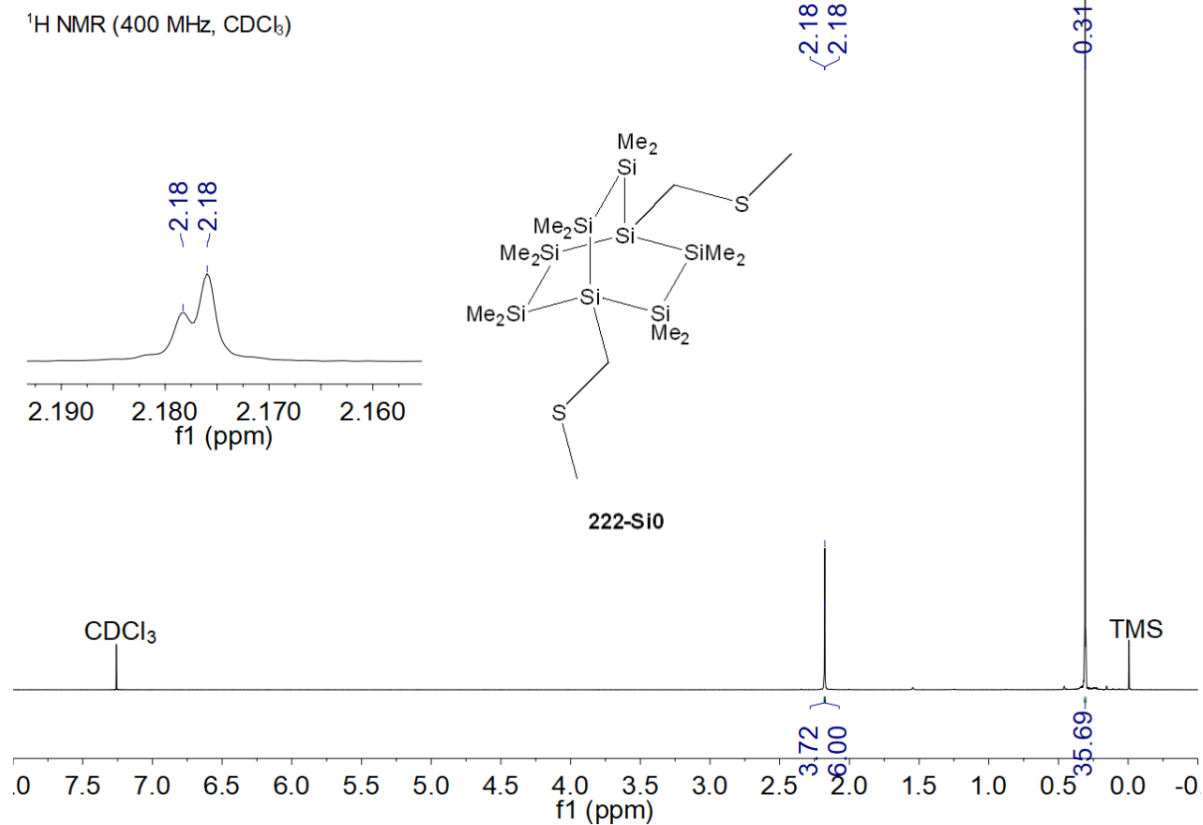
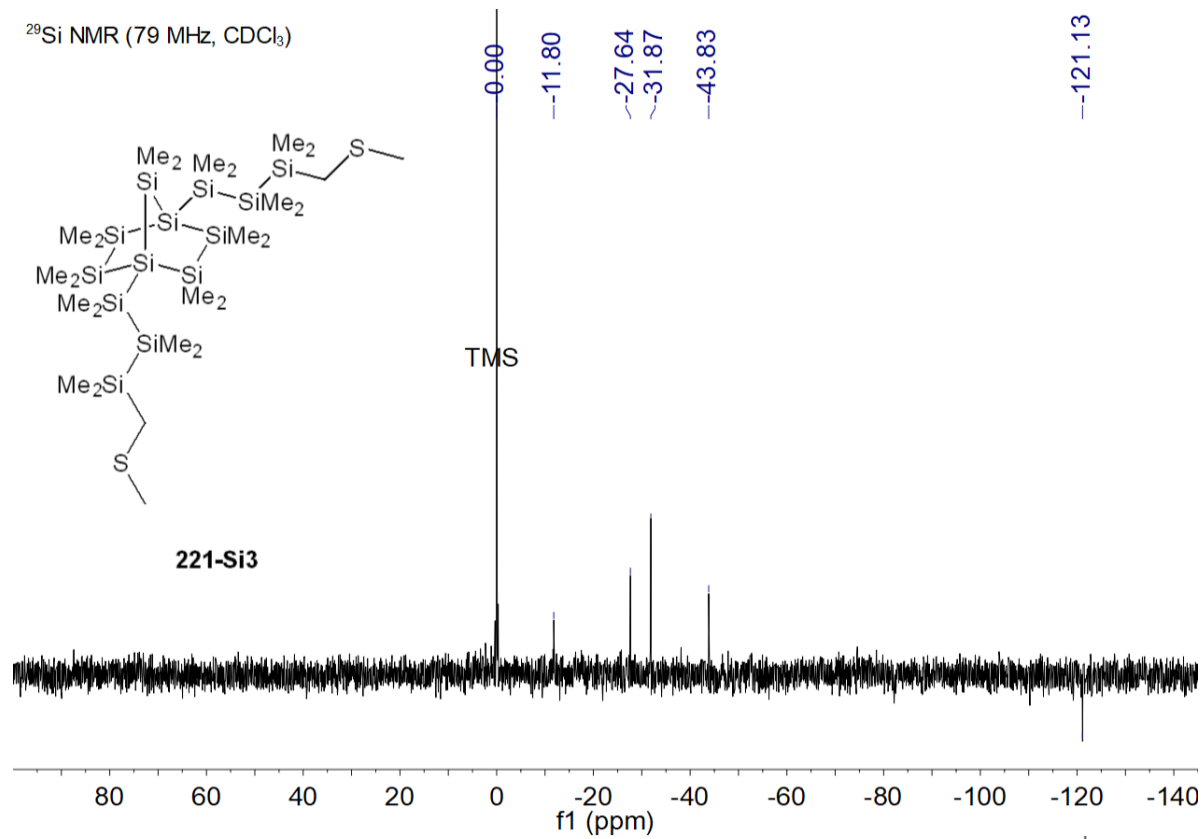


¹H NMR (400 MHz, CDCl₃)

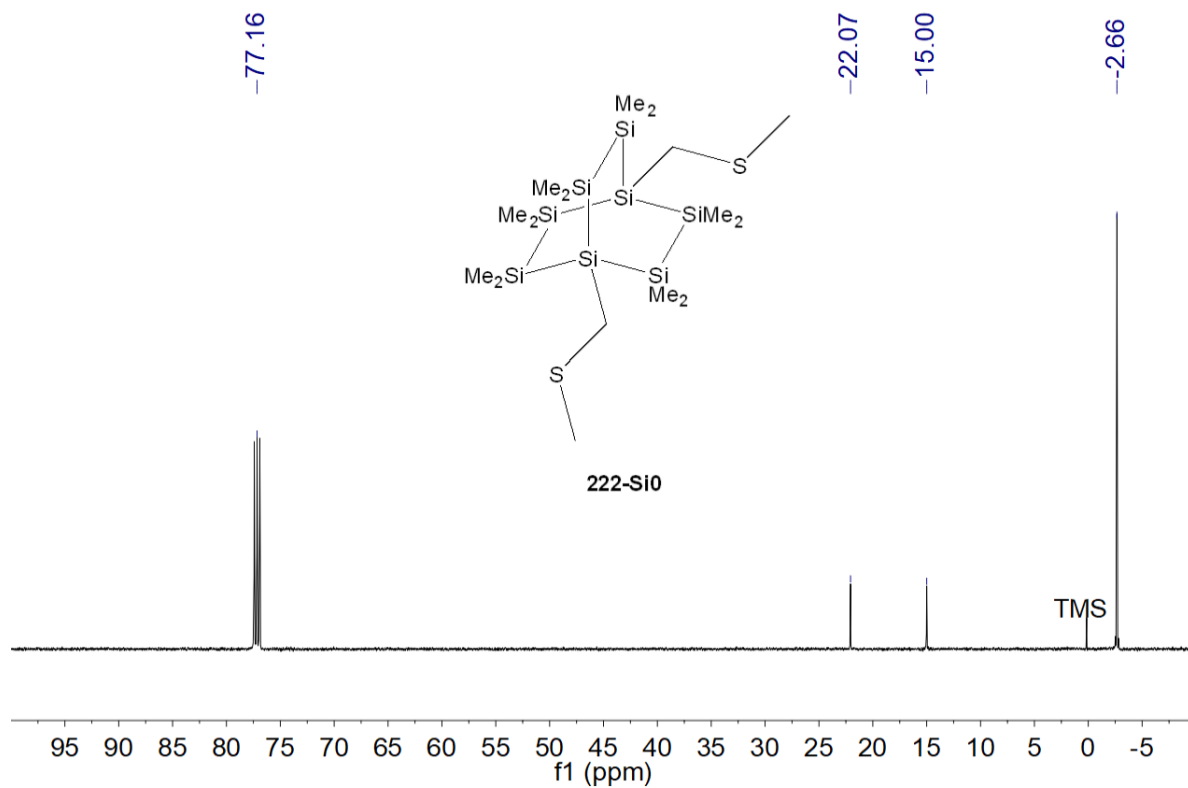


¹³C NMR (101 MHz, CDCl₃)

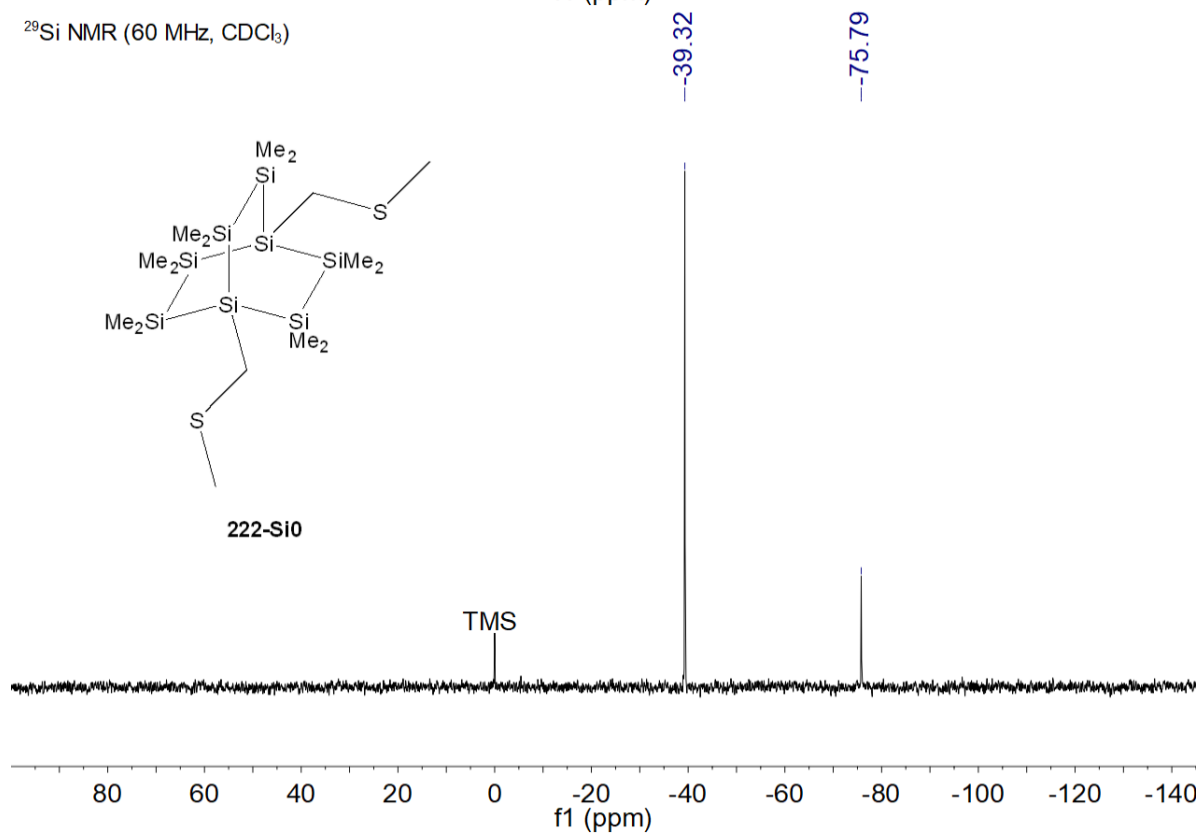


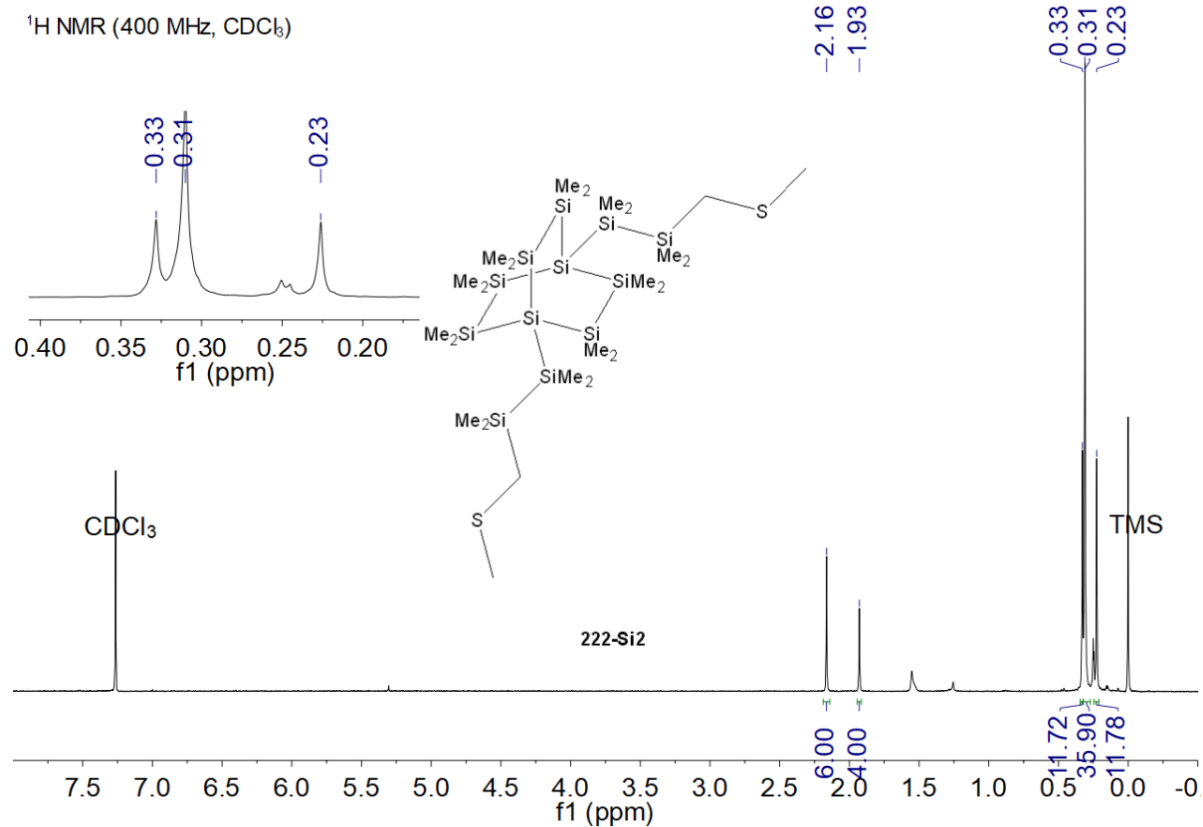
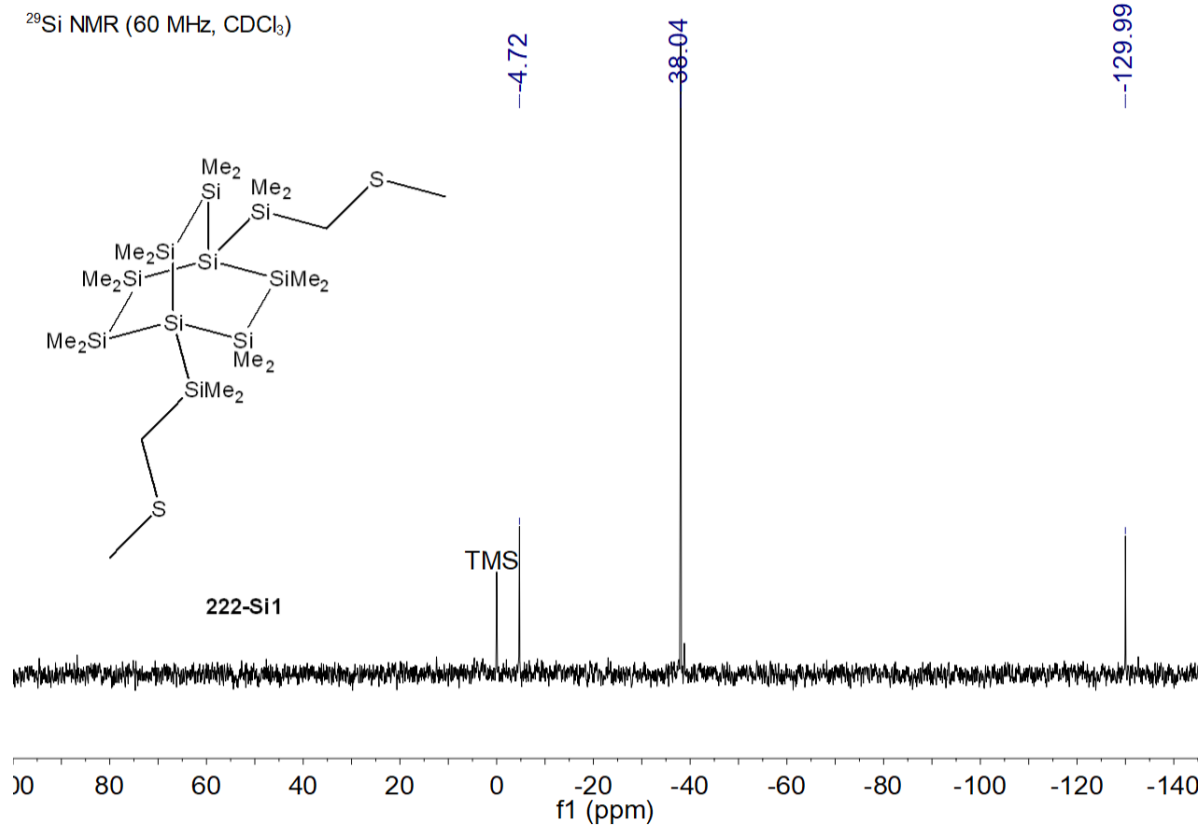


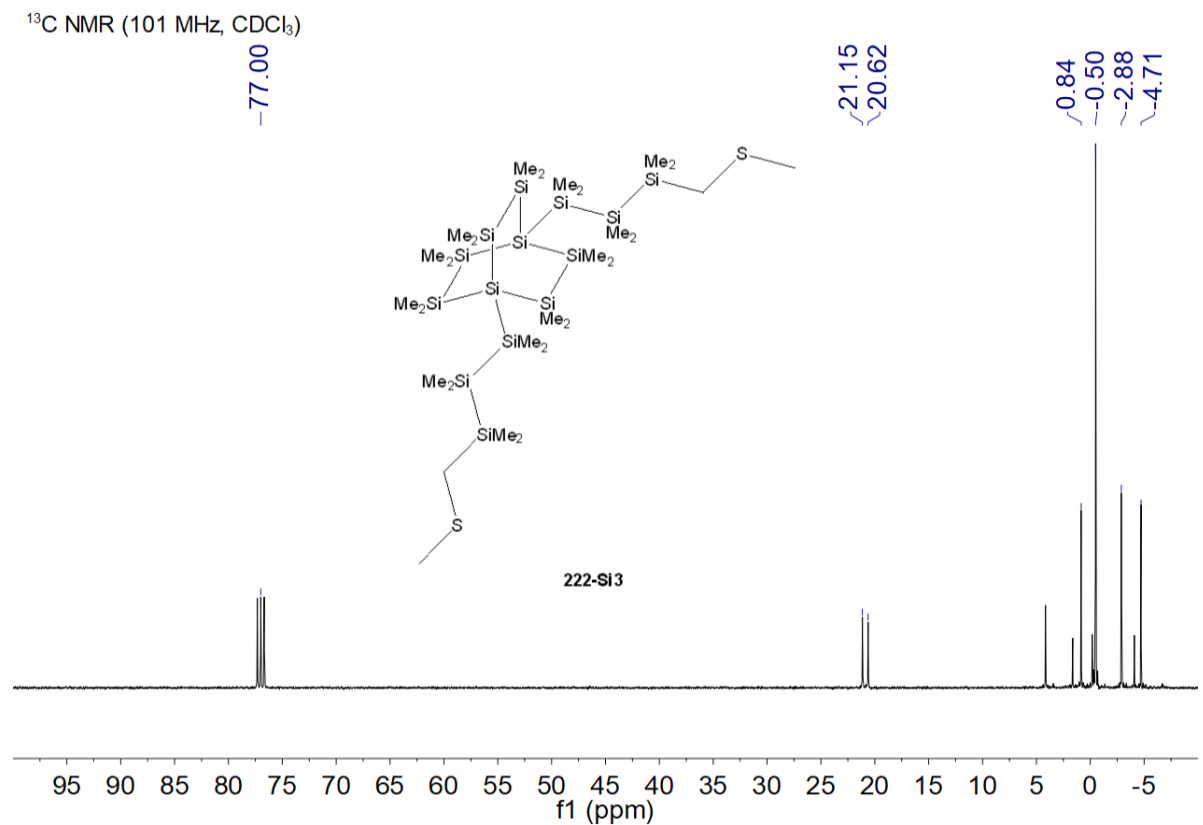
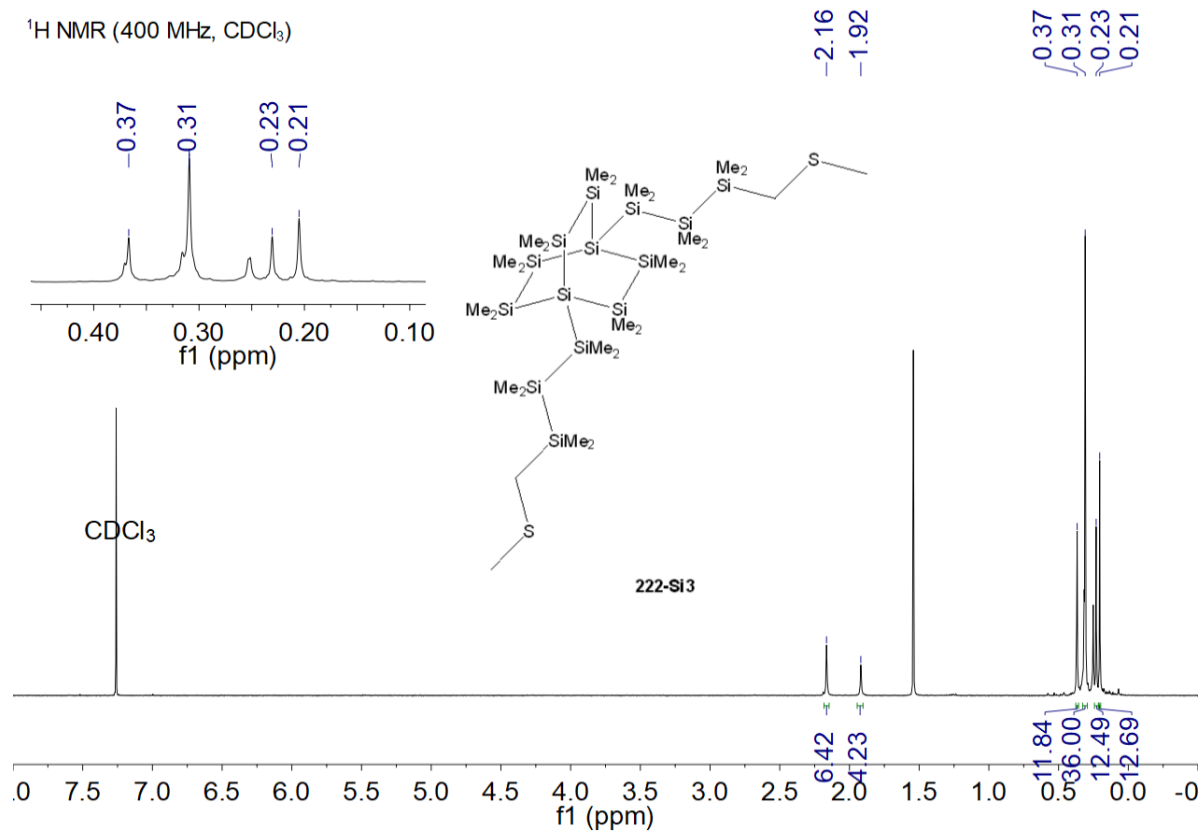
¹³C NMR (126 MHz, CDCl₃)

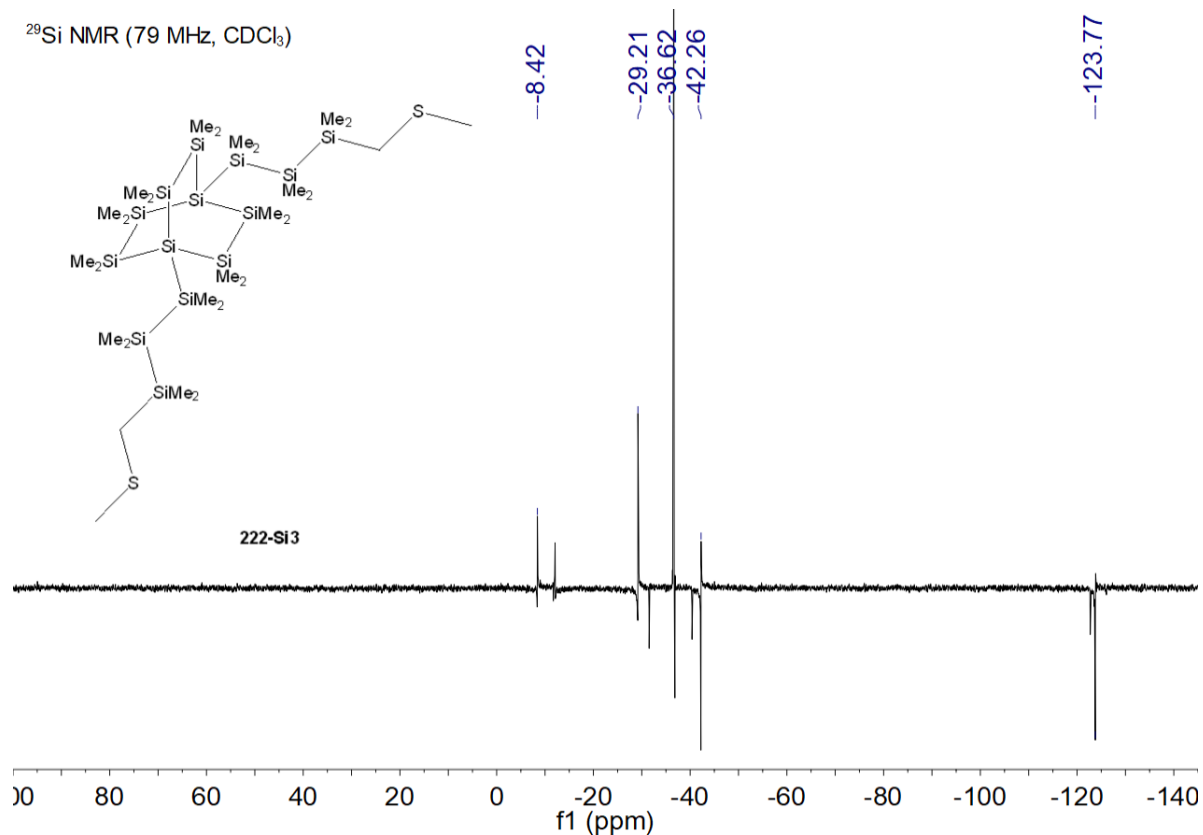


²⁹Si NMR (60 MHz, CDCl₃)









VI. References

1. Brandbyge, M.; Mozos, J.-L.; Ordejón, P.; Taylor, J.; Stokbro, K. *Phys. Rev. B* **2002**, 65, 165401.
2. Atomistix ToolKit version2016.3 (QuantumWiseA/S,2016); quantumwise.com.
3. Virtual NanoLab version2016.3 (QuantumWiseA/S,2016); quantumwise.com.
4. Solomon, G. C.; Herrmann, C.; Hansen, T.; Mujica, V.; Ratner, M. A. *Nat. Chem.* **2010**, 2, 223-228.
5. Su, T. A.; Li, H.; Steigerwald, M. L.; Venkataraman, L.; Nuckolls, C. *Nat. Chem.* **2015**, 7, 215-220.
6. Tkatchenko, A.; Scheffler, M. *Phys. Rev. Lett.* **2009**, 102, 073005.
7. Li, H.; Garner, M. H.; Shanguan, Z.; Zheng, Q.; Su, T. A.; Neupane, M.; Li, P.; Velian, A.; Steigerwald, M. L.; Xiao, S.; Nuckolls, C.; Solomon, G. C.; Venkataraman, L. *Chem. Sci.* **2016**, 7, 5657-5662.
8. Ogura, K.; Fujita, M.; Takahashi, K.; iida, H. *Chemischer Informationsdienst* **1983**, 14.
9. Klausen, R. S.; Widawsky, J. R.; Steigerwald, M. L.; Venkataraman, L.; Nuckolls, C. *J Am Chem Soc* **2012**, 134, 4541-4.
10. Fischer, R.; Baumgartner, J.; Kickelbick, G.; Marschner, C. *J Am Chem Soc* **2003**, 125, 3414-5.
11. Fischer, R.; Konopa, T.; Baumgartner, J.; Marschner, C. *Organometallics* **2004**, 23, 1899-1907.
12. Marschner, C. *Organometallics* **2006**, 25, 2110-2125.